

**ENGINEERING MAGNETIC TRANSITIONS AND MAGNETOCALORIC
EFFECT IN RARE-EARTH TRANSITION METAL ICOSAGENIDES**

by
George Agbaworvi

A Dissertation

*Submitted to the Faculty of Purdue University
In Partial Fulfillment of the Requirements for the degree of*

Doctor of Philosophy



Department of Chemistry
West Lafayette, Indiana
May 2020

THE PURDUE UNIVERSITY GRADUATE SCHOOL
STATEMENT OF COMMITTEE APPROVAL

Dr. Corey M. Thompson, Chair

Department of Chemistry

Dr. Christina Li

Department of Chemistry

Dr. Jonathan Wilker

Department of Chemistry

Dr. Xianfan Xu

School of Mechanical Engineering

Approved by:

Dr. Christine Hrycyna

ACKNOWLEDGMENTS

I am indeed grateful to the highest God for his kind blessings, goodness, guidance, and protection throughout my five years at Purdue University. My profound gratitude goes to my advisor Dr. Corey Thompson for allowing me to work in his lab. I appreciate his guidance, tolerance, constructive criticisms, support, and patience in ensuring that I carry my research work to its logical conclusion over the years of my study at Purdue University. I would also like to thank my supervisory committee members, Dr. Christina Li, Dr. Jonathan Wilker, and Dr. Xianfan Xu for their suggestions regarding my research, especially, their feedback on my end of the year research report. In addition, I would like to thank Dr. Fang Yuan for her contribution towards my research. I wish her great success at Princeton University. To Dr. Matthew Zeller and Dr. Neil Dilley, I thank you for helping me with crystallography and magnetism respectively.

A special appreciation goes to the current and past graduate students of the Thompson's lab who have been there to keep me on track from the beginning to the end. Thank you, Robert Compton, Sebastian Calderon Cazorla, Benjamin Daum, and Andrew Bowser. To the numerous committed undergrads who worked with me, I'm indeed grateful for your support over the years. Thank you, Justin Wong, Brittany Linn, Patrick Curley, and Samuel Hostettler. I wish all of you the best in your future endeavors.

Finally, to my family, I give my unending thanks for the love, support, and encouragement you have shown me through this experience. To Dave and Betsy Ayers, special thanks to you and your family for your love and care here in West Lafayette. If I had to come back to West Lafayette, It's because of you. To my mum, my brother, Norbert Agbeworvi, niece, Dominion Enalasie Agbeworvi, and brother, Emmanuel Quarshie Avisseh, thank you all for your prayers and support.

Last but not least, I would like to thank all the graduate students in the Chemistry department and all the friends I have met over the years here at Purdue University.

TABLE OF CONTENTS

LIST OF TABLES	7
LIST OF FIGURES	8
LIST OF ABBREVIATIONS	12
ABSTRACT.....	13
CHAPTER 1. INTRODUCTION	14
1.1 Magnetism in Intermetallic Compounds.....	14
1.2 Magnetocaloric Effect (MCE)	18
1.2.1 Discovery of Magnetocaloric Effect.....	18
1.2.2 Magnetic Refrigeration.....	20
1.2.3 Design of magnetic refrigeration materials for practical applications.....	21
1.3 Magnetocaloric Materials	22
1.3.1 Gd ₅ T ₄ -based Phases (T = main group elements)	22
1.3.2 Ni ₂ MnGa-based Heusler Alloys	23
1.3.3 As containing materials	24
1.3.4 Laves phases	24
1.4 Materials in focus.....	25
1.5 References.....	25
CHAPTER 2. SIGNIFICANTLY ENHANCED CURIE TEMPERATURE OF TERNARY LAVES PHASES RCr _{0.4} Al _{1.6} and RZnAl (R = Tb, Dy, Ho).....	29
2.1 Introduction.....	29
2.2 Experimental details.....	31
2.2.1 Synthesis	31
2.2.2 Physical property Measurements	31
2.2.3 Structure Determination.....	32
2.3 Results and Discussion	32
2.3.1 Crystal Structure	32
2.3.2 Structural Characterization	33
2.3.3 Magnetic Properties	34
2.3.3.1 RCr _{0.4} Al _{1.6} (R = Tb, Dy, Ho) phase	34

2.3.3.2	RZnAl (R = Tb, Dy, Ho) phase.....	37
2.3.4	Magnetocaloric Effect	39
2.3.5	Magnetoresistance (MR) Effect.....	42
2.4	Conclusion	43
2.5	References.....	44
CHAPTER 3. ENGINEERING MAGNETIC TRANSITIONS IN TERNARY LAVES TYPE PHASES, GdCr _x Al _{2-x} AND GdZnAl.		
3.1	Introduction.....	47
3.2	Experimental details.....	49
3.2.1	Synthesis.....	49
3.2.2	Physical property Measurements	49
3.2.3	Structure Determination.....	49
3.2.4	Computational details	50
3.3	Results and Discussion	51
3.3.1	Structural Characterization	51
3.3.2	Magnetic Properties	52
3.3.2.1	GdCr _{0.2} Al _{1.8} , GdCr _{0.3} Al _{1.7} , GdCr _{0.4} Al _{1.6} and GdCr _{0.45} Al _{1.55}	52
3.3.2.2	GdZnAl	55
3.3.3	Magnetocaloric effect of GdCr _x Al _{2-x}	56
3.3.4	Magnetocaloric effect of GdZnAl	59
3.3.5	Magnetoresistance effect of Gd-Cr-Al and GdZnAl	60
3.4	Conclusion	63
3.5	References.....	64
CHAPTER 4. MANIPULATION OF THE STRUCTURAL, MAGNETIC, AND MAGNETOCALORIC PROPERTIES IN GdNi _{3-x-y} Co _x Al _y VIA VALENCE ELECTRON PERTURBATION.		
4.1	Introduction.....	67
4.2	Experimental details.....	68
4.2.1	Synthesis.....	68
4.2.2	Physical property Measurements	69
4.2.3	Structure Determination.....	69

4.3	Results and Discussion	69
4.3.1	Structural Characterization	69
4.3.2	Crystal Chemistry	71
4.3.3	Magnetic Properties of $\text{GdNi}_{3-x-y}\text{Co}_x\text{Al}_y$ phases	72
4.3.4	Magnetocaloric effect of $\text{GdNi}_{3-x-y}\text{Co}_x\text{Al}_y$ phases	76
4.3.5	Magnetoresistance of GdCo_2Al	81
4.4	Conclusion	81
4.5	References.....	82
CHAPTER 5. MAGNETOCALORIC EFFECT (MCE) AND MAGNETIC PROPERTIES OF GdNiGa_2 AND THE CO-DOPED GADOLINIUM NICKEL GALLIDES ($\text{GdNi}_{3-x-y}\text{Co}_x\text{Ga}_y$) ..		84
5.1	Introduction.....	84
5.2	Experimental details.....	86
5.2.1	Synthesis	86
5.2.2	Physical property Measurements	86
5.2.3	Structure Determination.....	86
5.2.4	Energy dispersive X-ray Fluorescence (EDXRF) Data.....	87
5.3	Results and Discussion	87
5.3.1	Structural Characterization	87
5.3.2	Magnetic Properties of $\text{GdNi}_{3-x-y}\text{Co}_x\text{Ga}_y$ phases	89
5.3.3	Magnetocaloric effect of $\text{GdNi}_{3-x-y}\text{Co}_x\text{Al}_y$ phases	93
5.4	Conclusion	97
5.5	References.....	98
CHAPTER 6. CONCLUSIONS AND FUTURE WORK		104
APPENDIX A. FIGURES FROM CHAPTER 2.....		107
APPENDIX B. FIGURES FROM CHAPTER 3.....		108
APPENDIX C. FIGURES FROM CHAPTER 4.....		109
APPENDIX D. FIGURES FROM CHAPTER 5.....		115

LIST OF TABLES

Table 2.1. Lattice parameters of RZnAl and RCr _{0.4} Al _{1.6} .	34
Table 2.2. Magnetic properties of RCr _{0.4} Al _{1.6} and RZnAl(R = Tb, Dy, Ho) compounds: Curie temperature (T_C), saturation magnetization per formula unit M_{sat}/fu at 2K and effective magnetic moment per formula unit (M_{eff}/fu) and per transition metals (M_{eff}/T).	37
Table 2.3. The T_C , $-\Delta S_M^{max}$, and RCP for $\Delta H = 0-5$ T for RZnAl and HoCr _{0.4} Al _{1.6} as well as some selected low-temperature magnetocaloric materials.	41
Table 3.4. Lattice parameters from Rietveld refinements of the Powder X-ray diffraction data of GdCr _{0.2} Al _{1.8} , GdCr _{0.3} Al _{1.7} , GdCr _{0.4} Al _{1.6} , GdCr _{0.45} Al _{1.55} , and GdZnAl.	52
Table 3.5. The Curie temperature (T_C), and structure for GdZnAl and GdCr _{0.45} Al _{1.5} compared with other GdAl systems.	57
Table 3.6. The T_C , $-\Delta S_M^{max}$, and RCP for $\Delta H = 0-5$ T for GdZnAl and GdCr _{0.45} Al _{1.55} as well as other GdAl (Mn, Fe, Co, Ni, Cu) variants.	60
Table 4.1. Lattice parameters from Rietveld refinements of the powder X-ray diffraction data of GdNi _{3-x-y} Co _x Al _y .	71
Table 4.2. Magnetic properties GdCo _x Ni _{3-x-y} Al _y compounds: effective magnetic moment per formula unit (M_{eff}/fu) and per transition metals (M_{eff}/T), saturation magnetization per formula unit M_{sat}/fu at 2K and curie temperature (T_C).	74
Table 4.3a. The T_C , $-\Delta S_M^{max}$, and RCP for $\Delta H = 0-5$ T for GdNi _{3-x-y} Co _x Al _y and some recently reported magnetocaloric materials.	80
Table 4.4b. The T_C , $-\Delta S_M^{max}$, and RCP for $\Delta H = 0-5$ T for GdNi _{3-x-y} Co _x Al _y and some recently reported magnetocaloric materials.	80
Table 5.1. Lattice parameters from Rietveld refinements of the powder X-ray diffraction data of GdNiGa ₂ GdNi _{3-x-y} Co _x Ga _y .	88
Table 5.2. Elemental composition of GdNiGa ₂ and GdNi _{3-x-y} Co _x Ga _y series from Energy Dispersive X-ray Fluorescence analysis (EDXRF).	89
Table 5.3. Magnetic Properties of GdNiGa ₂ and GdNi _{3-x-y} Co _x Ga _y Compounds: T_C , Curie Temperature; θ , Paramagnetic Weiss Temperature.	91
Table 5.4. Magnetic Properties of Compounds of GdNi _{3-x-y} Co _x Ga _y : μ_{eff} , Effective Magnetic Moment; μ_{sat} , Saturation Magnetization at 2 K and 7 T; T_C , Curie Temperature.	92
Table 5.5. Maximum of the Magnetic Entropy Change at various applied magnetic fields, the RCP, Relative Cooling Powder calculated at 0-5 T.	96

LIST OF FIGURES

Figure 1.1. Schematic representation of the four-basic magnetism.....	16
Figure 1.2. The (a) magnetic susceptibility and (b) inverse magnetic susceptibility	17
Figure 1.3. The diagram of the magnetocaloric effect (MCE).	19
Figure 1.4. Schematic representation of a magnetic refrigeration cycle.....	20
Figure 1.5. Crystal structures of orthorhombic Gd_5Si_4 - (left), monoclinic $Gd_5Si_2Ge_2$ - (middle), orthorhombic Sm_5Ge_4 - (right) type structure. (Si, Ge) atoms between the slabs are in red; Gd atoms are in blue; (Si, Ge) atoms inside the slabs are in green; ²⁰	22
Figure 1.6. Crystal structure of $MgCu_2$ (left) and $MgZn_2$ (right) type structure	33
Figure 1.7. Rietveld refinement of the powder X-ray diffraction patterns of (a) $RZnAl$, and (b) $RCr_{0.4}Al_{1.6}$	34
Figure 1.8. Magnetization vs temperature of (a) $TbCr_{0.4}Al_{1.6}$, (b) $DyCr_{0.4}Al_{1.6}$ and (c) $HoCr_{0.4}Al_{1.6}$ compounds in applied field of 0.1 T.	35
Figure 1.9. Magnetization vs. magnetic field data of (a) $TbCr_{0.4}Al_{1.6}$ at 2 K, 10 K, 50 K, 75 K, 150 K, 300 K (b) $DyCr_{0.4}Al_{1.6}$ at 2 K, 10 K, 50 K, 75 K, 150 K, 300 K and (c) $HoCr_{0.4}Al_{1.6}$ at 2 K, 10 K and 300 K.	36
Figure 1.10. Magnetization vs temperature of (a) $TbZnAl$, (b) $DyZnAl$, and (c) $HoZnAl$ compounds in an applied field of 0.1 T.	38
Figure 1.11. Magnetization vs. magnetic field data of (a) $TbZnAl$ at 2 K, 10 K, 75 K, 100 K, 125 K (b) $DyZnAl$ at 2 K, 25 K, 60 K, 90 K, and (c) $HoZnAl$ at 2 K, 10 K and 300 K.	39
Figure 1.12. Isothermal magnetic entropy changes for (a) $TbZnAl$, (b) $DyZnAl$, (c) $HoZnAl$, for magnetic changes of $\mu_0\Delta H = 2$ T and 5 T. (d) $TbCr_{0.4}Al_{1.6}$, (e) $DyCr_{0.4}Al_{1.6}$ and (f) $HoCr_{0.4}Al_{1.6}$ for magnetic changes of $\mu_0\Delta H = 5$ T	40
Figure 1.13. Resistivity as a function of temperature at zero magnetic field of (a) $DyCr_{0.4}Al_{1.6}$ and (b) $DyZnAl$	42
Figure 1.14. Magnetoresistance as a function of the applied magnetic field of (a) $DyCr_{0.4}Al_{1.6}$ and (b) $DyZnAl$ at 2 K.	43
Figure 3.1. Rietveld refinement of the powder X-ray diffraction patterns of (a) $GdCr_xAl_{2-x}$, and (b) $GdZnAl$	51
Figure 3.2. Magnetization vs temperature of (a) $GdCr_{0.2}Al_{1.8}$, (b) $GdCr_{0.3}Al_{1.7}$ and (c) $GdCr_{0.4}Al_{1.6}$ and (d) $GdCr_{0.45}Al_{1.5}$ compounds in applied field of 0.1 T.....	53
Figure 3.3. Magnetization as a function of the external magnetic field of (a) $GdCr_{0.2}Al_{1.8}$, (b) $GdCr_{0.3}Al_{1.7}$ and (c) $GdCr_{0.4}Al_{1.6}$ and (d) $GdCr_{0.45}Al_{1.55}$ compounds at 2 K in fields up to 7 T...	54

Figure 3.4. Magnetic properties of GdZnAl: (a) magnetic susceptibility at 0.01 T; (b) isothermal	56
Figure 3.5. Variation of Curie temperature as a function of valence electron concentration of T on selected GdTAl (T = Zn, Cu, Ni, Co, Fe, Mn, Cr).....	57
Figure 3.6 Temperature dependence of the isothermal magnetic entropy changes for (a) GdCr _{0.2} Al _{1.8} , (b) GdCr _{0.3} Al _{1.7} , (c) GdCr _{0.4} Al _{1.6} and (d) GdCr _{0.45} Al _{1.55} in the field change of 0-5 T.	58
Figure 3.7. (a) Magnetization isotherms of GdZnAl at various temperatures (118 – 157 K); (b) Temperature dependence of the isothermal magnetic entropy changes for GdZnAl in the field change of 0-2 and 0-5 T.	59
Figure 3.8. Unit cell volume dependence of the magnetic entropy change for the GdCr _{0.45} Al _{1.55} , GdZnAl, and other GdTAl (T = Mn, Fe, Co, Ni, Cu) compounds.	60
Figure 3.9. Resistivity as a function of temperature at various applied magnetic fields for (a) GdCr _{0.2} Al _{1.8} , (b) GdCr _{0.4} Al _{1.6} , (c) GdCr _{0.45} Al _{1.55} and (d) GdZnAl.	61
Figure 3.10. Magnetoresistance as a function of applied magnetic field at various temperatures for (a) GdCr _{0.2} Al, (b) GdCr _{0.4} Al _{1.5} and (c) GdCr _{0.45} Al _{1.5} and (d) GdZnAl.....	62
Figure 3.11. (a) The electronic band structure of GdCr _{0.5} Al _{1.5} indicates metallic behavior. (b) The (b) total and (c) partial DOS is split into their spins.	63
Figure 4.1. Rietveld refinement of the powder X-ray diffraction patterns of (a) GdCo _x Ni _{1-x} Al ₂ , (b) GdCo _x Ni _{3-x-y} Al _y , (c) GdCoAl ₂	70
Figure 4.2. Crystal structure of GdNiAl ₂ (left) and GdNi _{3-x-y} Co _x Al _y (right).....	72
Figure 4.3. Magnetization vs temperature of (a) GdCo _x Ni _{1-x} Al ₂ , (b) GdCo _x Ni _{3-x} Al _y compounds in applied field of 0.01 T.....	73
Figure 4.4. Magnetization vs magnetic field of (a) GdCo _x Ni _{1-x} Al ₂ , (b) GdCo _x Ni _{3-x} Al _y compounds at 2 K and (c) GdCo ₂ Ni _{0.5} Al _{0.5} at 2, 280, 320 K in fields up to 7 T.....	75
Figure 4.5. Saturation magnetic moments M_{sat} obtained from magnetization isotherms $M(H)$ measured at 2 K for the GdNi _{3-x-y} Co _x Al _y compounds.	76
Figure 4.6 Isothermal magnetic entropy changes for (a) GdNiAl ₂ (b) GdCo _{0.5} Ni _{0.5} Al ₂ , (c) GdCo _{0.75} Ni _{0.25} Al ₂ , (d) GdCoAl ₂ for magnetic changes of $\mu_0\Delta H = 2$ T and 5 T.	77
Figure 4.7. Isothermal magnetic entropy changes for (e) GdCo _{0.25} Ni _{2.5} Al _{0.25} , (f) GdCo _{0.5} Ni ₂ Al _{0.5} , (g) GdCoNiAl, (h) GdCo _{1.5} Ni _{0.5} Al, for magnetic changes of $\mu_0\Delta H = 2$ T and 5 T.	78
Figure 4.8. Isothermal magnetic entropy changes for (i) GdCoNi _{1.5} Al _{0.5} , (j) GdCo ₂ Al, (k) GdCo _{1.5} NiAl _{0.5} and (l) GdCo ₂ Ni _{0.5} Al _{0.5} for magnetic changes of $\mu_0\Delta H = 2$ T and 5 T.....	79
Figure 4.9. (a) Change of magnetic entropy and saturated magnetization versus the Co-concentration, (b) change of magnetic entropy versus the unit cell volume for the GdCo _x Ni _{3-x} Al _y compounds.	79

Figure 4.10. Resistivity as a function of temperature at 0 and 7T applied magnetic fields for GdCo ₂ Al. Inset magnetoresistance as a function of applied field at 2K.....	81
Figure 5.1. Rietveld refinement of the powder X-ray diffraction patterns of (a) GdNiGa ₂ , (b) GdNi _{3-x-y} Co _x Ga _y	88
Figure 5.2. Variation of unit cell volume of the GdCo _{0.25} Ni _{2.5} Ga _{0.25} , GdCo _{0.5} Ni ₂ Ga _{0.5} , GdCoNi _{1.5} Ga _{0.5} , GdCo _{1.5} NiGa _{0.5} and GdCo ₂ Ni _{0.5} Ga _{0.5} as a function of the Co concentration.....	90
Figure 5.3. Magnetic susceptibility of (a) GdNiGa ₂ , (b) GdNi _{3-x-y} Co _x Ga _y series, measured under the field of 0.01 T.....	90
Figure 5.4. Field dependence of magnetization for (a) GdNiGa ₂ and (b) GdNi _{3-x-y} Co _x Ga _y at 2 K.	92
Figure 5.5. Saturation magnetic moments M_{sat} measured at 2 K for the GdNi _{3-x-y} Co _x Ga _y compounds as a function of the Co concentration.	93
Figure 5.6. (a) Selected magnetization isotherms for GdNiGa ₂ , measured between 11 and 47 K. (b) Magnetic entropy change of GdNiGa ₂ for a $\Delta H = 0-2$ T.....	93
Figure 5.7. Temperature dependence of the magnetic entropy change ΔS_M of (a) GdCo _{0.25} Ni _{2.5} Ga _{0.25} , (b) GdCo _{0.5} Ni ₂ Ga _{0.5} , (c) GdCoNiGa (d) GdCo _{1.5} Ni _{0.5} Ga compounds.	94
Figure 5.8. Temperature dependence of the magnetic entropy change ΔS_M of (a) GdCoNi _{1.5} Ga _{0.5} , (b) GdCo ₂ Ga, (c) GdCo _{1.5} NiGa _{0.5} (d) GdCo ₂ Ni _{0.5} Ga _{0.5} compounds.....	95
Figure 5.9. The change of magnetocaloric effect at 0-5 T versus (a) saturation magnetization at 2 K and (b) the volume of the unit cell, for some selected phases.	97
Figure A.1. Rietveld refinement of the powder X-ray diffraction patterns of (a) TbZnAl, (b) DyZnAl, (c) HoZnAl (d) TbCr _{0.4} Al _{1.6} , (e) DyCr _{0.4} Al _{1.6} and (f) HoCr _{0.4} Al _{1.6}	107
Figure B.1. Rietveld refinement of the powder X-ray diffraction patterns of (a) GdCr _{0.2} Al _{1.8} , (b) GdCr _{0.3} Al _{1.7} and (c) GdCr _{0.4} Al _{1.6} and (d) GdCr _{0.45} Al _{1.55} compounds	108
Figure C.1. Rietveld refinement of the powder X-ray diffraction patterns of (a) GdNiAl ₂ , (b) GdCo _{0.5} Ni _{0.5} Al ₂ , (c) GdCo _{0.75} Ni _{0.25} Al ₂ , (d) GdCoAl ₂ , (e) GdCo _{0.25} Ni _{2.5} Al _{0.25} , (f) GdCo _{0.5} Ni ₂ Al _{0.5}	109
Figure C.2. Rietveld refinement of the powder X-ray diffraction patterns of (g) GdCoNiAl, (h) GdCo _{1.5} Ni _{0.5} Al, (i) GdCoNi _{1.5} Al _{0.5} , (j) GdCo ₂ Al, (k) GdCo _{1.5} NiAl _{0.5} and (l) GdCo ₂ Ni _{0.5} Al _{0.5} . .	110
Figure C.3. Temperature dependence of zero-field cooled (ZFC) and field cooled (FC) magnetic	111
Figure C.4. Temperature dependence of zero-field cooled (ZFC) and field cooled (FC) magnetic	112
Figure C.5. Field dependence of magnetization for (a) GdNiAl ₂ , (b) GdCo _{0.5} Ni _{0.5} Al ₂ (c) GdCo _{0.75} Ni _{0.25} Al ₂ (d) GdCoAl ₂ , (e) GdCo _{0.25} Ni _{2.5} Al _{0.25} and (f) GdCo _{0.5} Ni ₂ Al _{0.5} compounds at 2 K in fields up to 7 T.....	113

Figure C.6. Field dependence of magnetization for (g) GdCoNiAl , (h) $\text{GdCo}_{1.5}\text{Ni}_{0.5}\text{Al}_{0.5}$, (i) $\text{GdCoNi}_{1.5}\text{Al}_{0.5}$, (j) GdCo_2Al , (k) $\text{GdCo}_{1.5}\text{NiAl}_{0.5}$ compounds at 2 K and (l) $\text{GdCo}_2\text{Ni}_{0.5}\text{Al}_{0.5}$ at 2, 280, 320 K in fields up to 7 T.	114
Figure D.1. Rietveld refinement of the powder X-ray diffraction patterns of (a) GdNiGa_2 , (b) $\text{GdCo}_{0.25}\text{Ni}_{2.5}\text{Ga}_{0.25}$, (c) $\text{GdCo}_{0.5}\text{Ni}_2\text{Ga}_{0.5}$, (e) $\text{GdCo}_{1.5}\text{Ni}_{0.5}\text{Ga}$, (f) $\text{GdCoNi}_{1.5}\text{Ga}_{0.5}$ and (g) GdCo_2Ga	115
Figure D.2. Rietveld refinement of the powder X-ray diffraction patterns of (h) $\text{GdCo}_{1.5}\text{NiGa}$, (i) $\text{GdCo}_2\text{Ni}_{0.5}\text{Ga}_{0.5}$	116
Figure D.3. Temperature dependence of magnetic susceptibility for (g) GdCo_2Ga , (h) $\text{GdCo}_{1.5}\text{NiGa}_{0.5}$, and (i) $\text{GdCo}_2\text{Ni}_{0.5}\text{Ga}_{0.5}$ compounds in applied field of 0.01 T.	116
Figure D.4. Temperature dependence of magnetic susceptibility for (a) GdNiGa_2 , (b) $\text{GdCo}_{0.25}\text{Ni}_{2.5}\text{Ga}_{0.25}$, (c) $\text{GdCo}_{0.5}\text{Ni}_2\text{Ga}_{0.5}$, (d) GdCoNiGa , (e) $\text{GdCo}_{1.5}\text{Ni}_{0.5}\text{Ga}$ and (f) $\text{GdCoNi}_{1.5}\text{Ga}_{0.5}$ compounds in applied field of 0.01 T.	117
Figure D.5. Linear fit of the inverse susceptibility to the Curie-Weiss law for (a) GdNiGa_2 , (b) $\text{GdCo}_{0.25}\text{Ni}_{2.5}\text{Ga}_{0.25}$, (c) $\text{GdCo}_{0.5}\text{Ni}_2\text{Ga}_{0.5}$, (d) GdCoNiGa , (e) $\text{GdCo}_{1.5}\text{Ni}_{0.5}\text{Ga}$ and (f) $\text{GdCoNi}_{1.5}\text{Ga}_{0.5}$ compounds.	118
Figure D.6. Linear fit of the inverse susceptibility to the Curie-Weiss law for (g) GdCo_2Ga , (h) $\text{GdCo}_{1.5}\text{NiGa}_{0.5}$, and (i) $\text{GdCo}_2\text{Ni}_{0.5}\text{Ga}_{0.5}$ compounds.	119
Figure D.7. Field-dependent magnetization of (b) $\text{GdCo}_{0.25}\text{Ni}_{2.5}\text{Ga}_{0.25}$, (c) $\text{GdCo}_{0.5}\text{Ni}_2\text{Ga}_{0.5}$ at 2 K.	119
Figure D.8. Field-dependent magnetization of (d) GdCoNiGa , (e) $\text{GdCo}_{1.5}\text{Ni}_{0.5}\text{Ga}$ (f) $\text{GdCoNi}_{1.5}\text{Ga}_{0.5}$, (g) GdCo_2Ga , (h) $\text{GdCo}_{1.5}\text{NiGa}_{0.5}$, and (i) $\text{GdCo}_2\text{Ni}_{0.5}\text{Ga}_{0.5}$ compounds at 2 K.	120

LIST OF ABBREVIATIONS

VEC.....	Valence Electron Concentration
T_C	Curie temperature
T_N	Néel temperature
χ	Magnetic Susceptibility
DOS.....	Density of States
MCE	Magnetocaloric effect
MR.....	Magnetoresistance
MR.....	Magnetic Refrigeration
ZFC.....	Zero Field Cooled
FC.....	Field Cooled

ABSTRACT

The global demand for energy of mankind, the ever-increasing cost of energy, and the expected depletion of fossil energy carriers within the next centuries urge the exploration of alternative and more sustainable ways to provide energy. The current quest for energy-efficient technologies for the replacement of existing cooling devices has made the magnetocaloric effect a field of current scientific interest. Cooling technologies based on magnetic refrigerants are expected to have a better environmental impact compared with those based on the gas compression-expansion cycle. This technology provides an alternative for refrigeration applications with advantages, such as high energy efficiency, environmental friendliness, and low power consumption. In search of promising magnetocaloric materials, several rare earth-depleted transition metal-based materials were designed and investigated.

In this work, $\text{RCr}_x\text{Al}_{2-x}$ and RZnAl ($\text{R} = \text{Gd, Tb, Dy, Ho}$) belonging to the ternary rare-earth transition-metal Laves phases, were chosen as the starting point to establish the effect of valence electron concentration (VEC) on the magnetic behavior and magnetocaloric effect. Our result and the results from the previously studied RTAl phases ($\text{T} = \text{Cu, Ni, Co, Fe, Mn}$) shows that the perturbation of the valence electron concentration at the Fermi level is found to be the driving force that dictates the crystal structure, magnetocaloric and magnetic properties of these systems. Most notably, the decrease in the valence electron concentration at the Fermi level leads to an increase in the curie temperature.

In addition, we have further extended this theory to GdNiAl_2 systems. GdNiAl_2 is a known magnetocaloric material which exhibits an isothermal magnetic entropy change of $\Delta S_M = 16.0 \text{ Jkg}^{-1}\text{K}^{-1}$ at $T_C = 28\text{K}$ under a magnetic field change from 0-5T. However, the low T_C limits its application as a room temperature refrigerant. We, therefore, substituted Co for (Ni/Al) in the structure of GdNiAl_2 , intending to substantially perturb the position of the Fermi level of Ni since that will lead to a decrease in the VEC and hence elevate the T_C . The study was also extended to another Icosagenides (Ga), which saw the substitution of Ga for Al in GdNiAl_2 and its Co substituted analogs. The Ga analogs exhibit complex magnetic behavior with a cascade (multiple) of magnetic transitions, as opposed to the rather simple magnetism of their Al congeners.

CHAPTER 1. INTRODUCTION

1.1 Magnetism in Intermetallic Compounds

1.1.1 Intermetallic Compounds

Intermetallic compounds are solid phases with a well-defined and fixed stoichiometry containing at least two metallic elements, with optionally one or more non-metallic elements, whose crystal structure differs markedly from those of their elemental constituents. Changing their composition alone cannot transform continuously their properties into those of their individual constituents. They form crystalline species separated by phase boundaries that are distinct from their individual elements and mixed crystals of these components. The empirical formulas for these compounds cannot be determined on the sole basis of their analytical data but in conjunction with their crystallographic information. In addition, the composition of intermetallics is affected by the normal valences, relative atomic sizes of their components, and the ratio of the total number of valence electrons to the total number of atoms. These classes of compounds have been of great interest to scientists, and engineers for many years due to their rich structural and compositional diversity. They form a complicated mixture of metallic, covalent, and ionic bonding patterns which makes them unique and the least understood among inorganic solids. Thus, there is no universal and reliable way to predict oxidation numbers of individual atoms in many of these compounds based just on its chemical composition, consequently, the discovery of new compounds with the desired properties frequently originates from exploratory synthesis.

However, some of the most important materials (silicon and aluminum-based) for commercial and technological applications have been made possible due to intermetallic compounds. Interesting magnetic and electronic properties arise when these elements (Al, Si) combine with either transition metals or lanthanides/actinides. This makes them applicable as catalysts, advanced magnet, aircraft, and automotive components, etc.¹ Intermetallics such as $\text{Nd}_2\text{Fe}_{14}\text{B}$, Alnico, and SmCo_5 have been widely explored as permanent magnets among these applications. Most household appliances, automotive parts, industrial appliances, and many other applications in our society depend on the presence of strong permanent magnetic fields for their operations.

A wide variety of properties, including Kondo effect, valence fluctuation, magnetic pole reversal, superconductivity, heavy fermion behavior, metamagnetism, spin glass, exchange-bias, magnetoresistance (MR), and magnetocaloric effect (MCE) has been displayed by some of these intermetallic compounds. Although intermetallic compounds are among the best materials that possess permanent magnet and magnetocaloric properties, it is difficult to design promising materials for such applications because the interpretation of the aforementioned properties are quite challenging to some extent.²⁻⁵

Noteworthy, most of the practicable magnetic materials contain rare-earth (R) and transition (T) metals as part of their components and thus provide strong exchange interactions between the localized $4f$ (R) and delocalized $3d$ (T) magnetic sublattices. The $4f$ electrons ensure strong magnetic anisotropy and high magnetic moment, as opposed to high transition temperatures (T_N/T_C) and strong magnetic exchange of the $3d$ moments.³ Understanding the correlation of the $3d$ - $4f$ exchange interactions with the crystal and electronic structures of these materials is very vital to develop magnetic materials with unique properties. The $3d$ itinerant electrons at the Fermi level (E_F) (highest energy of electrons in solids), drives the type and temperature of the magnetic transition in these compounds. Therefore, understanding how the magnetic behavior of these materials can be controlled, by the modifications of the density of state (DOS; describes the number of states that are to be occupied by a system at each energy level) at the Fermi level is very important.

1.1.2 Magnetism

Magnetism refers to the characteristic property of a material arising from the force caused by magnets, objects that produce fields that repel or attract other objects. It is intrinsic to all materials and exhibits itself with an applied magnetic field. This phenomenon depends on the presence or absence of unpaired magnetic spins and their response to the magnetic field applied. Depending on the orientation and quantities, the magnetization of most materials can be classified into diamagnetism, paramagnetism, ferromagnetism (FM), antiferromagnetism (AFM), and ferrimagnetism (FiM). Diamagnetic materials yield negative magnetization due to no unpaired electrons that are repelled by the applied magnetic field and are independent of temperature in general. It occurs when an induced magnetic field in the opposite direction is formed due to the application of a magnetic field thereby causing a repulsive force. It is intrinsic to all materials.

However, it is so weak that it can be easily masked by other competing magnetic behaviors in a material. On the other hand, all materials with net magnetic moment due to the unpaired electrons are attracted by the applied field and exhibit a positive magnetization. The magnetic state with weak coupling between the neighboring magnetic moment is called paramagnetism (**Fig. 1.1**). This magnetization is usually temperature-dependent. Otherwise, it could be AFM, FiM, or FM.

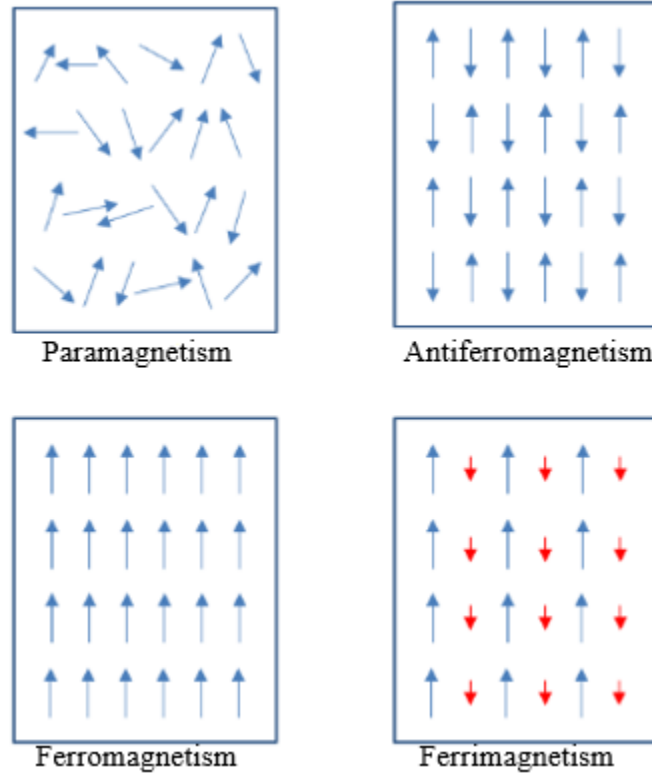


Figure 1.1. Schematic representation of the four-basic magnetism

Paramagnetism is very common and occurs in all the paramagnetic materials, above their magnetic ordering temperatures due to large thermal energy. In paramagnetic materials with localized magnetic moments, the magnetic susceptibility follows the Curie law when the magnetic interaction between spins is absent (Equation 1), or the Curie-Weiss law; where magnetic exchange coupling between spins takes place (Equation 2).

$$\chi = \frac{C}{T} \quad (1)$$

$$\chi = \frac{C}{(T-\theta)} \quad (2)$$

where C and θ are the proportionality constant and the Weiss temperature, respectively. The Weiss constant θ accounts for ferromagnetic ($\theta > 0$) or antiferromagnetic ($\theta < 0$) exchange coupling (nearest-neighbor interactions) between the spins. Therefore, θ could be used to distinguish the antiferromagnetism and ferrimagnetism from the ferromagnetism. Magnetic ordering (Fig. 1.1) arises when the exchange coupling overcomes thermal fluctuations as the temperature decreases.

Ferromagnetism arises when the magnetic spins align parallel to each other under an applied magnetic field, and the associated point of phase transition is termed Curie temperature (T_C) (Fig. 1.2). Ferromagnetism only exists with the presence of the spontaneous magnetization below Curie temperature. In the ferromagnetic state, the susceptibility is orders of magnitude higher than that of the paramagnetic state. Antiferromagnetism, on the other hand, occurs when adjacent spins align in opposite direction to each other and the corresponding temperature of this phase transition is called the Néel temperature (T_N) (Fig. 1.2). In this case, the two magnetic spins are both spontaneously magnetized but in the opposite direction, therefore, the net magnetization is nearly zero due to the equal magnitudes of the two spins.

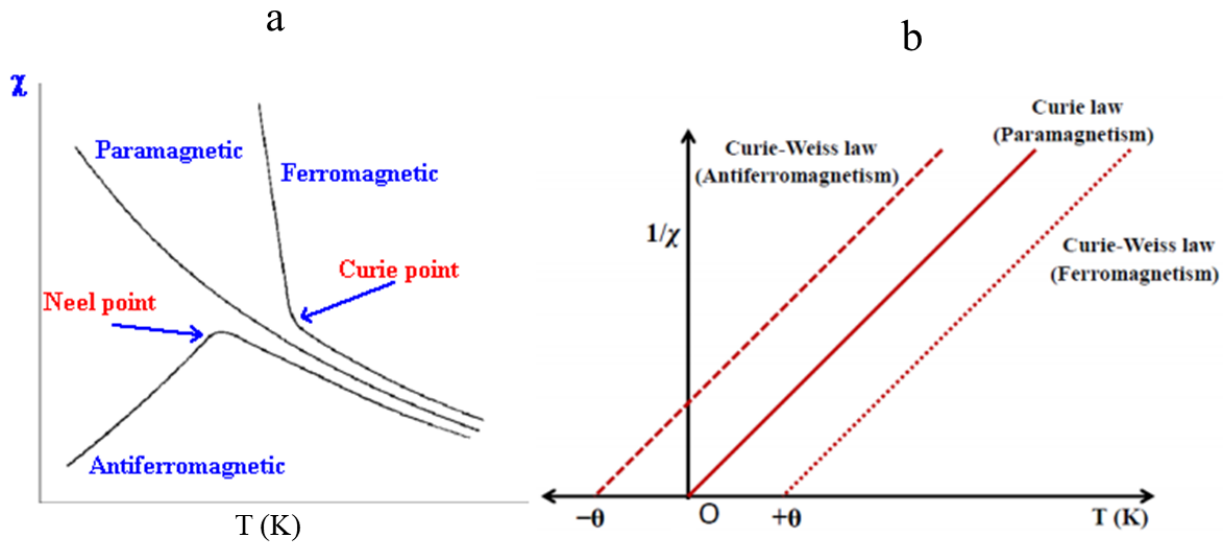


Figure 1.2. The (a) magnetic susceptibility and (b) inverse magnetic susceptibility curves for three basic magnetism.

Ferrimagnetism is closely related to both ferromagnetism and antiferromagnetism. It occurs when spins of different magnitude are aligned in opposite direction to each other (Fig. 1.1d). For one thing, ferrimagnetism has a spontaneous magnetization like that in ferromagnetism below the critical temperature, T_C . On the other hand, the adjacent magnetic moments are aligned

antiparallel like in antiferromagnetism. But the magnitude of magnetizations along the two opposite directions is not identical, therefore net magnetization is present.

Most permanent magnets and magnetocaloric materials are known to exhibit antiferro, ferro- or ferrimagnetic behaviors, and for them to be used for a practical application, they must have large magnetization values. In addition, permanent magnets required a high magnetic anisotropy for a desired property. One can differentiate one type of magnetic ordering from the other by measuring the magnetization of field and temperature dependences and obtain valuable information on magnetic spin reorientation transitions, saturation magnetic moments, charged states, critical temperatures of magnetic ordering, magnetic contribution from elements, superconducting transitions, etc.

1.2 Magnetocaloric Effect (MCE)

The rising concern on the cost of energy consumption and the depletion of the ozone layer in recent decades makes it necessary to develop new technologies to minimize the use of chemicals and techniques harmful to the environment. Magnetic refrigeration (MR) technology is one of those technologies that has gained a lot of attention in recent decades due to the discovery of giant MCE in 1997. MR technology based on MCE of materials is more energy-efficient and environmentally friendly as opposed to the MR based on the vapor-gas cycle. MR offers several advantages, i.e., high efficiency, small volume, low noise, little environmental impact, as compared with other competing technologies. As a result, several working materials with excellent MCE properties have been developed for the MR technology in the last few decades.⁶⁻⁹

1.2.1 Discovery of Magnetocaloric Effect

The magnetocaloric effect, a thermodynamic phenomenon of a magnetic material, which manifests as an adiabatic temperature change (ΔT_{ad}) or an isothermal magnetic entropy change (ΔS_M) when the magnetic material experiences the effect of varying magnetic field. It was first discovered by Warburg in 1881, when he noticed a rise in temperature when a magnetic field was applied to pure iron.¹⁰ To understand the mechanism of MCE, studies on the total entropy of a system (S) is required. The total entropy change, ΔS , equals zero. ΔS consists of magnetic (S_{mag}), lattice (S_{lat}), and electronic (S_{el}) entropies.

$$\Delta S = \Delta S_{\text{mag}} + \Delta S_{\text{lat}} + \Delta S_{\text{el}} = 0 \quad (3)$$

The magnetic entropy decreases, i.e., ΔS_{mag} has a negative value since the applied magnetic field aligns the magnetic spins. As a result, the sum of ΔS_{lat} and ΔS_{el} will be positive. The temperature of the system will go up since C_p and, ΔT_{ad} must be positive according to $(\Delta S_{\text{lat}} + \Delta S_{\text{el}})T_{\text{ad}} = C_p \Delta T_{\text{ad}}$. Otherwise, the magnetic entropy decreases with the removal of the magnetic field applied. (**Figure 1.3**).

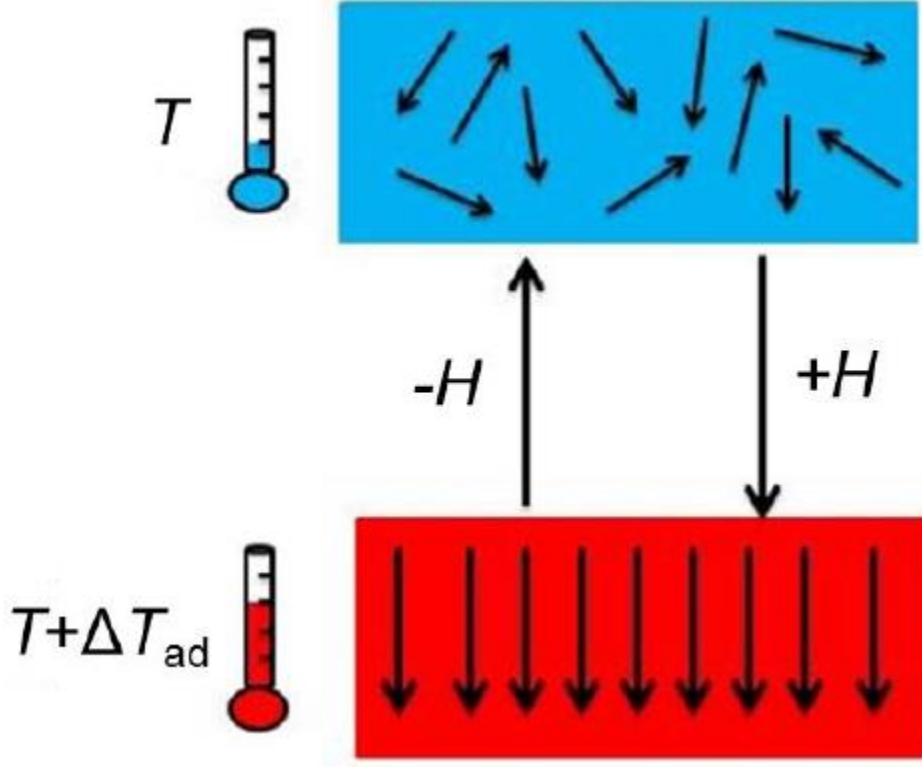


Figure 1.3. The diagram of the magnetocaloric effect (MCE).

The magnetocaloric effect of materials can be obtained using the isothermal entropy change, ΔS_{iso} , and the adiabatic temperature change, ΔT_{ad} . Under the isothermal condition, $\Delta T = 0$, the isothermal entropy change is,

$$(\Delta S_{\text{iso}})_T = \int_{H_i}^{H_f} \left(\frac{\delta M}{\delta T} \right)_{H,P} dH \quad (4)$$

Under adiabatic condition, the total entropy change is 0,

$$(\Delta T_{\text{ad}})_S = - \int_{H_i}^{H_f} \left(\frac{T}{c} \right)_{H,P} \left(\frac{\delta M}{\delta T} \right)_{H,P} dH \quad (5)$$

where C is the heat capacity under the constant pressure. ΔS_{iso} is an indirect measure of the cooling capacity of MCE materials, while ΔT_{ad} is a direct measure of the temperature change upon application of the magnetic field.

1.2.2 Magnetic Refrigeration

It is an environmentally friendly cooling technology based on the MCE. This technology can be used to attain temperature ranges used in common refrigerators as well as very extreme low temperatures. It does not use ozone-depleting chemicals, hazardous chemicals, or greenhouse gases for its operations. The magnetic refrigeration cycle (Figure 1.4) works similar to the Carnot refrigeration cycle. However, the refrigeration efficiency of the latter is only 40%, compared to 60% of the magnetic refrigeration cycle.¹¹⁻¹²

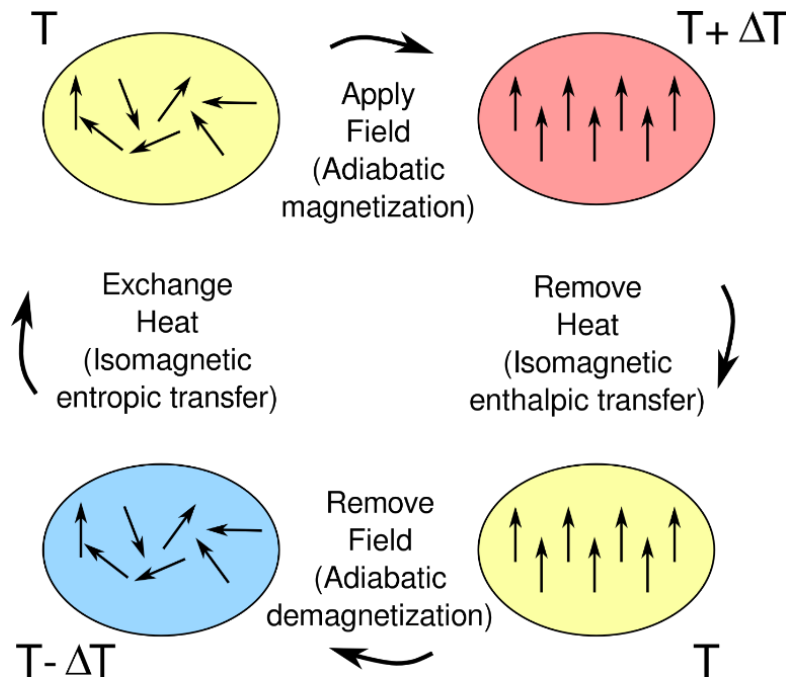


Figure 1.4. Schematic representation of a magnetic refrigeration cycle

Consider a system of randomly oriented magnetic spins at an arbitrary ambient temperature T (Fig. 1.4, top-left). Upon an adiabatic application of the magnetic field, H , the magnetic moments align along the field, and the system's temperature rises (Fig. 1.4, top-right). The generated heat is then extracted from the system using a heat transfer fluid (water, ethanol, etc), after which the system is brought to the original temperature, T , with the applied field, H , still on (Fig. 1.4, bottom-

right). The subsequent adiabatic release of the field results in a temperature decrease (Fig. 1.4, bottom-left). To return to the initial state and complete the refrigeration cycle, the system absorbs heat from the environment, where a cooling process occurs. The refrigeration cycle is repeated in order to achieve continuous cooling for practical application.

1.2.3 Design of magnetic refrigeration materials for practical applications

The magnetic refrigerators working with Gd has been shown to reach 60% cooling efficiency of the Carnot limit, compared to 40% of the best conventional gas-compression refrigerators.¹³⁻¹⁶ This high efficiency is achievable only with an applied magnetic field of 5 T. Thus, it is important to investigate alternative magnetic materials displaying larger MCE, at lower magnetic fields (2 T). Since the heating and cooling that occurs in the magnetic refrigeration cycle depends on the magnitude of the magnetic moments, a successful material must contain either a magnetically active *3d*- or *4f* elements. The magnetic entropy change, ΔS_{mag} values for the *4f* elements are expected to be large since ΔS_{mag} depends on the total quantum number J as

$$\Delta S_{\text{mag}} = -R \ln(2J + 1) \quad (6)$$

Hysteresis is another important property of MCE material and it is intrinsic to all magnetic materials. It significantly decreases the performance of a magnetic refrigerant. Therefore, a low magnetic hysteresis is needed to avoid magnetic-work losses due to the rotation of domains in a magnetic-refrigeration cycle. The hysteresis also depends on the homogeneity and purity of the material.

The material must have a high refrigerant capacity. Refrigerant capacity (Relative cooling power), q , is a measure of how much heat can be transferred from the hot to the cold sinks and vice versa, in an ideal refrigeration in one thermodynamic cycle, and it is calculated as:

$$q = \int_{\text{cold}}^{\text{hot}} \Delta S(T)_{\Delta H} dH \quad (7)$$

Therefore, a large entropy changes in a temperature range as wide as possible is needed. In terms of practicability, it is the amount of heat energy per unit volume transferred in one thermodynamic refrigeration cycle, which is the important parameter, i.e., the more denser the magnetic refrigerant the more the better its performance.¹⁸

Besides, the physical and chemical optimization methods enumerated above for enhancing the performance efficiency of MCE materials, the chemical and mechanical stability of the refrigeration refrigerants, low cost, and environmental friendliness must be addressed.

1.3 Magnetocaloric Materials

1.3.1 Gd₅T₄-based Phases (T = main group elements)

The breakthrough in the discovery of the giant MCE (GMCE) in the monoclinic Gd₅Si₂Ge₂ phase has led to extensive research in the *rare-earth*-based magnetocaloric materials.¹⁹ The Gd₅Si₂Ge₂ exhibits a magneto-structural transition and the total entropy change includes both the magnetic entropy and the structural contribution.

Two types of first-order magnetostructural transitions (from the monoclinic PM Gd₅Si₂Ge₂-type structure to the orthorhombic FM Gd₅Si₄-type structure, and from the orthorhombic AFM Sm₅Ge₄-type structure to the FM orthorhombic Gd₅Si₄-type structure) are responsible for the GMCE in the Gd₅T₄ and its related phases. All the three structures mentioned above can be distinguished by the arrangement of the interslab *T-T* dimers: (a) in the orthorhombic Gd₅Si₄-type structure, all interslab *T-T* dimers are intact (b) half of the interslab *T-T* dimers are broken in the monoclinic Gd₅Si₂Ge₂-type structure, and (c) in the orthorhombic Sm₅Ge₄-type structure, all interslab *T-T* dimers are broken (shown in Fig 1.5).

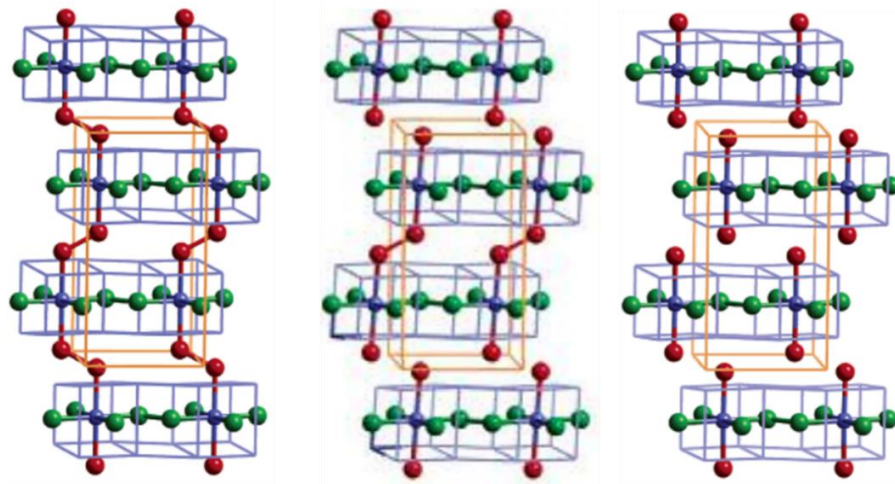


Figure 1.5. Crystal structures of orthorhombic Gd₅Si₄- (left), monoclinic Gd₅Si₂Ge₂- (middle), orthorhombic Sm₅Ge₄- (right) type structure. (Si, Ge) atoms between the slabs are in red; Gd atoms are in blue; (Si, Ge) atoms inside the slabs are in green;²⁰

Valence electron count (VEC) plays an important role in most cases in defining R_5T_4 structures. For example, a decrease in the VEC of Gd_5Ge_4 through Ga substitution leads to the formation of the interslab dimers in $Gd_5Ge_{4-x}Ga_x$.²¹ On the other hand, $Gd_5Si_{4-x}P_x$ breaks the interslab $T-T$ dimers due to an increase in the VEC in the compound.²² In addition, the interslab $T-T$ bonds can also be manipulated by modifying the T -atom size. The substitution of Si in Gd_5Si_4 with Ge and Sn led to the discovery of the dimer stretching or cleavage was discovered in $Gd_5Si_{4-x}Ge_x$ and $Gd_5Si_{4-x}Sn_x$.

1.3.2 Ni_2MnGa -based Heusler Alloys

Heusler alloys are ternary, magnetic, intermetallic alloys having basic formula X_2YZ (X and $Y = 3d$ transition elements, $Z = IIIA-VA$ group elements), where the localized magnetic moments of X and/or Y atoms influence each other via the indirect exchange interaction. They crystallize in the $L2_1$ structure with the $Fm-3m$ space group.²³ The Ni_2MnGa -based Heusler alloys are intensively studied owing to their unique and excellent magneto-structural, magneto-transport, magneto-caloric or magneto-optic properties and shape memory effect (SME), which could be attributed to a first-order martensitic transformation. The MCE of the Ni_2MnGa -based Heusler alloys were first reported in polycrystalline samples in 2000.²⁴ Under an applied magnetic field of 0.9 T, a large positive magnetic entropy change was observed at the austenitic transition temperature (TA), which is attributed to a first-order phase transition from the martensitic phase to the austenitic phase during heating.²⁵

The GMCE reported in the Ni_2MnGa -based Heusler alloys have relatively large magnetic entropy change in a large temperature range, which can be controlled by adjusting the ratio of Ni/Mn/Ga. They also have extremely flexible electronic structure and as a result, their magnetic and structural properties and their transition temperatures can easily be tuned by their composition and by external conditions.²⁶ In addition, they are also less expensive due to the absence of rare earth elements, and therefore, may be interesting as magnetic refrigerant materials. However, they exhibit low Refrigerant capacity (Relative cooling power) due to their small full width at half maximum (FWHM), which limits their applications.²⁷

1.3.3 As containing materials

MnAs compound exhibits a FOMT from an FM hexagonal NiAs-type structure to a PM orthorhombic MnP-type structure upon heating. Discovery of a large MCE in $\text{MnAs}_{1-x}\text{Sb}_x$ in 2001,⁴² shows that the FOMT is still maintained after the Sb substitution, with the T_C dropping by 35 K for $x = 0.1$. An extremely large MCE for $\text{MnAs}_{1-x}\text{Sb}_x$ ($0 \leq x \leq 0.4$) and $\text{MnAs}_{1-x}\text{Sb}_x$ ($0 \leq x \leq 0.3$) was subsequently recorded.⁴³⁻⁴⁴ The structural transformation is only possible for $x \leq 0.1$, and beyond that, a second-order magnetic transition is observed. Interestingly, the maximum magnetic entropy changes for $0 \leq x \leq 0.3$ is barely affected. The GMCE of $\text{MnAs}_{1-x}\text{Sb}_x$ in $x \leq 0.1$ is attributed to a FOMT, while the large MCE for $x > 0.1$ emanates from a metamagnetic transition above T_C .

A GMCE with a T_C of 300 K was also reported in 2002 for the $\text{MnFeP}_{0.45}\text{As}_{0.55}$ phase. By varying the As to P ratio, the T_C could be varied from 168 to 332K. While T_C increases with the As content, the magnetic entropy change peaks at $\text{MnFeP}_{0.65}\text{As}_{0.35}$. The FOMT in $(\text{MnFeP}_{1-x}\text{As}_x, 0.25 \leq x \leq 0.65, \text{ adopt the Fe}_2\text{P-type structure})$ can be characterized as magnetostriction without a change in the symmetry or relative atomic arrangement but with discontinuity in the lattice parameters. The $\text{MnFeP}_{1-x}\text{As}_x$ with $0.25 \leq x \leq 0.65$ exhibits considerable thermal hysteresis which is undesirable for practical applications.⁴⁵⁻⁴⁶

1.3.4 Laves phases

Laves phases are a group of intermetallic compounds with the general formula RT_2 (T = transition metal, and/or p-block element R = rare-earth elements).²⁸ Among the laves phases, the RCO_2 phases have received much attention in recent years because of the first-order metamagnetic transition in some of the compounds, which could lead to large magnetocaloric effect (MCE).²⁹ The heavy rare-earth ($R = \text{Dy, Ho, and Er}$) exhibit a first-order paramagnetic–ferromagnetic transition, while the other RCO_2 phases exhibit second-order ferromagnetic transition.²⁹⁻³⁰ ErCo_2 , HoCo_2 , and DyCo_2 , exhibit first-order paramagnetic-ferrimagnetic transitions at the T_C of 33, 77 and, 135 K respectively, and the maximum values of ΔS_M were about 28 J/kg K (at $T = 42$ K) for ErCo_2 , about 22 J/kg K (at $T = 84$ K) for HoCo_2 and about 14.5 J/kg K (at $T = 140$ K) for DyCo_2 under an applied field of 7 T.³¹⁻³² However, their low transition temperatures makes them less applicable as room temperature magnetic refrigerants.

Most of the recent studies on the RCO_2 systems involve the substitution of a rare-earth metal for one of the magnetic lanthanides ($\text{R}_{1-x}\text{R}'_x\text{Co}_2$; R' = other magnetic rare-earth elements) or the substitution of non-metals/transition metals for Co ($\text{RCo}_{2-x}\text{Y}_x$, Y = non-metals, Transition metal).³³⁻³⁶ The change in the ground state degeneracy of the rare-earth ion, from a magnetically ordered singlet state to a quadruplet in the paramagnetic state is responsible for the MCE in these intermetallics. Thus, substituting R atoms in RCO_2 will greatly influence the magnetic properties. The substitution of Co with Y (Y = Al, Si, Ga, Ge) in the DyCo_2 compound has been studied extensively. In all of them, the substitution leads to an increase in T_C : Ge is less effective than Si, followed by Ga and then Al; and MCE decreasing due to change from the FOMT (First Order Magnetic Transition) to SOMT (Second Order Magnetic Transition) after the substitution.³⁷⁻⁴¹

1.4 Materials in focus

Our research focus: synthesis of magnetically active intermetallic phases containing $3d$ and $4f$ metals, was based on the above-discussed principles. P elements were also incorporated to create a structurally flexible framework, which may undergo a phase transition and deliver a large entropy change. In this dissertation, the novel intermetallic materials for the study of the magnetocaloric effects are GdNiAl_2 - and RTAl (*Laves*)-based phases. Co/Ga substitution was explored for the GdNiAl_2 phase to increase structural diversity. More than one structure is found in Co/Ga substituted system of GdNiAl_2 , suggesting the possibility of GMCE if a structural transformation can be coupled with a magnetic one.

1.5 References

1. J. M. Dubois, E. Belin-Ferre, Editors. Complex Metallic Alloys: Fundamentals and Applications; 2011.
2. J. M. D. Coey, "Novel permanent magnetic materials" Phys. Scr., T 1991, T39, 21-28.
3. J. M. D. Coey, "Magnetic materials" J. Alloys Compd. 2001, 326, 2-6.
4. O. Tegus, E. Brueck, K. H. J. Buschow, F. R. de Boer, "Transition-metal-based magnetic refrigerants for room-temperature applications" Nature 2002, 415, 150-152.
5. N. A. De Oliveira, P. J. Von Ranke, M. V. Tovar Costa, A. Troper, "Magnetocaloric effect in the intermetallic compounds RCO_2 (R = Dy, Ho, Er)" Phys. Rev. B 2002, 66, 094402-1-094402/6.

6. M. H. Phan, S. C. Yu, Review of the magnetocaloric effect in manganite materials, *J. Magn. Mater.* 308 (2007) 325
7. A.M. Tishin, Y.I. Spichkin, *The Magnetocaloric Effect and its Applications*, Institute of Physics Publishing Ltd., Bristol, 2003.
8. M. Quintero, J. Sacanell, L. Ghivelder, A.M. Gomes, A.G. Leyva, F. Parisi, Magnetocaloric effect in manganites: metamagnetic transitions for magnetic Refrigeration, *Appl. Phys. Lett.* 97 (2010) 121916(1)-121916(3).
9. M. Balli, P. Fournier, S. Jandl, M.M. Gospodinov, A study of the phase transition and magnetocaloric effect in multiferroic La₂MnNiO₆ single crystals, *J. Appl. Phys.* 115 (2014) 173904(1)-173904(8).
10. E. Warburg, *Ann. Phys.* 1881, 13, 141.
11. C. J. Zimm, A. Sternberg, V. K. Pecharsky, K. A. Gschneidner Jr., M. Osborne, I. Anderson, *Adv. Cryog. Eng.* 1998, 43, 1759–1766.
12. G. J. Miller, *Chem. Soc. Rev.* 2006, 35, 799–813.
13. V. K. Pecharsky and K. A. Gschneidner, Jr., *J. Magn. Mater.* 200, 44 (1999).
14. C. B. Zimm, A. Jastrab, A. Sternberg, V. K. Pecharsky, K. A. Gschneidner, Jr., M. Osborne, and I. Anderson, *Adv. Cryog. Eng.* 43, 1759 (1998).
15. K. A. Gschneidner, Jr. and V. K. Pecharsky, *Annu. Rev. Mater. Sci.* 30, 387 (2000).
16. V. K. Pecharsky and K. A. Gschneidner, Jr., *J. Appl. Phys.* 85, 5365 (1999)
17. V. K. Pecharsky, K. A. Gschneidner, Y. Mudryk, D. Paudyal, *J. Magn. Mater.* 2009, 321, 3541-3547.
18. V. K. Pecharsky and K. A. Gschneidner Jr., *J. Appl. Phys.* 90, 4614 (2001).
19. V. K. Pecharsky and K. A. Gschneidner Jr., *Rev. Lett.* 1997, 78, 4494–4497.
20. G. J. Miller, *Chem. Soc. Rev.* 2006, 35, 799–813.
21. Y. Mozharivskyj, W. Choe, A. O. Pecharsky, G. J. Miller, *J. Am. Chem. Soc.* 2003, 125, 15183–15190.
22. V. Svitlyk, Y. Mozharivskyj, G. J. Miller, *J. Am. Chem. Soc.* 2009, 131, 2367–2374.
23. T. Graf, S.S.P. Parkin, C. Fesler, *Progr. Solid State Chem.* 39, 1 (2011).
24. F. Hu, B. Shen, J. Sun, *Appl. Phys. Lett.* 2000, 76, 3460.
25. F. Hu, B. Shen, J. Sun, G. Wu, *Phys. Rev. B* 2001, 64, 132412.

26. A. Planes, I. Mañosa, M. Acet, J. Phys.: Condens. Matter 2009, 21 233201.
27. B. Ingale, R. Gopalan, M. M. Raja, V. Chandrasekaran, S. J. Ram, Appl. Phys. 2007, 102, 22–27.
28. F. Stein, M. Palm, G. Sauthoff, Intermetallics 2004, 12, 713–720.
29. N. H. Duc, D. T. Kim Anh, P. E. Brommer, Phys. B 2002, 319, 1–8.
30. N. H. Duc, D. T. K. Anh, J. Magn. Magn. Mater. 2002, 242–245, 873–875.
31. S. Khmelevskiy, P. Mohn, The order of the magnetic phase transitions in RCo₂. J. Phys.: Condens. Matter 2000, 12, 9453–9464.
32. N. K. Singh, S. K. Tripathy, D. Banerjee, C. V. Tomy, K. G. Suresh A. K. Nigam. Journal of Magnetism and Magnetic Materials 317 (2007) 68–79.
33. D. Wang, H. Liu, S. Tang, S. Yang, S. Huang, Y. Du, Phys. Lett. 2002, A 297 247.
34. N. H. Duc, D. T. K. Anh P. E. Brommer, Physica B. 2002 319 1
35. A. M. Gomes, M. S. Reis, I. S. Oliveira, A. P. Guimaraes, A. Y. Takeuchi, J. Magn. Magn. Mater. 2002, 242–245 870.
36. H. Wada, Y. Tanabe, M. Shiga, H. Sugawara, H. Sato, J. Alloys Compounds. 2001, 316 245.
37. D. H. Wang, H. D. Liu, S. L. Tang, T. Tang, J. F. Wen, Y. W. Du, Solid State Commun. 2002, 121 199.
38. H. Liu, D. Wang, S. Tang, Q. Cao, T. Tang, B. Gu, Y. Du, J. Alloys Compounds. 2002, 346 314.
39. Y. Wang, S. Yang, X. Song, J. Alloys Compounds. 2003, 354 81.
40. D. Wang, S. Tang, H. Liu, W. Zhong, Y. Du, Mater. Lett. 2003, 57 3884.
41. N. K. Singh, K. G. Suresh, A. K. Nigam, 2003 Solid State Commun. 2003, 127 373.
42. H. Wada, Y. Tanabe, Appl. Phys. Lett. 2001, 79, 3302.
43. H. Wada, K. Taniguchi, Y. Tanabe, Mater. Trans. 2002, 43, 73–77
44. H. Wada, T. Morikawa, K. Taniguchi, T. Shibata, Y. Yamada, Y. Akishige, Phys. B 2003, 328, 114–116.
45. O. Tegus, E. Bruck, L. Zhang, Dagula, K. H. J. Buschow, F. R. De Boer, Phys. B 2002, 319, 174–192.

46. K. A. Gschneider Jr., V. K. Pecharsky, A.O. Tsokol, Reports Prog. Phys. 2005, 68, 1479–1539

CHAPTER 2. SIGNIFICANTLY ENHANCED CURIE TEMPERATURE OF TERNARY LAVES PHASES $\text{RCr}_{0.4}\text{Al}_{1.6}$ and RZnAl ($\text{R} = \text{Tb, Dy, Ho}$)

We begin our research into the study of the magnetostructural relationships in rare-earth transition-metal aluminides by investigating the substitutions of Cr and Zn in the Al site in RAl_2 . In an attempt to verify the effect of valence electron concentration (VEC) on the different structural ($\text{Cu \& Ni} = P\bar{6}2m$, $\text{Co \& Fe} = P6_3/mmc$, $\text{Mn} = Fd\bar{3}m$) and magnetic properties observed in first-row transition metal ternary Laves phases, we investigate some of the remaining first-row transition metals ($\text{RCr}_{0.4}\text{Al}_{1.6}$, RZnAl ; $\text{R} = \text{Tb, Dy, Ho}$). Our studies show that with a fixed R, the magnetic behavior of these two systems strongly depends on the nature of the transition metal. A comparison with the previously studied RTAl phases made ($\text{R} = \text{Tb, Dy, Ho}$; $\text{T} = \text{Cu, Ni, Co, Fe, Mn}$). In this chapter, the structural, magnetocaloric, transport, and magnetic properties of $\text{RCr}_{0.4}\text{Al}_{1.6}$ and RZnAl (Tb, Dy, Ho) are reported.

2.1 Introduction

Ternary Laves phases are a group of intermetallic compounds with the general formula RTX ($\text{T} = \text{transition metal}$, $\text{X} = \text{p-block element}$, $\text{R} = \text{rare earth}$).¹ They crystallize in one of the following binary Laves structure types: hexagonal MgNi_2 (C36), cubic MgCu_2 (C15), and hexagonal MgZn_2 (C14) and, which differ only by the particular stacking of the same four-layered structural units.² These types of Mg binary Laves systems are isostructural to a vast number of ternary intermetallic compounds.³ Hamm et al. studied the ternary Laves phases $\text{Ti}_2\text{M}_3\text{Si}$ ($\text{M} = \text{Fe, Co}$) that crystallize in the hexagonal MgZn_2 -type structure with $P6_3/mmc$ space group.⁴ Henriques et al. and Verniere et al. also studied recently the magnetism of the ternary $\text{U}_2\text{Fe}_3\text{Ge}$ and $\text{U}_2\text{Os}_3\text{Si}$ that adopts the hexagonal MgZn_2 and MgCu_2 -type structure respectively.⁵⁻⁶ The vast majority of the RTX compounds also adopt one of the aforementioned structures or their ordered variant.⁷

These types of RTX intermetallic compounds display some of the rich structural and compositional diversity which endows them with a wide variety of physical properties including, magnetic polaronic behavior, intermediate valency, Kondo effect, multiple magnetic transitions, large Magnetocaloric effect (MCE), heavy fermion behavior, large Magnetoresistance (MR), spin glass state, superconductivity, metamagnetism, spin-orbital compensation, and pseudogap effect.⁸⁻

¹⁴ Interest in this Laves compounds stemmed initially from the discovery of the interesting and technologically relevant physical phenomena, including giant MCE, giant magnetostriction, colossal MR in their binary variants.¹⁵⁻¹⁷ Interesting magnetostrictive properties were discovered in the RFe_2 (Sm, Tb) compound.¹⁸ RT_2 (T = Co, Al; R = Gd, Tb, Dy, Ho, Er) cubic binary Laves phases have also been widely studied because of their large MCEs at low to moderate temperatures.¹⁹⁻²⁰

Among the RTX based compounds, the equiatomic ternary aluminides RTAl series are a subject of exceptional consideration. They exhibit a plethora of interesting and technologically relevant phenomena such as giant MCE, giant magnetostriction, colossal MR.²¹⁻²² These RTAl compounds possess varied magnetic phase transitions and display complex magnetic structures which can induce interesting MCE properties.²³⁻²⁵

The properties of these ternary aluminides also depend on the history of the sample. The well-known example is GdTAI (T = Co, Ni, Cu, Rh, Pd).²⁶ In addition, these compounds exhibit one of the broadest structural diversity crystallizing in different crystal structures which is rare-earth dependent and therefore, provide an opportunity to study the variation of their properties with the underlying structural diversity.²⁷ The light rare-earth of $RFeAl$ except for R = La, crystallize in the $MgCu_2$ -type, while heavy rare-earth compounds show $MgZn_2$ -type structure.²⁸⁻²⁹ More so, the light rare earth $RCoAl$ discovered to be unstable, while the $RCoAl$ (Gd-Lu) of heavy rare counterparts adopt the $MgZn_2$ structure.³⁰ The RTAl (T = Ni, Cu; R = Ce–Nd, Sm, Gd, Lu) variant adopts the $MgNi_2$ -type structure together with the iso-structural transition in some of them.³¹

Among the RTAl ternary system, the $RMnAl$ crystallizing in the cubic $MgCu_2$ -type structure, displays a high Curie temperature,³² higher than those crystallizing in the hexagonal $MgZn_2$ and $MgNi_2$ ($RCuAl$, $RNiAl$, $RCoAl$, $RFeAl$).³³⁻³⁷ The increase in the curie temperature from Cu to Mn is attributed to the change in structure from hexagonal to cubic phase.³⁸ It is also attributed to the decrease in the number of d-electrons at the Fermi level.³⁸ The change in the number of delocalized 3d electrons across the transition metal series leads to considerable effects on the DOS at the Fermi level and plays a significant role in determining the magnetic properties.³⁸ Based on the aforementioned properties, it is of interest to investigate the early transition metal-based RTAl systems with the aim of further understanding the structure-property relations and optimizing their properties.

Herein we report on the synthesis, crystal structures, transport properties, magnetic properties, and electronic band structures of the $\text{RCr}_{0.4}\text{Al}_{1.6}$ and RZnAl ($\text{R} = \text{Tb, Dy, Ho}$) series of compounds. From the Powder X-ray diffraction structure refinements, these phases were confirmed to adopt the MgCu_2 and MgZn_2 -type structure for the RCrAl and RZnAl respectively. Magnetic susceptibility measurements revealed ferromagnetic and ferrimagnetic behavior for these analogs. Electrical resistivity measurement and Electronic band structure calculations suggest that $\text{RCr}_{0.4}\text{Al}_{1.6}$ and RZnAl exhibits a metallic behavior.

2.2 Experimental details

2.2.1 Synthesis

General Details. The following reagents were used as received: Finely dispersed powder of terbium (Alfa Aesar, 99.9%), dysprosium powder (Alfa Aesar, 99.9%), holmium powder (Alfa Aesar, 99.9%), chromium powder (Alfa Aesar, 99.9%) and zinc powder (Alfa Aesar, 99.9%). All manipulations during sample preparation were carried out in an argon-filled glovebox (content of $\text{O}_2 < 0.5$ ppm)

Synthesis of $\text{RCr}_{0.4}\text{Al}_{1.6}$. The $\text{TbCr}_{0.4}\text{Al}_{1.6}$, $\text{DyCr}_{0.4}\text{Al}_{1.6}$, and $\text{HoCr}_{0.4}\text{Al}_{1.6}$ compounds were prepared by arc-melting of stoichiometric amounts of rare earth, Cr, and Al. Each compound was re-melted four times to ensure homogeneity.

Synthesis of RZnAl . The TbZnAl , DyZnAl , and HoZnAl compounds were pressed into pellets without arc-melting them. All the samples were placed in coat-ed quartz tubes, sealed and annealed at 1273 K for 7days in an argon atmosphere and subsequently quenched in air

2.2.2 Physical property Measurements

Magnetic and resistivity measurements of $\text{RCr}_{0.4}\text{Al}_{1.6}$ and RZnAl ($\text{R} = \text{Tb, Dy, Ho}$), were carried out on a Quantum Design Magnetic Property Measurement System using the Quantum Design superconducting quantum interference device (SQUID) Magnetometer option and the Physical Property Measurement System, respectively. Both zero-field cooled (ZFC) and field cooled (FC) measurements have been performed in the 2-400 K temperature range with an applied field up to 0.1 T. Field-dependent magnetization measurements were performed at 2 K and above room temperature. The temperature dependence Electrical resistivity measurements were carried

out using the standard four-probe DC technique in the temperature-dependent resistivity measurements were also performed at 2 K with an applied field up to 7 T.

2.2.3 Structure Determination

Powder X-ray diffraction (PXRD) measurement was performed on the respective crushed pellets of $\text{RCr}_{0.4}\text{Al}_{1.6}$ and RZnAl to determine the homogeneity and phase purity of samples and was performed using a PANalytical Empyrean X-ray Powder Diffractometer operating at 45 kV/40 mA with (Cu $\text{K}\alpha 1$, $\lambda = 1.540598$) radiation. The lattice parameters and crystal structure of the samples were analyzed by Rietveld refinement using the FULLPROF software.

2.3 Results and Discussion

2.3.1 Crystal Structure

Crystal structure determinations revealed that the $\text{RCr}_{0.4}\text{Al}_{1.6}$ and RZnAl phases crystallize in the MgCu_2 -type (Fd-3m) and MgZn_2 -type (P6₃/mmc) structure (Figure 2.1) respectively. The majority component atoms create a 3D network that is made up of B_4 tetrahedra. These tetrahedra are arranged in the same manner as the individual atoms in the cubic and hexagonal diamond, respectively. The Mg atoms in these two structures also are arranged in the respective diamond networks so their crystal structures can be described as two inter-penetrating diamond networks. The Cu/Zn atoms form layers which are referred to as Kagomé nets. These layers of Kagomé nets are separated by other Cu/Zn atom planes. Depending on the stacking of these Kagomé nets, the two different basic structures arise: the cubic stacking found in MgCu_2 is described as (ABC) stacking; the stacking found in hexagonal MgZn_2 is (AB) stacking.

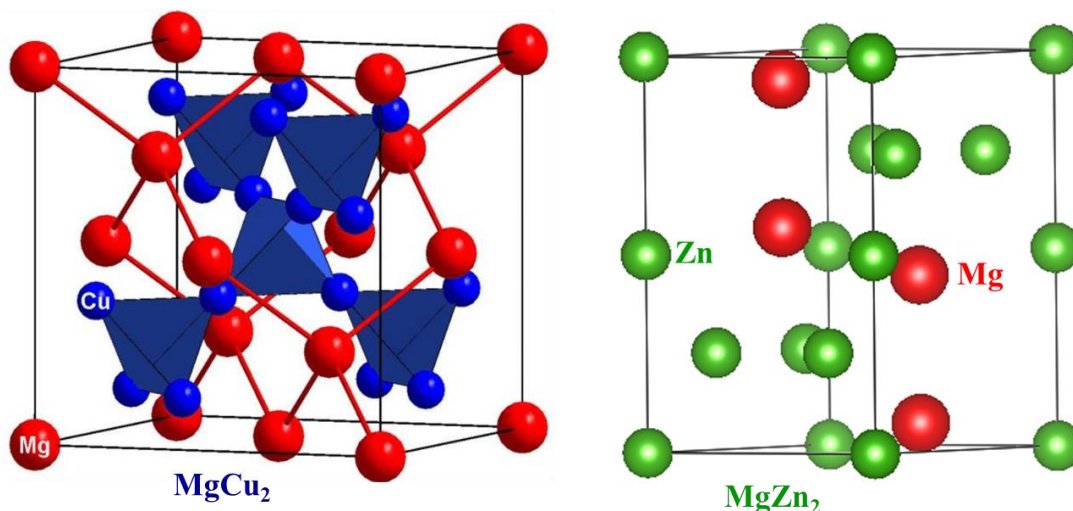


Figure 1.6. Crystal structure of MgCu_2 (left) and MgZn_2 (right) type structure

2.3.2 Structural Characterization

The compounds $\text{RCr}_{0.4}\text{Al}_{1.6}$, and RZnAl ($\text{R} = \text{Tb}, \text{Dy}, \text{Ho}$) Laves phases were analyzed using powder X-ray diffraction (PXRD). Their PXRD data were refined using the hexagonal MgZn_2 -type with space group $\text{P6}_3/\text{mmc}$ and the cubic ($\text{Fd-}3\text{m}$) MgCu_2 -type structural model respectively. The refined lattice parameters from Rietveld refinements are listed in Table 1. As can be seen from Table 2.1, the lattice parameters and unit cell volume of RZnAl and $\text{RCr}_{0.4}\text{Al}_{1.6}$ decrease with increasing atomic numbers of rare earth element due to the change in the atomic radii of R.

Figure 2.2 shows the Rietveld refinements for PXRD data for RZnAl and $\text{RCr}_{0.4}\text{Al}_{1.6}$ ($\text{R} = \text{Tb}, \text{Dy}, \text{Ho}$). All the compounds contain secondary phases as impurities as shown in Figure 2.2a-b. The Rietveld refinement of all the compounds showed that the major phases contain about 90-95 wt% of the MgZn_2 -type (RZnAl) and MgCu_2 -type ($\text{RCr}_{0.4}\text{Al}_{1.6}$) with the remaining wt% distributed among the impurities.

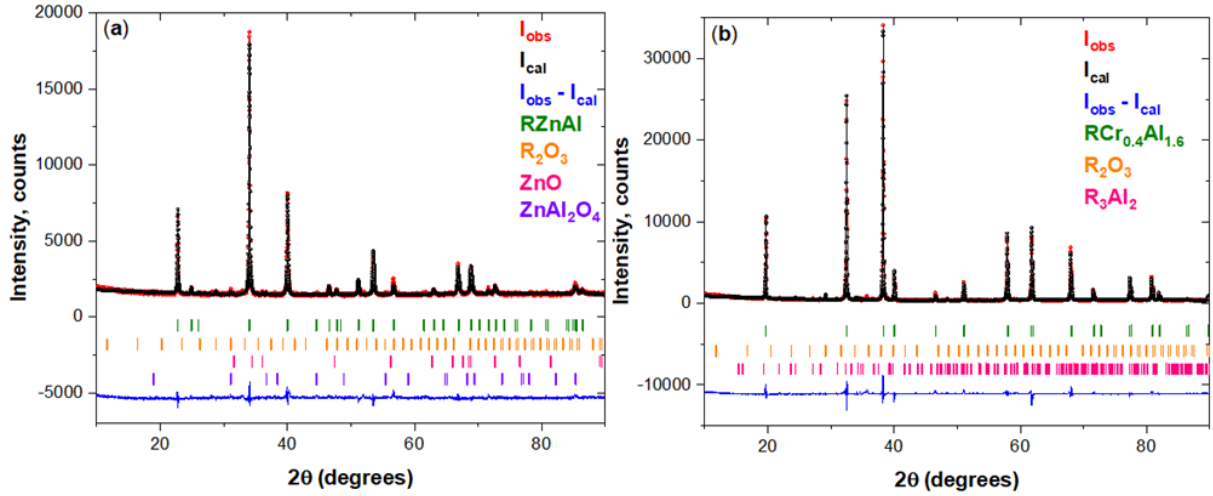


Figure 1.7. Rietveld refinement of the powder X-ray diffraction patterns of (a) RZnAl, and (b) RCr_{0.4}Al_{1.6}.

Table 2.1. Lattice parameters of RZnAl and RCr_{0.4}Al_{1.6}.

Compound	a/Å	c/Å	V/Å ³
TbCr _{0.4} Al _{1.6}	7.78200		471.273
DyCr _{0.4} Al _{1.6}	7.75600		466.567
HoCr _{0.4} Al _{1.6}	7.75551		466.479
TbZnAl	4.50103	7.15274	125.503
DyZnAl	4.48837	7.08438	123.433
HoZnAl	4.49616	7.03617	123.183

2.3.3 Magnetic Properties

2.3.3.1 RCr_{0.4}Al_{1.6} (R = Tb, Dy, Ho) phase

Magnetization and inverse magnetic susceptibility as a function of the temperature of RCr_{0.4}Al_{1.6} compounds are shown in Fig. 2.3. The TbCr_{0.4}Al_{1.6} exhibit ferromagnetic transitions at 190 K (Fig. 2.3a). The DyCr_{0.4}Al_{1.6} and HoCr_{0.4}Al_{1.6} in a field of 0.1 T show Curie temperature (T_c) of 110 K, and 20 K (Fig. 2.3b and c) respectively. DyCr_{0.4}Al_{1.6} also shows a possible spin-reorientation transition at 50 K (Fig. 2.3b). The paramagnetic susceptibility of TbCr_{0.4}Al_{1.6}, DyCr_{0.4}Al_{1.6} and HoCr_{0.4}Al_{1.6} follows Curie–Weiss law in 0.1 T (see insets in Fig. 2.3a-c). The fit to the Curie–Weiss law yields a paramagnetic Weiss temperature of 35 K and 10 K and -36 K indicating a ferromagnetic dominant interaction in (TbCr_{0.4}Al_{1.6}, DyCr_{0.4}Al_{1.6}) and an

antiferromagnetic nearest-neighbor interaction in $\text{HoCr}_{0.4}\text{Al}_{1.6}$. The fit also yielded an effective magnetic moment per formula unit (M_{eff}/fu) of 10.01, 10.98, and 10.85 μ_B for $\text{TbCr}_{0.4}\text{Al}_{1.6}$, $\text{DyCr}_{0.4}\text{Al}_{1.6}$ and $\text{HoCr}_{0.4}\text{Al}_{1.6}$ respectively. These M_{eff}/fu values yield effective magnetic moments of 2.39 μ_B/Cr in $\text{TbCr}_{0.4}\text{Al}_{1.6}$, 2.67 μ_B/Cr in $\text{DyCr}_{0.4}\text{Al}_{1.6}$ and 2.27 μ_B/Cr in $\text{HoCr}_{0.4}\text{Al}_{1.6}$ (assuming that Tb, Dy, and Ho have the theoretical effective moment of 9.72, 10.65 and 10.61 μ_B respectively).

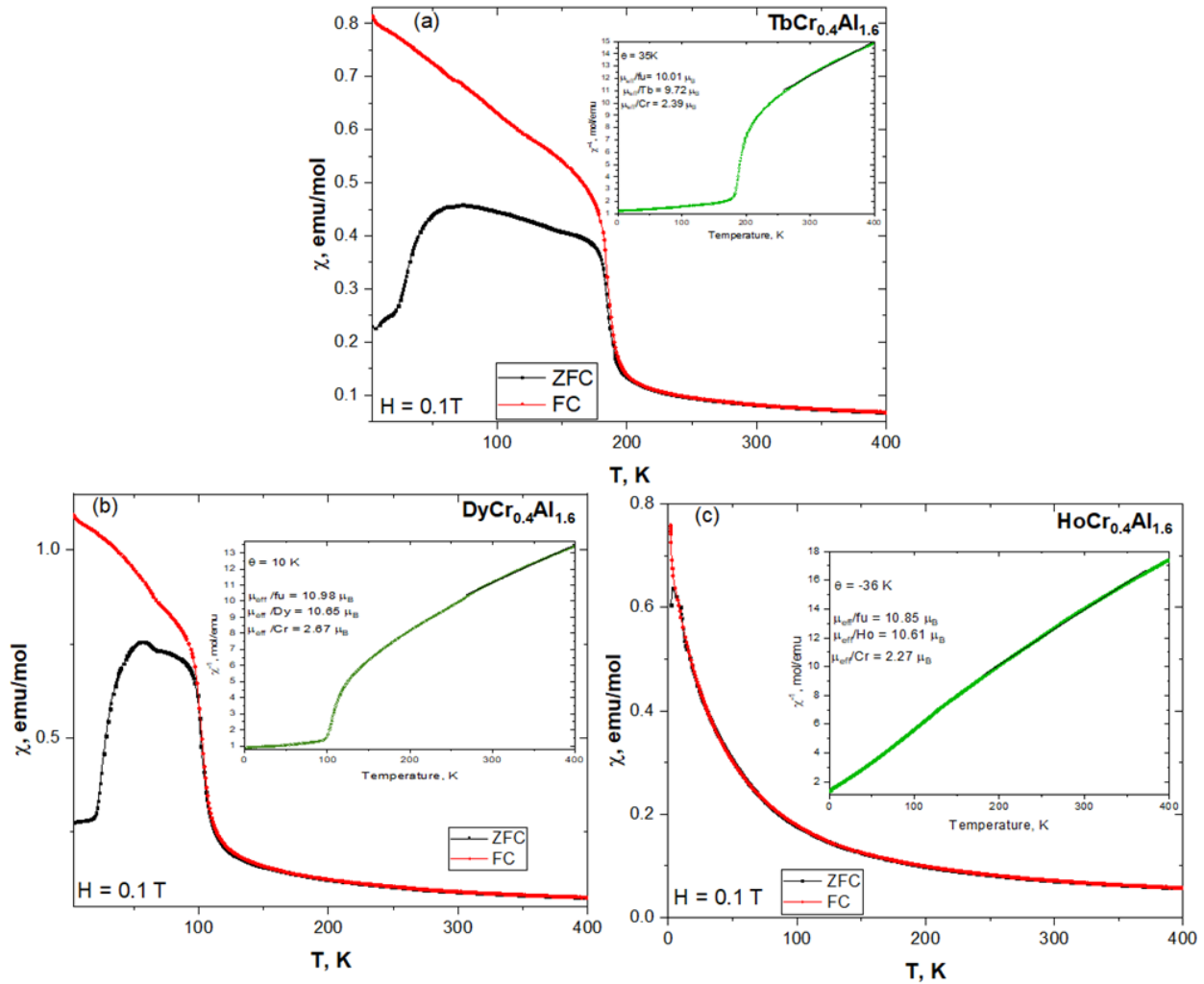


Figure 1.8. Magnetization vs temperature of (a) $\text{TbCr}_{0.4}\text{Al}_{1.6}$, (b) $\text{DyCr}_{0.4}\text{Al}_{1.6}$ and (c) $\text{HoCr}_{0.4}\text{Al}_{1.6}$ compounds in applied field of 0.1 T.

The isothermal field-dependent magnetization examined at different temperatures are shown in (Fig. 2.4a-c). The magnetization vs field data of $\text{TbCr}_{0.4}\text{Al}_{1.6}$ and $\text{DyCr}_{0.4}\text{Al}_{1.6}$ shows similar behavior at all temperatures. They behave as a hard ferrimagnet at 2 K and 10 K with a

decrease in the hysteresis from 2 K to 10 K (Fig. 2.4a-b). They became soft after 10 K with zero residual magnetization and coercive field and showed a linear behavior at 300 K suggesting weak antiferromagnetism at higher temperatures. $\text{HoCr}_{0.4}\text{Al}_{1.6}$ however, behaves as a soft ferrimagnet at all measured temperatures (2, 10, 300 K) with zero residual magnetization and coercive field (Fig. 2.4c). The magnetization value for all the three compounds at 2 K does not saturate even at 7 T. The saturation magnetization value, obtained at 2 K, reaches values of $2.3 \mu_B/\text{fu}$ for $\text{TbCr}_{0.4}\text{Al}_{1.6}$, $3.2 \mu_B/\text{fu}$ for $\text{DyCr}_{0.4}\text{Al}_{1.6}$ and $4.5 \mu_B/\text{fu}$ for $\text{HoCr}_{0.4}\text{Al}_{1.6}$. These magnetic saturation values (Fig. 2.4a-c) are lower than the theoretical ordered moment of Tb ($9 \mu_B$), Dy ($10 \mu_B$), and Ho ($10 \mu_B$). This reduction of the observed moment values in $\text{TbCr}_{0.4}\text{Al}_{1.6}$, $\text{DyCr}_{0.4}\text{Al}_{1.6}$, and $\text{HoCr}_{0.4}\text{Al}_{1.6}$ suggest a possible antiferromagnetic coupling between the rare-earth and the transition metal sublattices.

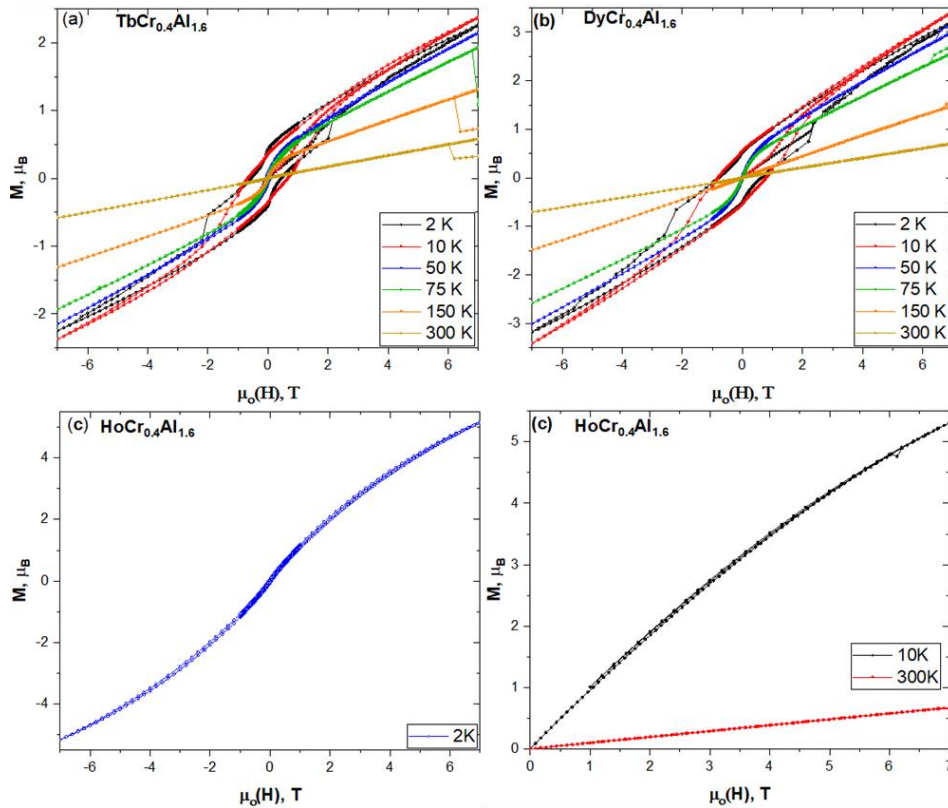


Figure 1.9. Magnetization vs. magnetic field data of (a) $\text{TbCr}_{0.4}\text{Al}_{1.6}$ at 2 K, 10 K, 50 K, 75 K, 150 K, 300 K (b) $\text{DyCr}_{0.4}\text{Al}_{1.6}$ at 2 K, 10 K, 50 K, 75 K, 150 K, 300 K and (c) $\text{HoCr}_{0.4}\text{Al}_{1.6}$ at 2 K, 10 K and 300 K.

2.3.3.2 RZnAl (R = Tb, Dy, Ho) phase

Figure 2.5 shows the temperature dependence of magnetization for the RZnAl compounds measured at 0.1 T. From the field-cooled (FC) and zero-field cooled (ZFC) curves, we can clearly observe that strong ferromagnetic behavior in TbZnAl and DyZnAl with a curie temperature of 130 K and 105 K (Fig. 2.5a-b) for TbZnAl and DyZnAl respectively. In addition, DyZnAl shows a cusp in magnetization at 50 K (T_N). The divergence in the zfc-fc curve is an indication of magnetic anisotropy in these compounds. The HoZnAl, however, shows a ferrimagnetic behavior at T_c equal to 20 K (Fig. 2.5c). The high-temperature magnetization data are fitted with the Curie–Weiss law (shown in Fig. 5a-c as insets). The effective paramagnetic moment obtained from the fit is $\mu_{\text{eff}}/\text{fu} = 10.93, 11.05, \text{ and } 10.69 \mu_B$, for TbZnAl, DyZnAl and HoZnAl respectively. These values are close to the expected trivalent effective paramagnetic moment ($\mu_{\text{theor}} = 9.72 \mu_B/\text{Tb}, 10.65 \mu_B/\text{Dy}, \text{ and } 10.61 \mu_B/\text{Ho}$). The Curie–Weiss temperature(θ_p) of TbZnAl, DyZnAl, and HoZnAl is found to be 94 K, 64 K, and -8 K respectively. The positive and negative signs of θ_p indicate that the magnetic interaction is ferromagnetic and antiferromagnetic, respectively.

Table 2.2. Magnetic properties of $\text{RCr}_{0.4}\text{Al}_{1.6}$ and RZnAl (R = Tb, Dy, Ho) compounds: Curie temperature (T_c), saturation magnetization per formula unit M_{sat}/fu at 2K and effective magnetic moment per formula unit (M_{eff}/fu) and per transition metals (M_{eff}/T).

Compound	M_{eff}/fu (μ_B)	M_{eff}/T (μ_B)	M_{sat}/fu (μ_B)	T_c (K)
TbCr _{0.4} Al _{1.6}	10.01	2.39	2.30	190
DyCr _{0.4} Al _{1.6}	10.98	2.67	3.20	110
HoCr _{0.4} Al _{1.6}	10.85	2.27	5.10	16
TbZnAl	10.93	-	6.20	130
DyZnAl	11.05	-	6.00	105
HoZnAl	10.69	-	5.70	20

The field-dependent magnetization $M(H)$ data measured at different temperatures are shown in (Fig. 2.6a-c). At 2 K, HoZnAl, which shows a soft magnet characteristic (Fig. 2.6c), TbZnAl and DyZnAl exhibit a hard ferromagnet behavior with a large hysteresis (Fig. 2.6a and b). This hysteresis in TbZnAl and DyZnAl disappear with an increase in temperature as shown in Fig. 2.6a and b. The magnetization of TbZnAl, DyZnAl, and HoZnAl saturates above 6 T with a

saturation moment of 6.2, 5.8, and 5.5 μ_B/fu respectively at 2 K (Fig. 2.6a-c), smaller than that obtained at high temperatures. This is consistent with an antiferromagnetism interaction between the rare-earth sublattices. The results of magnetization measurements of the $\text{RCr}_{0.4}\text{Al}_{1.6}$ and RTAl ($\text{R} = \text{Tb}, \text{Dy}, \text{Ho}$) are summarized in Table 2.2.

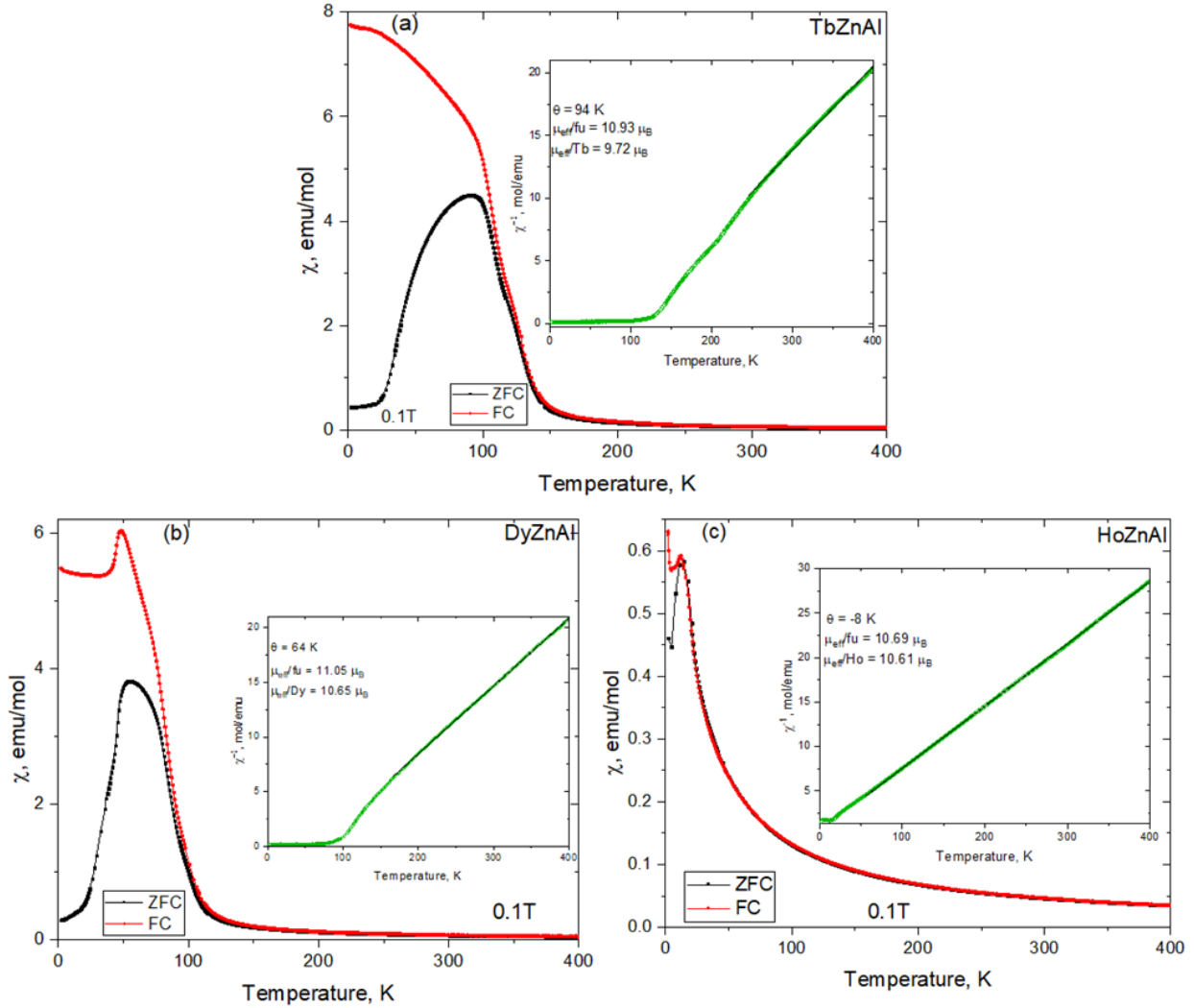


Figure 1.10. Magnetization vs temperature of (a) TbZnAl , (b) DyZnAl , and (c) HoZnAl compounds in an applied field of 0.1 T.

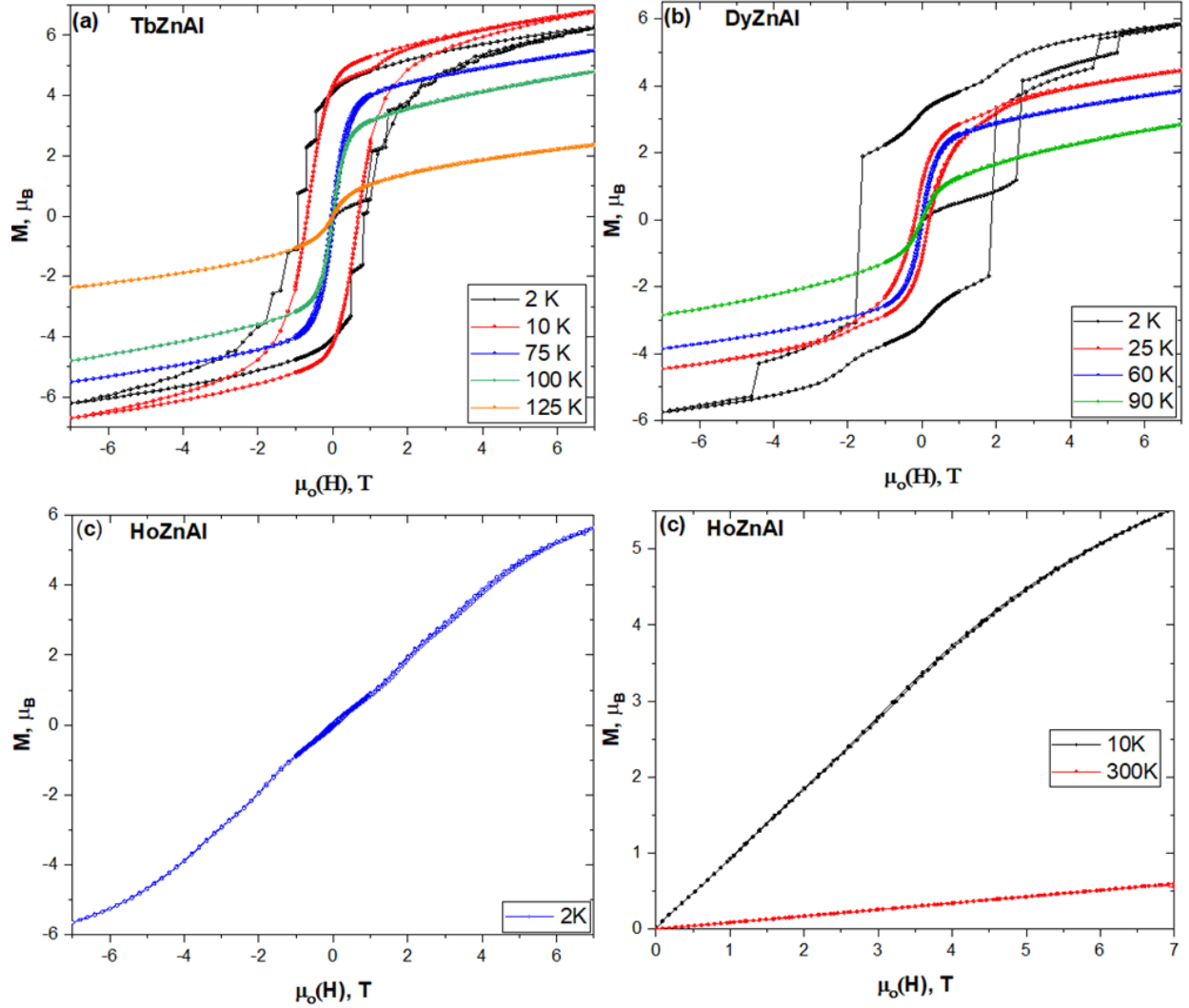


Figure 1.11. Magnetization vs. magnetic field data of (a) TbZnAl at 2 K, 10 K, 75 K, 100 K, 125 K (b) DyZnAl at 2 K, 25 K, 60 K, 90 K, and (c) HoZnAl at 2 K, 10 K and 300 K.

2.3.4 Magnetocaloric Effect

The temperature dependence of magnetic entropy change $\Delta S_M(T)$ for $RZnAl$ and $RCr_{0.4}Al_{1.6}$ was estimated from the $M(H, T)$ curves under various magnetic field changes (ΔH) by using Maxwell's thermodynamic equation,

$$\Delta S_M = - \int^H (\partial M / \partial T)_H dH$$

The $-\Delta S_M(T)$ curves for $RZnAl$ and $RCr_{0.4}Al_{1.6}$ for ΔH from 0 to 2 to 0–5 T is shown in Fig. 2.7a-c and 2.7d-f, respectively. As shown in the figures, for each sample and field change, ΔS_M initially increases with increasing temperature and peaks near their respective T_C 's. With further increase

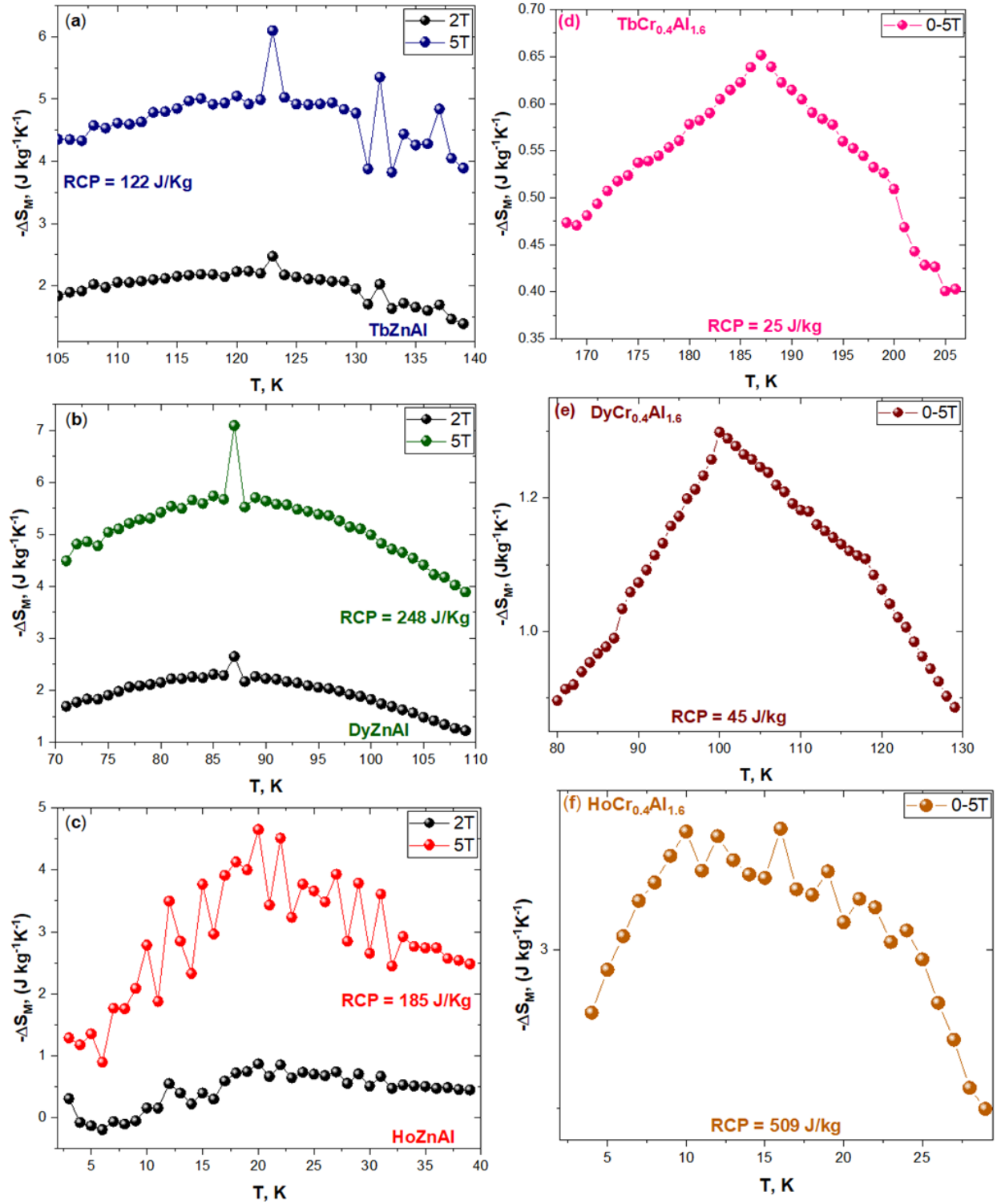


Figure 1.12. Isothermal magnetic entropy changes for (a) TbZnAl, (b) DyZnAl, (c) HoZnAl, for magnetic changes of $\mu_0\Delta H = 2\text{ T}$ and 5 T . (d) TbCr_{0.4}Al_{1.6}, (e) DyCr_{0.4}Al_{1.6} and (f) HoCr_{0.4}Al_{1.6} for magnetic changes of $\mu_0\Delta H = 5\text{ T}$

of the temperature, ΔS_M decreases with increasing temperature. The peak values of the entropy change for RZnAl at 2T are $2.5 \text{ J kg}^{-1}\text{K}^{-1}$, $2.7 \text{ J kg}^{-1}\text{K}^{-1}$, and $0.9 \text{ J kg}^{-1}\text{K}^{-1}$ for TbZnAl, DyZnAl, and HoZnAl respectively. For a field change of 5T the samples exhibit a peak ($-\Delta S_M$) of $6.1 \text{ J kg}^{-1}\text{K}^{-1}$, $7.1 \text{ J kg}^{-1}\text{K}^{-1}$, $4.7 \text{ J kg}^{-1}\text{K}^{-1}$, $1.38 \text{ J kg}^{-1}\text{K}^{-1}$, $1.41 \text{ J kg}^{-1}\text{K}^{-1}$ and $3.38 \text{ J kg}^{-1}\text{K}^{-1}$ for TbZnAl, DyZnAl, HoZnAl, TbCr_{0.4}Al_{1.6}, DyCr_{0.4}Al_{1.6} and HoCr_{0.4}Al_{1.6} respectively. The entropy change values for the RZnAl compounds remain relatively high throughout the entire temperature change. This makes them potential MCE materials for low-temperature applications.

Table 2.3. The T_C , $-\Delta S_M^{\max}$, and RCP for $\Delta H = 0-5 \text{ T}$ for RZnAl and HoCr_{0.4}Al_{1.6} as well as some selected low-temperature magnetocaloric materials.

Compound	T_C (K)	$-\Delta S_M(\text{Jkg}^{-1}\text{K}^{-1})$	RCP(Jkg ⁻¹)	ref.
TbCoAl	70	10.4	-	35
TbNiAl	48	13.8	494	23
TbCuAl	52	14.4	-	41
TbZnAl	121	6.1	122	This work
DyFeAl	128	6.4	595	34
DyCoAl	37	16.3	-	35
DyNiAl	30	19.0	-	21
DyCuAl	27	20.4	423	42
DyZnAl	87	7.1	248	This work
HoCr _{0.4} Al _{1.6}	16	3.38	509	This work
HoCoAl	10	21.5	-	35
HoNiAl	14	23.6	500	13
HoCuAl	11.2	30.6	486	43
HoZnAl	20	4.87	185	This work

The relative cooling power (RCP) is an important quality factor for the MCE material which can identify the amount of heat that can be transferred from the hot to the cold sinks and vice versa, in an ideal magnetic refrigeration cycle. The value of RCP is evaluated as, $RCP = -\Delta S_M \times \delta T_{FWHM}$, where δT_{FWHM} is the full width at half maximum and $-\Delta S_M^{\max}$ is the maximum of magnetic entropy change. Under the field of 5T, the values of the RCP for TbZnAl, DyZnAl, HoZnAl, TbCr_{0.4}Al_{1.6}, DyCr_{0.4}Al_{1.6} and HoCr_{0.4}Al_{1.6} are 122 Jkg^{-1} , 248 Jkg^{-1} , 185 J kg^{-1} , 25 J kg^{-1} , 45 J kg^{-1} and 509 J kg^{-1} respectively. These values are comparable to other RTAl compounds as shown in Table 2.3.

2.3.5 Magnetoresistance (MR) Effect

In order to understand the multiple magnetic transitions in $\text{DyCr}_{0.4}\text{Al}_{1.6}$ and DyZnAl , we measured the electrical resistivity as a function of temperature as shown in Fig. 8. The resistivity of $\text{DyCr}_{0.4}\text{Al}_{1.6}$ shows a purely metallic behavior from 2 K to 270 K (Fig. 2.8a) as the resistivity increases linearly with temperature. With an increase of temperature, ρ reaches a maximum at around 270 K and then decreases with a further increase in temperature. This decrease in resistivity with increasing temperature is an indication of a semiconductor behavior. The change from metallic to semiconducting behavior has been observed for some other RTX compounds and the hydrides of many laves phases.³⁹⁻⁴⁰ The origin of the resistivity maximum at 270 K is not known at this point as there is no magnetic transition at 270 K in M vs T plot of $\text{DyCr}_{0.4}\text{Al}_{1.6}$ (Fig. 2.3b). The temperature dependence of the electrical resistivity of DyZnAl is shown in Fig. 2.8b.

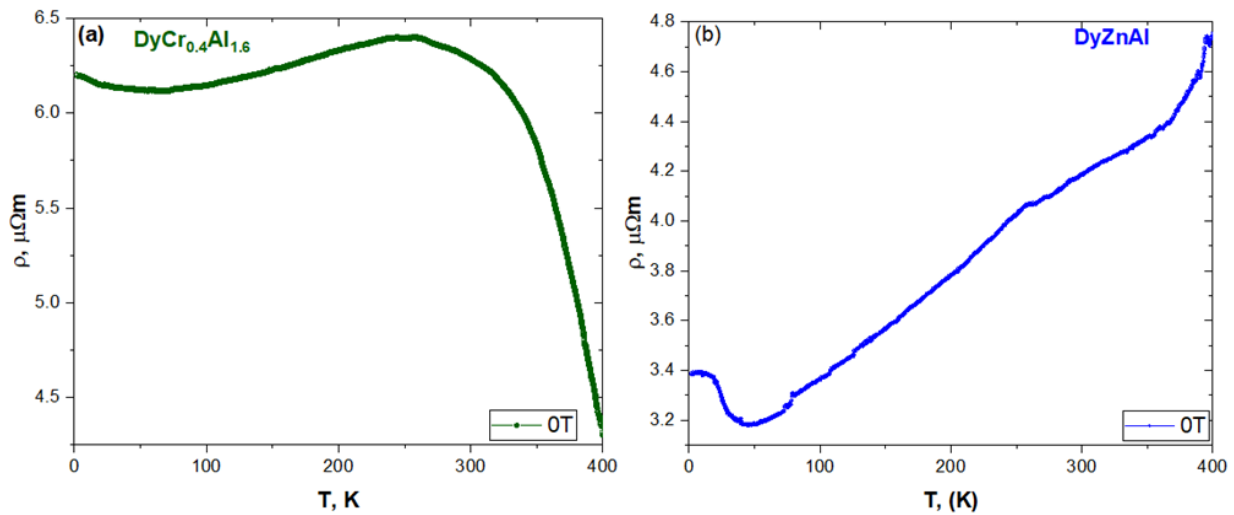


Figure 1.13. Resistivity as a function of temperature at zero magnetic field of (a) $\text{DyCr}_{0.4}\text{Al}_{1.6}$ and (b) DyZnAl .

At high temperatures, the resistivity of DyZnAl exhibits good linearity, suggesting a metallic behavior. With a decrease in temperature, the resistivity reaches a minimum at around 50 K and then increases with a further decrease in temperature. The resistivity minimum at the 50 K corresponds to the antiferromagnetic transition, observed in the magnetization versus temperature plot (Fig. 4b) of DyZnAl . The presence of a resistivity minimum at low temperatures might be attributed to Kondo-effect, which is the scattering conducting electrons by the magnetic Dy. Fig.

2.9 illustrates the magnetoresistance (MR), $[p(H)-p(0)]/p(0) \times 100\%$, as a function of the magnetic field up to 7T measured at 2 K. Where the $p(H)$ and $p(0)$ are the resistivities.

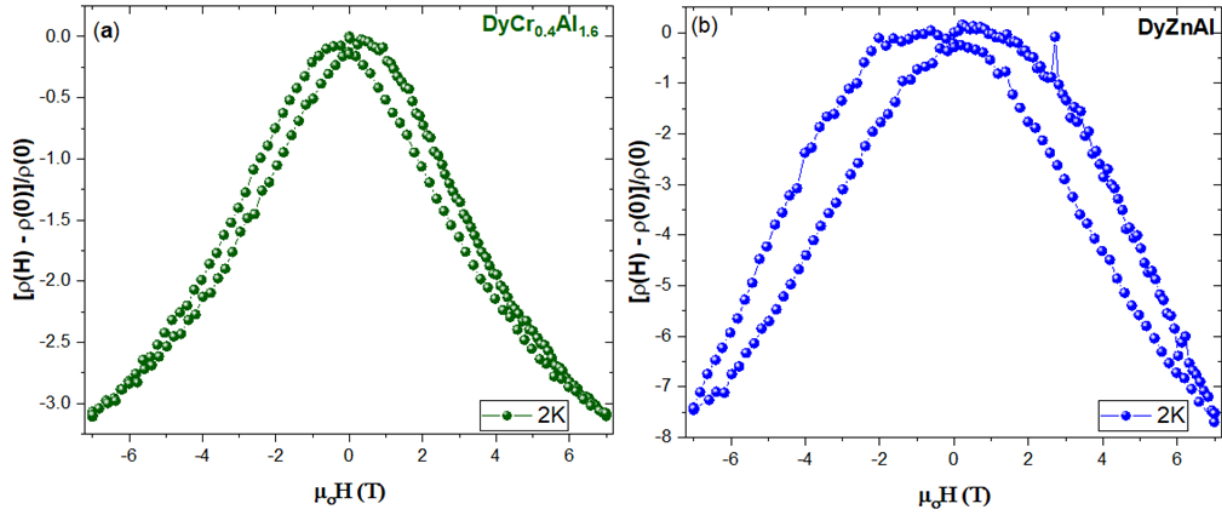


Figure 1.14. Magnetoresistance as a function of the applied magnetic field of (a) $\text{DyCr}_{0.4}\text{Al}_{1.6}$ and (b) DyZnAl at 2 K.

under applied magnetic field and zero fields, respectively. A maximum negative MR of 3.2 and 7.5% at 7T was observed for $\text{DyCr}_{0.4}\text{Al}_{1.6}$ and DyZnAl , respectively. In both compounds, the MR decreases with increasing magnetic field. This is because as the magnetic field is increased, the nonaligned magnetic spins align their spin-moments along the direction of the external magnetic field, resulting in the reduction of the resistivity.

2.4 Conclusion

The magnetic behavior of the cubic and hexagonal intermetallic compounds $\text{RCr}_{0.4}\text{Al}_{1.6}$ and RZnAl are consistent with an indirect exchange interaction occurring through the polarization of the conduction electrons. The field cooled (FC) and zero-field cooled (ZFC) magnetization data in an applied field of 0.1 T indicate a ferromagnetic ordering of all the compounds with ferromagnetic-like transitions at T_c in the range of 20-190 K. MR measurements revealed different magnetoresistive behaviors at 2 K. A negative MR effect of 3.2 and 7.5% was observed for $\text{DyCr}_{0.4}\text{Al}_{1.6}$ and DyZnAl sample respectively. These compounds show normal magnetocaloric effects. The magnitude of entropy changes around the transition temperatures increases with an increase in the magnetic field for all the compounds. The entropy change values for the RZnAl

compounds remain relatively high throughout the entire temperature change. This makes them potential MCE materials for low-temperature applications.

2.5 References

1. S. Gupta, K.G. Suresh, *Journal of Alloys and Compounds* 618 (2015) 562–606.
2. F. Stein, M. Palm, G. Sauthoff, *Intermetallics* 12 (2004) 713–720.
3. J. H. Wernick, *Intermetallic Compounds*, Wiley VCH, New York, 1967.
4. C. M. Hamm, D. Golden, E. Hildebrandt, J. Weischenberg, H. Zhang, L. Alff and C. S. Birkel, *J. Mater. Chem. C*, 2016, 4, 7430.
5. M. S. Henriques, D. I. Gorbunov, J. C. Waerenborgh, L. Havela, A. B. Shick, M. Divis, A. V. Andreev and A. P. Goncalves, *J. Phys. Condens. Matter* 25 (2013) 066010.
6. A. Verniere, P. Lejay, P. Bordet, J. Chenavas, J.P. Brison, P. Haen and J.X. Boucherle, *Journal of Alloys and Compounds*, 209 (1994) 251-255.
7. S. Gupta, K.G. Suresh, *Journal of Alloys and Compounds* 618 (2015) 562–606.
8. S.K. Dhar, C. Mitra, P. Manfrinetti, R. Palenzona, A. Palenzona, *J. Phase Equilibria* 23 (2002) 79.
9. D.T. Adroja, B.D. Rainford, S.K. Malik, H. Takeya, K.A. Gschneidner Jr, V.K. Pecharsky, *J. Alloys Comp.* 288 (1999) 7.
10. K. Kamioka, A. Oyamada, K. Hashi, S. Maegawa, T. Goto, H. Kitazawa, Y. Isikawa, *Phys. B* 259 (1999) 121.
11. K. Nakamura, Y. Kitaoka, K. Asayama, T. Takabatake, G. Nakamoto, H. Tanaka, H. Fujii, *Phys. B* 206 (1995) 829.
12. M. Napoletano, F. Canepa, P. Manfrinetti, F. Merlo, *J. Mater. Chem.* 10 (2000) 1663.
13. N.K. Singh, K.G. Suresh, R. Nirmala, A.K. Nigam, S.K. Malik, *J. Appl. Phys.* 101 (2007) 093904.
14. Y. Pan, A.M. Nikitin, T.V. Bay, Y.K. Huang, C. Paulsen, B.H. Yan, A. de Visser, *Europhys. Lett.* 104 (2013) 27001.
15. R. D. James and D. Kinderlehrer, *Theory of magnetostriction with applications to $Tb_xDy_{1-x}Fe_2$* , 1993.
16. R. Grossinger, R. S. Turtelli and N. Mehmood, *IOP Conf. Ser. Mater. Sci. Eng.*, 2014, 60, 012002.

17. T. Gao, N. Qi, Y. Zhang and T. Zhou, *J. Phys. Conf. Ser.*, 2014, 568, 042006.
18. J. B. Milstein, *Solid State Chemistry: A Contemporary Overview*, 1980, pp. 291–307.
19. T. Hashimoto, K. Matsumoto, T. Kurihara, T. Numuzawa, A. H. Tomokiyo, T. G. Yayama, S. Todo and M. Sahashi, *Adv. Cryogen. Eng.* 32 1986 279
20. Kunming Gu, Junqin Li, Weiqin Ao, Yongxi Jian, Jiaoning Tang, *Journal of Alloys and Compounds* 441 (2007) 39–42.
21. N.K. Singh, K.G. Suresh, R. Nirmla, A.K. Nigam, S.K. Malik, *J. Appl. Phys.* 99 (2006) 08K904.
22. L. Menon, S.K. Malik, *Phys. Rev. B* 51 (1995) 5858.
23. N.K. Singh, K.G. Suresh, R. Nirmala, A.K. Nigam, S.K. Malik, *J. Magn. Magn. Mater.* 302 (2006) 302.
24. N.K. Singh, K.G. Suresh, R. Nirmala, A.K. Nigam, S.K. Malik, *J. Appl. Phys.* 101 (2007) 093904.
25. Q.Y. Dong, B.G. Shen, J. Chen, J. Shen, J.R. Sun, *J. Appl. Phys.* 105 (2009) 113902.
26. E. Talik, J. Kusz, W. Hofmeister, M. Matlak, M. Skutecka, M. Klimczak, *J. Alloys Compd.* 423 (2006) 47.
27. S. Gupta, K.G. Suresh, *Journal of Alloys and Compounds* 618 (2015) 562–606.
28. H. Oesterreicher, *J. Less-Common Met.* 25 (1971) 341.
29. Q.Y. Dong, B.G. Shen, J. Chen, J. Shen, H.W. Zhang, J.R. Sun, *J. Appl. Phys.* 105 (2009) 07A305
30. H. Oesterreicher, *J. Less-Common Met.* 25 (1971) 228.
31. A. E. Dwight. M. H. Muller. R. A. Conner, Jr., J. W. Downey and H. Knott, *Trans. AIME* 242 (1968) 2075.
32. M. Oboz, E. Talik, *Journal of Alloys and Compounds* 509 (2011) 5441–5446
33. H. Oesterreicher, *Phys. Stat. Sol. (a)* 40 (1977) K139.
34. L. Li, D. Huo, Z. Qian, K. Nishimura, *Intermetallics* 46 (2014) 231.
35. X.X. Zhang, F.W. Wang, G.H. Wen, *J. Phys.: Condens. Matter* 13 (2001) L747.
36. H. Oesterreicher, *J. Less-Common Met.* 30 (1973) 225

37. P. Javorsky', L. Havela, V. Sechovsky', H. Michor, K. Jurek, J. Alloys Comp. 264 (1998) 38.
38. J. Jarosz, E. Talik, T. Mydlarz, J. Kusz, H. BoKhm, A. Winiarski, Journal of Magnetism and Magnetic Materials 208 (2000) 169-180
39. B. Chevalier, W. Hermes, B. Heying, U. C. Rodewald, A. Hammerschmidt, S. F. Matar, E. Gaudin, R. Pöttgen, Chem. Mater. 2010, 22, 5013–5021.
40. M. J. Evans, G. P. Holland, F. J. Garcia-Garcia, U. Häussermann, J. Am. Chem. Soc. 2008, 130, 12139–12147.
41. Q.Y. Dong, B.G. Shen, J. Chen, J. Shen, J.R. Sun, Solid State Commun. 151 (2011) 112
42. Q. Dong, B. Shen, S. He, H. Jiang, W. Zheng, J. Sun, J. Nanosci. Nanotech. 12 (2012) 1040.
43. L.C. Wang, Q.Y. Dong, Z.J. Mo, Z.Y. Xu, F.X. Hu, J.R. Sun, B.G. Shen, J. Appl. Phys. 114 (2013) 163915

CHAPTER 3. ENGINEERING MAGNETIC TRANSITIONS IN TERNARY LAVES TYPE PHASES, $\text{GdCr}_x\text{Al}_{2-x}$ AND GdZnAl .

We have demonstrated in chapter 2 that perturbing the valence electron concentration at the Fermi level leads to drastically different structural, magnetocaloric and magnetic properties of RTAl ($\text{R} = \text{Tb, Dy, Ho}$; $\text{T} = \text{Zn, Cu, Ni, Co, Fe, Mn, Cr}$). Realizing that the changes in the valence electron concentration dictate the observed changes in the structural, magnetocaloric and magnetic behavior, we have completely replaced Gd for R in the structure of RTAl ($\text{T} = \text{Cr, Zn}$; $\text{R} = \text{Tb, Dy, Ho}$) with the goal to substantially perturb the position of the VEC at the rare-earth site. In this chapter, we report the structural, magnetocaloric, magnetic, transport and magnetic properties of $\text{GdCr}_x\text{Al}_{2-x}$ ($x = 0.2, 0.3, 0.4, 0.45$) and GdZnAl .

3.1 Introduction

Ternary rare-earth transition-metal Laves phases, with the topologically close-packed (TCP) structure, are a rich family of intermetallics with the general formula RTX ($\text{R} = \text{Rare earth elements}$, $\text{T} = \text{transition metals}$, $\text{X} = \text{non-metals}$).¹ They have been studied extensively and their investigations have led to the discovery of novel materials with interesting physical properties including, magnetic polaronic behavior, intermediate valency, Kondo effect, multiple magnetic transitions, large Magnetocaloric effect (MCE), heavy fermion behavior, large Magnetoresistance (MR), spin glass state, superconductivity, metamagnetism, spin-orbital compensation, and pseudogap effect.²⁻⁸ Some of them have also been known to possess hydrogen storage capabilities. Notably, CaNiGe , GdScGe , GdTiGe , and NdScSi studied by Liu et al, Mahon et al, Gaudin et al, and Tence et al respectively have been considered as promising hydrogen storage materials for technological applications.⁹⁻¹² Because of their high melting point, high strength and low density, some of them are also used in high-temperature structural applications¹³

These classes of compounds adopt one of the three crystallographically closely related primary structure types: hexagonal MgNi_2 (C36), cubic MgCu_2 (C15), and hexagonal MgZn_2 (C14) or their ordered variant.¹⁴ In these three structures, the C15 phase exhibits better deformability than C14 and C36 phases at low temperatures due to more allowed independent slip systems.¹⁵

The structures in the RTX ternary Laves phases depends very strongly on the ionic radius of the X element. For example, Increasing the atomic size of X from Al to In in RMnX leads to a change from the MgCu_2 to MgNi_2 and to MgZn_2 -type structure.¹⁶⁻¹⁹ In addition, the crystallographic structures with fixed X element in the RTAl aluminides are also observed to depend on the atomic size of the rare earth elements. For instance, increasing the atomic size of R in RFeAl from R = Lu-Gd and to R = Sm-Ce results in a change from MgCu_2 structure to the MgZn_2 structure respectively.²⁰⁻²¹ On the other hand, keeping both R and Al elements fixed the change in structure has also been observed to depend on the influence of the VEC on the T elements. For instance, one could observe the change of the MgNi_2 -type structure (GdNiAl and GdCuAl) to MgZn_2 structure (GdCoAl and GdFeAl) and to MgCu_2 (GdMnAl) with decreasing valence electron concentration on the T element.^{16-18, 20, 22-23}

It is evident in great part that the valence electron concentration determines not only the crystallographic structure but also the magnetic properties of these compounds. It has been observed in the GdTAl (T = Cu, Ni, Co, Fe, Mn) family that the transition temperature, T_c increases with decreasing valence electron concentration on the T element. For example, the T_c (66 K) of GdNiAl increased from 100 K, 265 to 274 when the Ni atom is replaced with the Co, Fe, and the Mn atoms, respectively.^{17, 24-26}

In order to further extend the investigation of the correlation between the valence electron concentration and the magnetic properties as well as the crystallographic structures, we decided to look into Cr and Zn metals by keeping Gd and Al constant since this will alter the number of valence electrons due to different number of d electrons provided by different metals.

Herein we report on the synthesis, crystal structures, transport properties, magnetic properties, and electronic band structures of the GdTAl (T = Cr, Zn) series of compounds. From the powder X-ray diffraction structure refinements, these phases were confirmed to adopt the MgCu_2 and MgZn_2 -type structure for the GdCrAl and GdZnAl respectively. Magnetic susceptibility measurements revealed ferromagnetic and ferrimagnetic behavior for these analogs. Electrical resistivity measurement and electronic band structure calculations suggest that Gd-Cr-Al and GdZnAl exhibits a metallic behavior.

3.2 Experimental details

3.2.1 Synthesis

General Details. The following reagents were used as received: Finely dispersed powder of gadolinium (Alfa Aesar, 99.9%), aluminum powder (Alfa Aesar, 99.9%), chromium powder (Alfa Aesar, 99.9%) and zinc powder (Alfa Aesar, 99.9%). All manipulations during sample preparation were carried out in an argon-filled glovebox (content of O₂ < 0.5 ppm).

Synthesis of GdCr_xAl_{2-x}. All the chromium compounds were prepared by argon arc melting on a water-cooled copper crucible from elemental ingots with a purity of 99.99%. The Gd-Cr-Al compounds were prepared by arc-melting of stoichiometric amounts of Gd, Cr, and Al with some excess aluminum for compensation of the weight loss. Each compound was re-melted several times to ensure sample homogeneity.

Synthesis of GdZnAl. The GdZnAl compound was prepared by pressing elements into pellets without arc-melting. The samples were placed in carbon-coated quartz tubes, sealed and annealed at 1273 K for 7 days in an argon atmosphere, and subsequently quenched in air.

3.2.2 Physical property Measurements

Magnetic and resistivity measurements of Gd-Cr-Al and GdZnAl, were carried out on a Quantum Design Magnetic Property Measurement System using the Quantum Design superconducting quantum interference device (SQUID) magnetometer option and the Physical Property Measurement System, respectively (PPMS). Both field cooled (FC) and zero-field cooled (ZFC) measurements have been performed in the 2-400 K temperature range with an applied field up to 0.01 T. Field-dependent magnetization measurements were performed at 2 K and above room temperature. The temperature-dependent electrical resistivity measurements were carried out using the standard four-probe DC technique. V curves were recorded at 2 K with an applied field up to 7 T.

3.2.3 Structure Determination

Powder X-ray diffraction (PXRD) measurements were performed on the powdered samples of Gd-Cr-Al and GdZnAl using a PANalytical Empyrean X-ray Powder Diffractometer

operating at 45 kV/40 mA with (Cu K α 1, $\lambda = 1.540598$) radiation. The lattice parameters and crystal structure of the samples were analyzed by Rietveld refinement using the FULLPROF software.

3.2.4 Computational details

The chemical and electrical properties of GdAl_{1.5}Cr_{0.5} were computed using Quantum ESPRESSO²⁹ with the Perdew-Burke-Ernzerhof (PBE) generalized gradient approximations (GGA)³⁰ and the projector augmented wave (PAW) method. The cut-off energy of the wavefunction (charge density) was set to 120 (1,200) Ry and a cold smearing of 0.001 Ry was applied. For the pseudopotential of Gd, the f-electrons were not included in the valence states. While f-electrons can contribute to bonding and the physical properties, the degree of correlation and self-interaction error of f-electrons are challenging to treat with DFT methods accurately.³¹ Thus, the inclusion of f-electrons can introduce a significant error. In addition to f-electrons, d-electrons of Cr can exhibit strong electron correlations. To include these correlations, the Hubbard-U potential for Cr was set to 3.7 eV. Although the crystal structure of GdAl_{1.5}Cr_{0.5} is not layered, dispersion corrections were included to improve the prediction of the chemical and physical properties. For the dispersion corrections, the exchange-hole dipole moment (XDM) method by Becke and Johnson was implemented.³² All DFT calculations were performed on the primitive unit cell which contains six atoms. Because the Al-site was doped with Cr, it is important to determine the lowest ground state energy for the doped site. In this sense, four different configurations were calculated in which Cr is placed on the different Al sites. The difference between all configurations is relatively small (<0.02 Ry) leading to a ground state energy of -0.40 Ry atom⁻¹. Prior to the electronic band structure calculations, the crystal structure was completely relaxed using a Γ -centered 8x8x8 k-point mesh and force (energy) thresh-old of 10⁻⁵ Ry Bohr⁻¹ (10⁻⁸ Ry). The electronic band structure was calculated using a fine-meshed k-point path along the symmetry points and the density of states (DOS) with a Γ -centered 15x15x15 k-point mesh. It is important to note that the number of bands was increased to 60 to include a larger number of conduction bands. The charge density and electron localization function (ELF) were visualized with XCrysden.³³

3.3 Results and Discussion

3.3.1 Structural Characterization

The phases ($\text{GdCr}_{0.2}\text{Al}_{1.8}$, $\text{GdCr}_{0.3}\text{Al}_{1.7}$, $\text{GdCr}_{0.4}\text{Al}_{1.6}$, $\text{GdCr}_{0.45}\text{Al}_{1.55}$) and GdZnAl that adopt the MgCu_2 ($Fd\bar{3}m$) and MgZn_2 ($P6_3/mmc$) structure respectively, constitute an interesting series of ternary (RTAl) Laves phases in which correlations between valence electron concentration (VEC), stoichiometry, and structural properties can be studied. The PXRD data of the compounds were refined using the hexagonal MgZn_2 -type and the cubic MgCu_2 -type structural model respectively. Figure 3.1 shows the Rietveld refinements for PXRD data of ($\text{GdCr}_{0.2}\text{Al}_{1.8}$, $\text{GdCr}_{0.3}\text{Al}_{1.7}$, $\text{GdCr}_{0.4}\text{Al}_{1.6}$, $\text{GdCr}_{0.45}\text{Al}_{1.55}$) and GdZnAl . All the compounds contain Gd_2O_3 as a secondary phase as shown in Figure 3.1a-b. The GdZnAl however, contains additional impurities as seen in figure 3.1b.

The Rietveld refinement of all the compounds showed that the major phases contain about 90-98 wt% of the MgZn_2 -type (GdZnAl) and MgCu_2 -type ($\text{GdCr}_{0.2}\text{Al}_{1.8}$, $\text{GdCr}_{0.3}\text{Al}_{1.7}$, $\text{GdCr}_{0.4}\text{Al}_{1.5}$, and $\text{GdCr}_{0.45}\text{Al}_{1.5}$) with the remaining wt% distributed among the impurities. The refined lattice parameters of GdZnAl and $\text{GdCr}_x\text{Al}_{2-x}$ from Rietveld refinements are listed in Table 3.1. As shown in Table 1, the unit cell volume and lattice parameters of Gd-Cr-Al increases with increasing Cr concentration. The variation of the lattice parameters corresponds roughly to Vegard's rule, which states that solid solution lattice parameters vary linearly with composition. This behavior is usually observed in quasi-binary Laves phase systems, despite the occurring structural transitions.²⁷

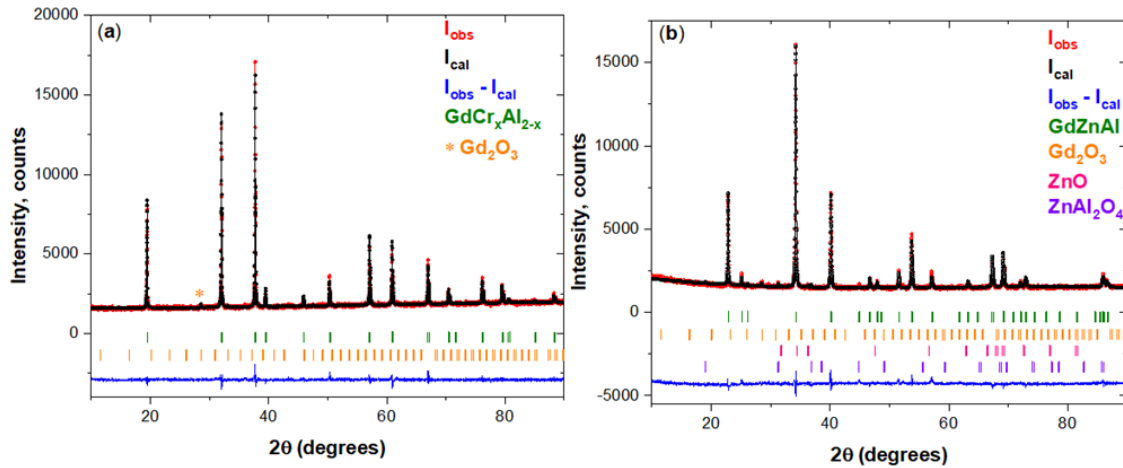


Figure 1.15. Rietveld refinement of the powder X-ray diffraction patterns of (a) $\text{GdCr}_x\text{Al}_{2-x}$, and (b) GdZnAl .

Table 3.4. Lattice parameters from Rietveld refinements of the Powder X-ray diffraction data of $\text{GdCr}_{0.2}\text{Al}_{1.8}$, $\text{GdCr}_{0.3}\text{Al}_{1.7}$, $\text{GdCr}_{0.4}\text{Al}_{1.6}$, $\text{GdCr}_{0.45}\text{Al}_{1.55}$, and GdZnAl

Compound	$a/\text{\AA}$	$c/\text{\AA}$	$V/\text{\AA}^3$
$\text{GdCr}_{0.2}\text{Al}_{1.8}$	7.8816		489.599
$\text{GdCr}_{0.3}\text{Al}_{1.7}$	7.8864		490.494
$\text{GdCr}_{0.4}\text{Al}_{1.6}$	7.8919		491.519
$\text{GdCr}_{0.45}\text{Al}_{1.55}$	7.8991		492.870
GdZnAl	4.4884	7.08438	123.433

3.3.2 Magnetic Properties

3.3.2.1 $\text{GdCr}_{0.2}\text{Al}_{1.8}$, $\text{GdCr}_{0.3}\text{Al}_{1.7}$, $\text{GdCr}_{0.4}\text{Al}_{1.6}$ and $\text{GdCr}_{0.45}\text{Al}_{1.55}$

Figure 3.2a-d shows the zero-field cooled (ZFC)-FC (field cooled) curves and inverse magnetic susceptibility as a function of the temperature of the $\text{GdCr}_{0.2}\text{Al}_{1.8}$, $\text{GdCr}_{0.3}\text{Al}_{1.7}$, $\text{GdCr}_{0.4}\text{Al}_{1.6}$, and $\text{GdCr}_{0.45}\text{Al}_{1.55}$ compounds under an external field of 0.1 T. The ZFC-FC curve for all the compounds obtained demonstrate a ferromagnetic behavior with a transition temperature T_C of 110 K, 140 K, 268 K and 271 K for $\text{GdCr}_{0.2}\text{Al}_{1.8}$, $\text{GdCr}_{0.3}\text{Al}_{1.7}$, $\text{GdCr}_{0.4}\text{Al}_{1.6}$, $\text{GdCr}_{0.45}\text{Al}_{1.55}$ respectively. It is obvious from the T_C values of the compounds that the T_C depends on the Cr concentration. Increasing the concentration of Cr increases T_C . However, any attempt to synthesize beyond $x = 0.45$ of Cr was not successful as indicated by Cr impurities. Further increase in the Al content in order to increase the Cr content leads to a decrease in T_C as a result of the dilution of the magnetic spins.

It is interesting to note that $\text{GdCr}_{0.4}\text{Al}_{1.6}$ and $\text{GdCr}_{0.45}\text{Al}_{1.55}$ exhibit a distinct behavior different from $\text{GdCr}_{0.2}\text{Al}_{1.8}$ and $\text{GdCr}_{0.3}\text{Al}_{1.7}$. Their ZFC-FC curves show a slight divergence at low temperatures indicating slight anisotropy in them as shown in Figure 3.2c and d. The temperature dependence of the inverse magnetic susceptibility for $\text{GdCr}_{0.2}\text{Al}_{1.8}$, $\text{GdCr}_{0.3}\text{Al}_{1.7}$, $\text{GdCr}_{0.4}\text{Al}_{1.6}$, and $\text{GdCr}_{0.45}\text{Al}_{1.55}$ was obtained in the paramagnetic region according to the Curie–Weiss law (see insets in Fig. 3.2a-d). The fit to the linear paramagnetic region as shown in the inset yields a paramagnetic Weiss temperature of 102 K and 114 K and 44 K indicating a ferromagnetic dominant interaction in $\text{GdCr}_{0.2}\text{Al}_{1.8}$, $\text{GdCr}_{0.4}\text{Al}_{1.6}$, and $\text{GdCr}_{0.45}\text{Al}_{1.55}$ respectively. The fit, however, yielded -210 K in $\text{GdCr}_{0.3}\text{Al}_{1.7}$ suggesting an antiferromagnetic nearest-neighbor interaction indicating a ferrimagnetic behavior in the compound. The fit also yielded an effective

magnetic moment per formula unit (M_{eff}/fu) increases with Cr content from $7.5 \mu_B$ for $\text{GdCr}_{0.2}\text{Al}_{1.8}$ to $8.15 \mu_B$ for $\text{GdCr}_{0.45}\text{Al}_{1.55}$. These values are close to the theoretical effective paramagnetic moment of trivalent Gd ($7.94 \mu_B$). The M_{eff}/fu values of $\text{GdCr}_{0.4}\text{Al}_{1.6}$ ($8.10 \mu_B$) and $\text{GdCr}_{0.45}\text{Al}_{1.55}$ ($8.15 \mu_B$) yield effective magnetic moments of $2.53 \mu_B/\text{Cr}$ and $2.67 \mu_B/\text{Cr}$, respectively. These Cr effective magnetic moments are close to the magnetic moment of Cr^{3+} ($3.70 \mu_B$).

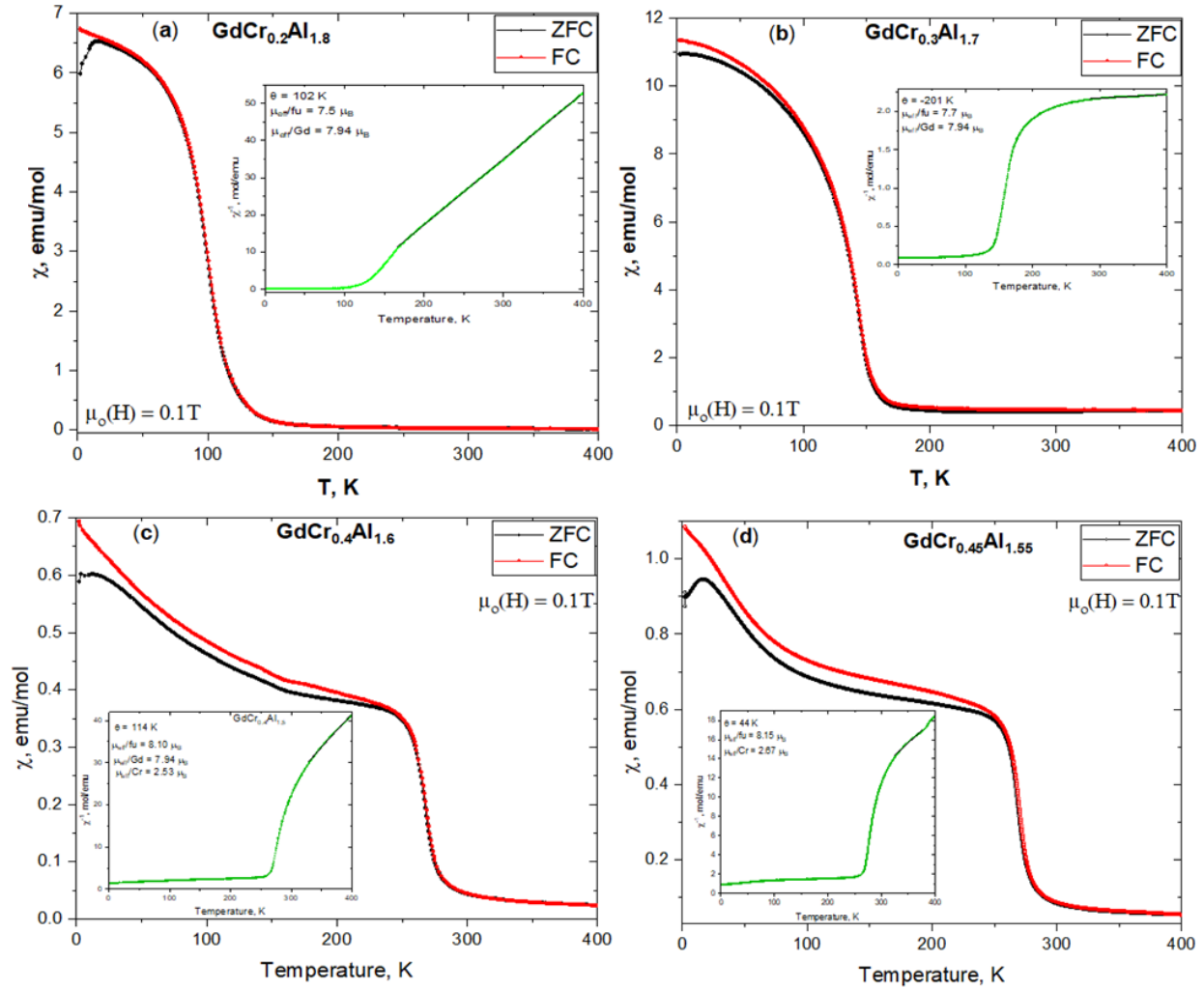


Figure 1.16. Magnetization vs temperature of (a) $\text{GdCr}_{0.2}\text{Al}_{1.8}$, (b) $\text{GdCr}_{0.3}\text{Al}_{1.7}$ and (c) $\text{GdCr}_{0.4}\text{Al}_{1.6}$ and (d) $\text{GdCr}_{0.45}\text{Al}_{1.5}$ compounds in applied field of 0.1 T.

The isothermal magnetization curves were recorded at 2 K for ($\text{GdCr}_{0.3}\text{Al}_{1.7}$, $\text{GdCr}_{0.4}\text{Al}_{1.6}$, $\text{GdCr}_{0.45}\text{Al}_{1.55}$) and 2, 75, 300 K for $\text{GdCr}_{0.2}\text{Al}_{1.8}$ as shown in figure 3.3a-d. All the samples at 2 K show a linear increase in magnetization with increasing applied field and negligible coercivity, with saturation magnetization value, obtained at 2 K, reaching values of 4.2 , 4.0 , 2.3 and $2.7 \mu_B/\text{fu}$

for $\text{GdCr}_{0.2}\text{Al}_{1.8}$, $\text{GdCr}_{0.3}\text{Al}_{1.7}$, $\text{GdCr}_{0.4}\text{Al}_{1.6}$, $\text{GdCr}_{0.45}\text{Al}_{1.55}$, respectively. The computed total magnetization of $\text{GdCr}_{0.5}\text{Al}_{1.5}$ is $2.3 \mu_{\text{B}}/\text{fu}$. This is slightly lower than the experimental value. It is important to note that f -electrons are neglected in the valence states. Although f -electrons can be significant for magnetization, DFT calculations cannot treat the degree of correlation in f -electrons accurately introducing a significant error in the calculations.

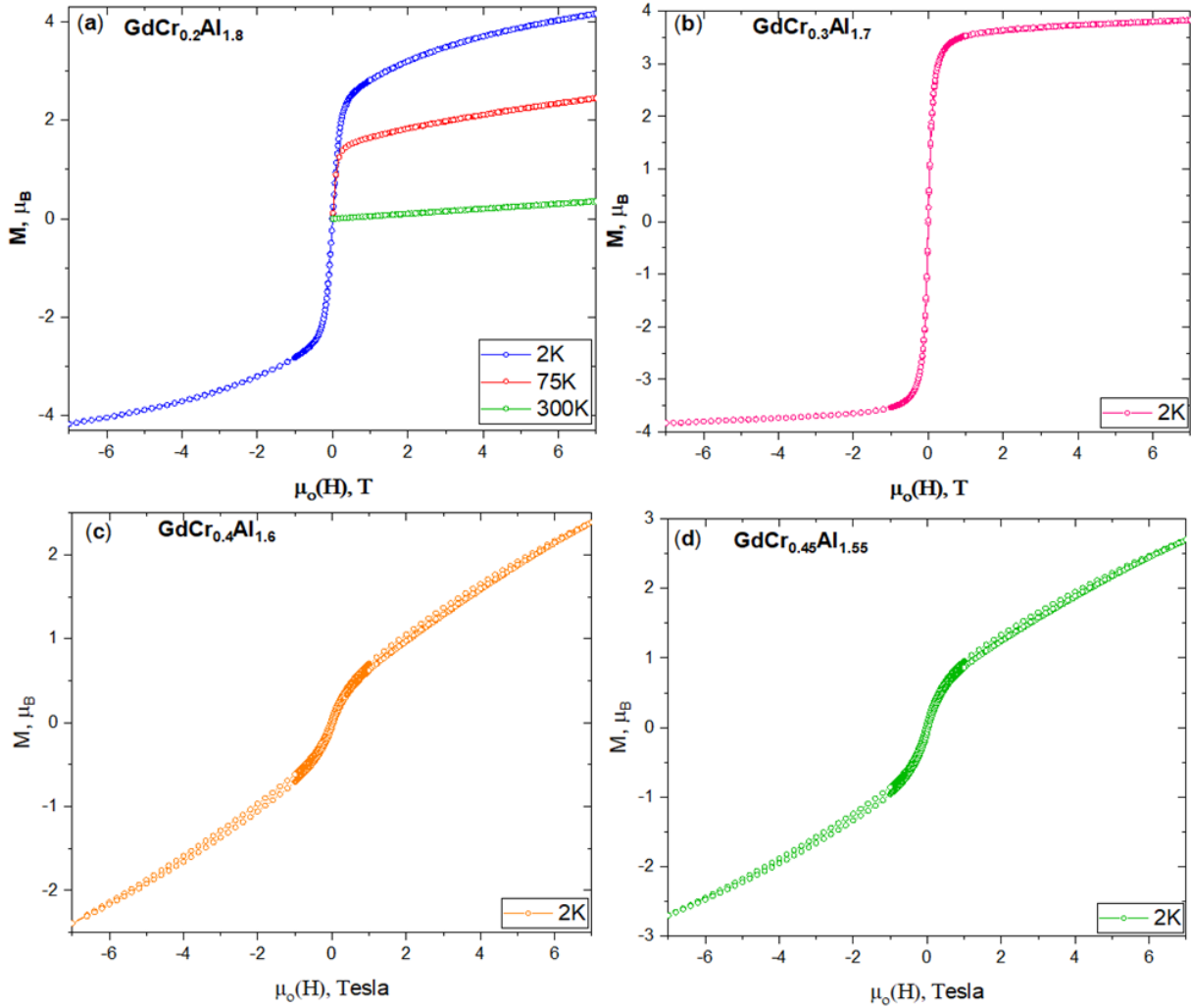


Figure 1.17. Magnetization as a function of the external magnetic field of (a) $\text{GdCr}_{0.2}\text{Al}_{1.8}$, (b) $\text{GdCr}_{0.3}\text{Al}_{1.7}$ and (c) $\text{GdCr}_{0.4}\text{Al}_{1.6}$ and (d) $\text{GdCr}_{0.45}\text{Al}_{1.55}$ compounds at 2 K in fields up to 7 T.

The saturation magnetization for $\text{GdCr}_{0.2}\text{Al}_{1.8}$ at 75 K and room temperature shows a decrease in the magnetization value and at room temperature, it shows the compound is in the paramagnetic state as displayed in Figure 3.3a. These magnetic saturation values are lower than the theoretical ordered moment of Gd ($7 \mu_{\text{B}}$). This reduction of the observed moment values in

GdCr_{0.2}Al_{1.8}, GdCr_{0.3}Al_{1.7}, GdCr_{0.4}Al_{1.6}, GdCr_{0.45}Al_{1.55} suggests a possible antiferromagnetic coupling between the 4f and the 3d magnetic sublattices. Interestingly, we did not see any AFM behavior in the inverse magnetic susceptibility plot except for GdCr_{0.3}Al_{1.7} which has a Curie Weiss temperature of -210 K (Figure 3.2b). Similar magnetic saturation behavior has been observed in other Gd-Cr-Al (GdCr_{3.5}Al_{8.5}, 4.25 μ_B /fu and GdCr₄Al₈, 4.33 μ_B /fu) compounds and other GdTAl (T = Mn, Fe, Co, Ni, Cu) systems.^{17, 24-28} Because these phases are metallic, this behavior probably stems from Ruderman–Kittel–Kasuya–Yosida (RKKY) interaction that is mediated by conduction electrons.

3.3.2.2 GdZnAl

Figure 3.4 shows the field and temperature dependence of magnetization for the GdZnAl compound measured at 0.1 T and 2 K, respectively. From the ZFC-FC curve, we can clearly observe ferromagnetic behavior with a Curie temperature of 131 K (Fig. 4). In addition, GdZnAl indicates an upturn in magnetization at 70 K (T_N). This upturn could be due to a small amount of impurity (Fig. 3.15b) present in the sample. The corresponding temperature dependence of the inverse susceptibility is shown in (Fig. 3.4a inset). The effective magnetic moment, M_{eff} calculated is equal to 8.04 μ_B /fu. This value is 0.26 μ_B larger than the theoretical effective paramagnetic moment of trivalent Gd (7.94 μ_B). However, many intermetallics of Gd and non-magnetic metals were found to have excess effective moments up to 0.8 μ_B . This effect is mostly assigned to the polarization of the Gd 5d conduction electrons. The *d-f* exchange constant is larger than the *s-f* one, due to the narrow nature of the 5d band. Figure 5 shows the isothermal magnetization of GdZnAl at 2 K. It is evidence that the compound exhibits a ferromagnetic behavior with a saturation value of 7.6 μ_B for 2 K. This magnitude of saturation magnetization is close to the corresponding free-ion saturation moment of Gd (7.0 μ_B).

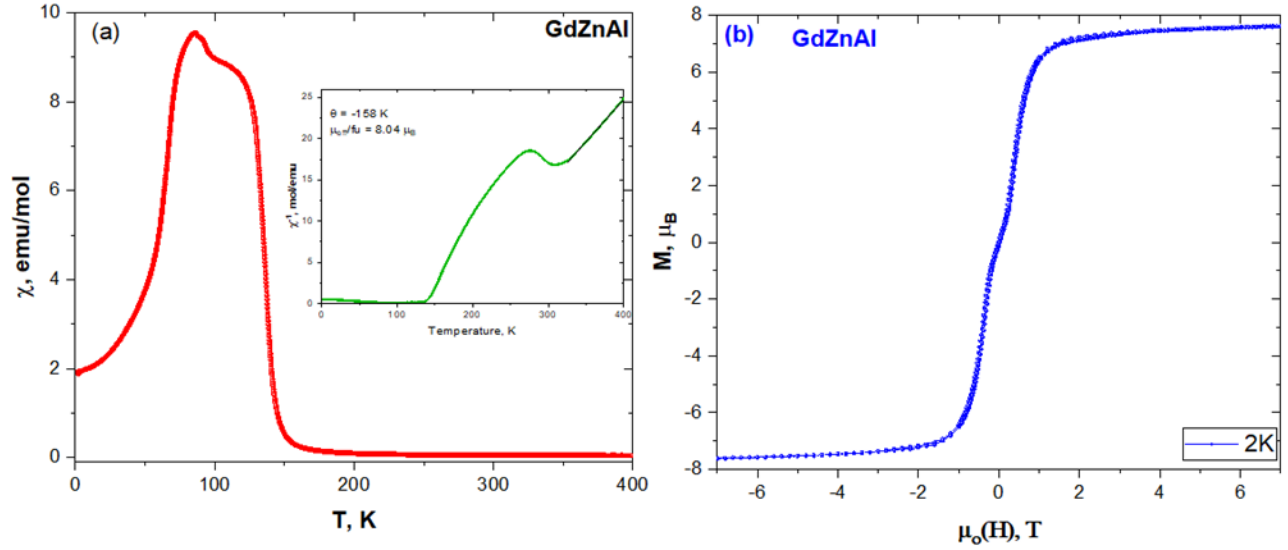


Figure 1.18. Magnetic properties of GdZnAl: (a) magnetic susceptibility at 0.01 T; (b) isothermal field-dependent magnetization at 2.0 K.

Comparatively, the T_C values for other GdTAl systems in the previous reports are 82 K for GdCuAl, 66 K for GdNiAl, 100 K for GdCoAl, 265 for GdFeAl and 274 K for GdMnAl (see Table 3.2). Although we have not stoichiometrically synthesized the equimolar Gd-Cr-Al compound the T_C of the GdCr_{0.45}Al_{1.55} is larger than all the other GdTAl systems, with the exception of GdMnAl. It is clear from Table 3.2 that the transition metal is controlling both the T_C and the structure. Figure 3.5 shows the variation of the valence electron concentration (VEC) of T on the T_C . It is obvious from the graph that decreasing VEC on T increases the T_C except for Ni. The role played by the d -electrons in these GdTAl systems is very important. A transfer of conduction electrons to fill the transition element d bands leads to the decrease of the conduction electron concentration. The increase of electrons in the $3d$ band leads to an increase in the density of states (DOS) at the Fermi level. The increase of the DOS leads to a decrease in the T_C .

3.3.3 Magnetocaloric effect of GdCr_xAl_{2-x}

The entropy of magnetic material changes when placed in a changing magnetic field that causes a change in the temperature of the material under adiabatic conditions, known as the magnetocaloric effect. In order to estimate the change in the magnetic entropy in the present compound, the magnetic field dependent magnetization at several temperatures was measured. The magnetic entropy change (ΔS_M) is calculated using the following equation:

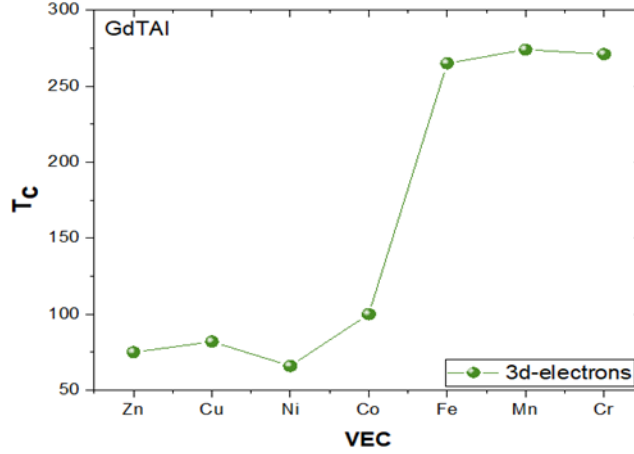


Figure 1.19. Variation of Curie temperature as a function of valence electron concentration of T on selected GdTAl (T = Zn, Cu, Ni, Co, Fe, Mn, Cr).

Table 3.5. The Curie temperature (T_C), and structure for GdZnAl and GdCr_{0.45}Al_{1.5} compared with other GdTAl systems.

Compounds	Structure	T_C /K	References
GdZnAl	$P6_3/mmc$	131	This work
GdCuAl	$P\bar{6}2m$	82	28
GdNiAl	$P\bar{6}2m$	66	24
GdCoAl	$P6_3/mmc$	100	25
GdFeAl	$P6_3/mmc$	268	26
GdMnAl	$Fd\bar{3}m$	274	17
GdCr _{0.45} Al _{1.55}	$Fd\bar{3}m$	271	This work

$$\Delta SM = - \int H (\partial M / \partial T) H dH \quad (1)$$

Fig. 3.6a-d shows the temperature dependence of the magnetic entropy change (ΔSM) for GdCr_{0.2}Al_{1.8}, GdCr_{0.3}Al_{1.7}, GdCr_{0.4}Al_{1.6} and GdCr_{0.45}Al_{1.55} for a field change of 0-5T. The highest entropy for these compounds occurs at the T_C for these compounds. GdCr_{0.2}Al_{1.8} and GdCr_{0.3}Al_{1.7} have a higher $-\Delta SM$ than GdCr_{0.4}Al_{1.6} and GdCr_{0.45}Al_{1.55} at all temperatures and an applied field of 0-5 T. Of these former two compounds, GdCr_{0.3}Al_{1.7} has the highest $-\Delta SM$ of 3.83 J kg⁻¹K⁻¹ at 141 K with GdCr_{0.2}Al_{1.8} having the $-\Delta SM$ of 3.38 J kg⁻¹K⁻¹ at 97 K, and of the latter two, GdCr_{0.4}Al_{1.6} and GdCr_{0.45}Al_{1.55} have a $-\Delta SM$ of 0.60 J kg⁻¹K⁻¹ (268 K) and 0.30 J kg⁻¹K⁻¹ (271 K), respectively.

These entropy values are greater than those of GdMnAl ($0.69 \text{ J kg}^{-1}\text{K}^{-1}$, 274 K) and GdFeAl ($2.78 \text{ J kg}^{-1}\text{K}^{-1}$, 265 K).¹⁷

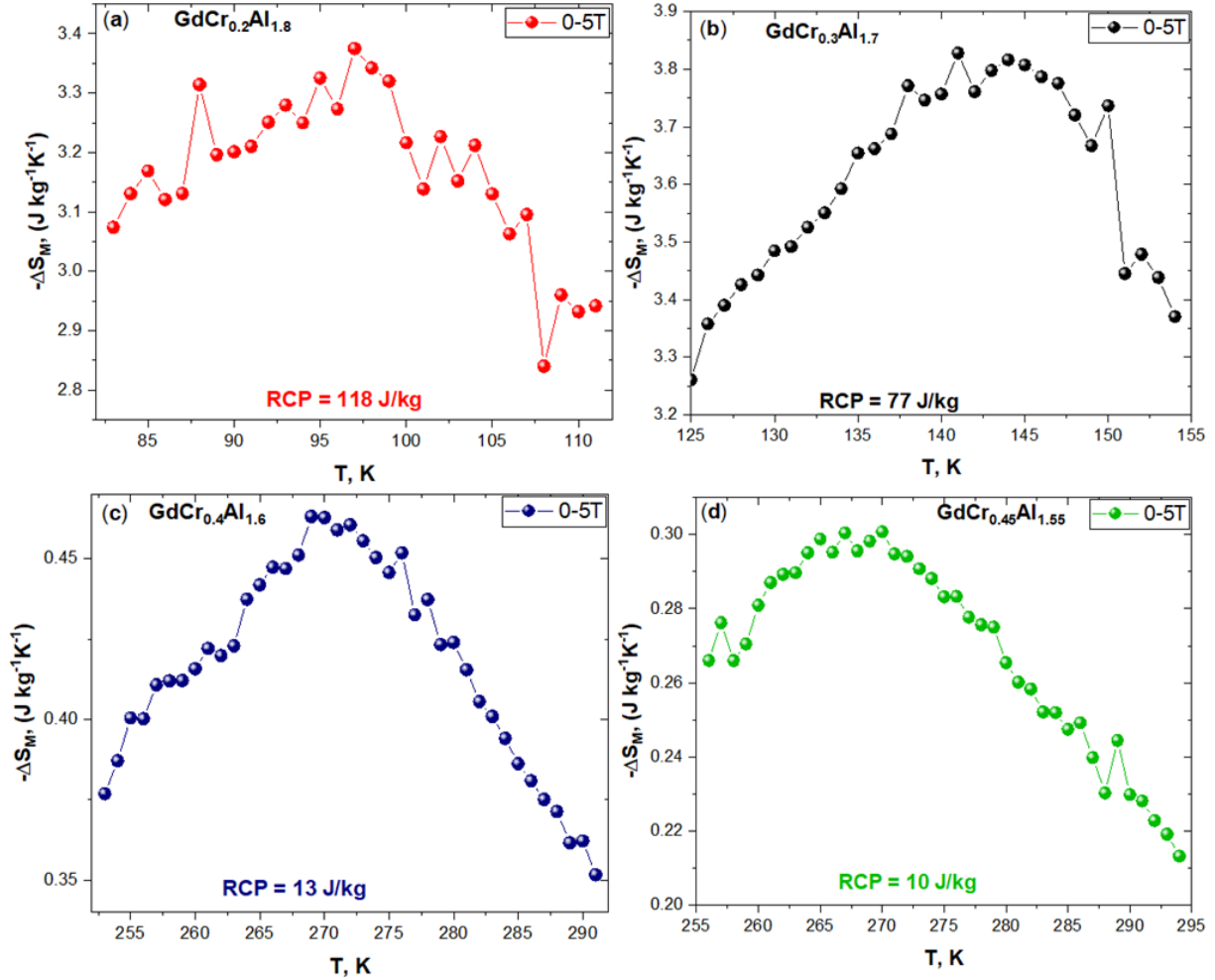


Figure 1.20 Temperature dependence of the isothermal magnetic entropy changes for (a) $\text{GdCr}_{0.2}\text{Al}_{1.8}$, (b) $\text{GdCr}_{0.3}\text{Al}_{1.7}$, (c) $\text{GdCr}_{0.4}\text{Al}_{1.6}$ and (d) $\text{GdCr}_{0.45}\text{Al}_{1.55}$ in the field change of 0-5 T.

The relative cooling power (RCP) is an important parameter of a magnetocaloric material. It is the amount of heat that can be transferred from the hot to the cold sinks and vice versa in one thermodynamic cycle of a magnetic refrigerator. The value of RCP is calculated using:

$$RCP = -\Delta S_M \times \delta T_{FWHM}, \quad (2)$$

where δT_{FWHM} is the full width at half maximum of the $-\Delta S_M(T)$ curve. The calculated RCP values obtained are 118 J kg^{-1} , 77 J kg^{-1} , 13 J kg^{-1} and 10 J kg^{-1} for $\text{GdCr}_{0.2}\text{Al}_{1.8}$, $\text{GdCr}_{0.3}\text{Al}_{1.7}$, $\text{GdCr}_{0.4}\text{Al}_{1.6}$,

and $\text{GdCr}_{0.45}\text{Al}_{1.55}$, respectively. The values obtained for $\text{GdCr}_{0.2}\text{Al}_{1.8}$ and $\text{GdC}_{0.3}\text{Al}_{1.7}$ are greater than GdMnAl (59 J kg^{-1}) and less than that of GdFeAl (570 J kg^{-1}).¹⁷

3.3.4 Magnetocaloric effect of GdZnAl

The magnetic entropy change (ΔSM) of the GdZnAl compound was calculated from magnetization isotherms recorded in the 118–157 K temperature range (Fig. 3.7a) using the integrated Maxwell relation stated above. The maximum entropy change is observed around 131 K, with the calculated values of $-\Delta S_M = 8.16$ and $20.50 \text{ J kg}^{-1}\text{K}^{-1}$ at $H_{\text{max}} = 0-2$ and $0-5 \text{ T}$ (Fig. 3.7b), respectively. Table 2 shows the magnetic entropy change for GdZnAl and $\text{GdCr}_{0.45}\text{Al}_{1.55}$ as well as other GdTAl (Mn, Fe, Co, Ni, Cu) variants. One can see a drastic decrease in the magnetic entropy value from GdZnAl ($20.5 \text{ J kg}^{-1}\text{K}^{-1}$) to $\text{GdCr}_{0.45}\text{Al}_{1.55}$ ($0.30 \text{ J kg}^{-1}\text{K}^{-1}$). This behavior can be related to the randomly aligned atoms due to an increase in the unit cell volume from GdZnAl (123.433 \AA^3) to $\text{GdCr}_{0.45}\text{Al}_{1.55}$ (490.365 \AA^3).

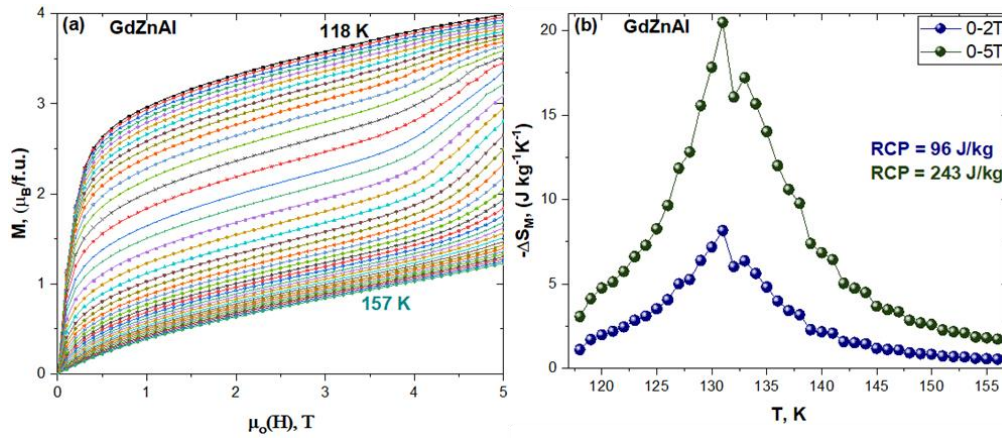


Figure 1.21. (a) Magnetization isotherms of GdZnAl at various temperatures (118 – 157 K); (b) Temperature dependence of the isothermal magnetic entropy changes for GdZnAl in the field change of 0-2 and 0-5 T.

The unit cell volume dependence of the magnetic entropy change for the $\text{GdCr}_{0.45}\text{Al}_{1.55}$, GdZnAl , and other GdTAl ($T = \text{Mn, Fe, Co, Ni, Cu}$) compounds are shown in Figure 3.8. This random alignment of the magnetic spins causes a loss of the magnetic entropy which is emanating from the energy used to realign the magnetic spins by the field. The RCP of the GdZnAl is also estimated to be 243 J kg^{-1} . The RCP values $\text{GdCr}_{0.45}\text{Al}_{1.55}$, GdZnAl , and other GdTAl ($T = \text{Mn, Fe, Co, Ni, Cu}$) compounds obtained listed in Table 3.3.

Table 3.6. The T_c , $-\Delta S_M$ max, and RCP for $\Delta H = 0-5$ T for GdZnAl and GdCr_{0.45}Al_{1.55} as well as other GdTAl (Mn, Fe, Co, Ni, Cu) variants.

Compounds	T_c	$-\Delta S_M(\text{J kg}^{-1} \text{K}^{-1})$	RCP(J kg^{-1})	References
GdZnAl	131	20.5	243	This work
GdCuAl	82	10.1	460	28
GdNiAl	66	10.9	460	24
GdCoAl	100	10.5	-	25
GdFeAl	268	3.70	420	26
GdMnAl	274	0.69	59	17
GdCr _{0.45} Al _{1.55}	271	0.30	10	This work

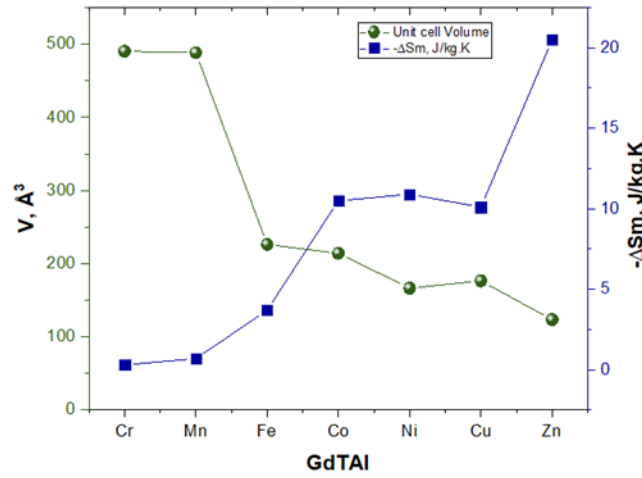


Figure 1.22. Unit cell volume dependence of the magnetic entropy change for the GdCr_{0.45}Al_{1.55}, GdZnAl, and other GdTAl (T = Mn, Fe, Co, Ni, Cu) compounds.

3.3.5 Magnetoresistance effect of Gd-Cr-Al and GdZnAl

In order to complement the magnetic properties of these compounds, the field and temperature dependence of electrical resistivity $\rho(T)$ of GdCr_{0.2}Al_{1.8}, GdCr_{0.4}Al_{1.6}, GdCr_{0.45}Al_{1.55}, and GdZnAl were measured. Figure 3.9a-d illustrates the temperature-dependent electrical resistivity $\rho(T)$ of GdCr_{0.2}Al_{1.8}, GdCr_{0.4}Al_{1.6}, GdCr_{0.45}Al_{1.55}, and GdZnAl at various applied magnetic field (0, 4, and 7 T). The resistivity of GdCr_{0.2}Al_{1.8}, GdCr_{0.4}Al_{1.6}, and GdCr_{0.45}Al_{1.55} (11a-c) at 0 T and 7 T displays an approximately linear decrease of the resistivity upon lowering the temperature, which is characteristic for metals. To verify the experimental results, the electronic band structure of GdAl_{1.5}Cr_{0.5} is displayed in Figure 3.11. The electronic bands are half-filled

indicating metallic behavior. Furthermore, the bands are strongly dispersed at the Fermi level suggesting that electron mobility and electrical conductivity are high. However, $\text{GdCr}_{0.45}\text{Al}_{1.55}$ (3.9c, 0, and 7 T) exhibits a sudden increase in resistivity around 271 K. This temperature coincides with the T_C of $\text{GdCr}_{0.4}\text{Al}_{1.55}$.

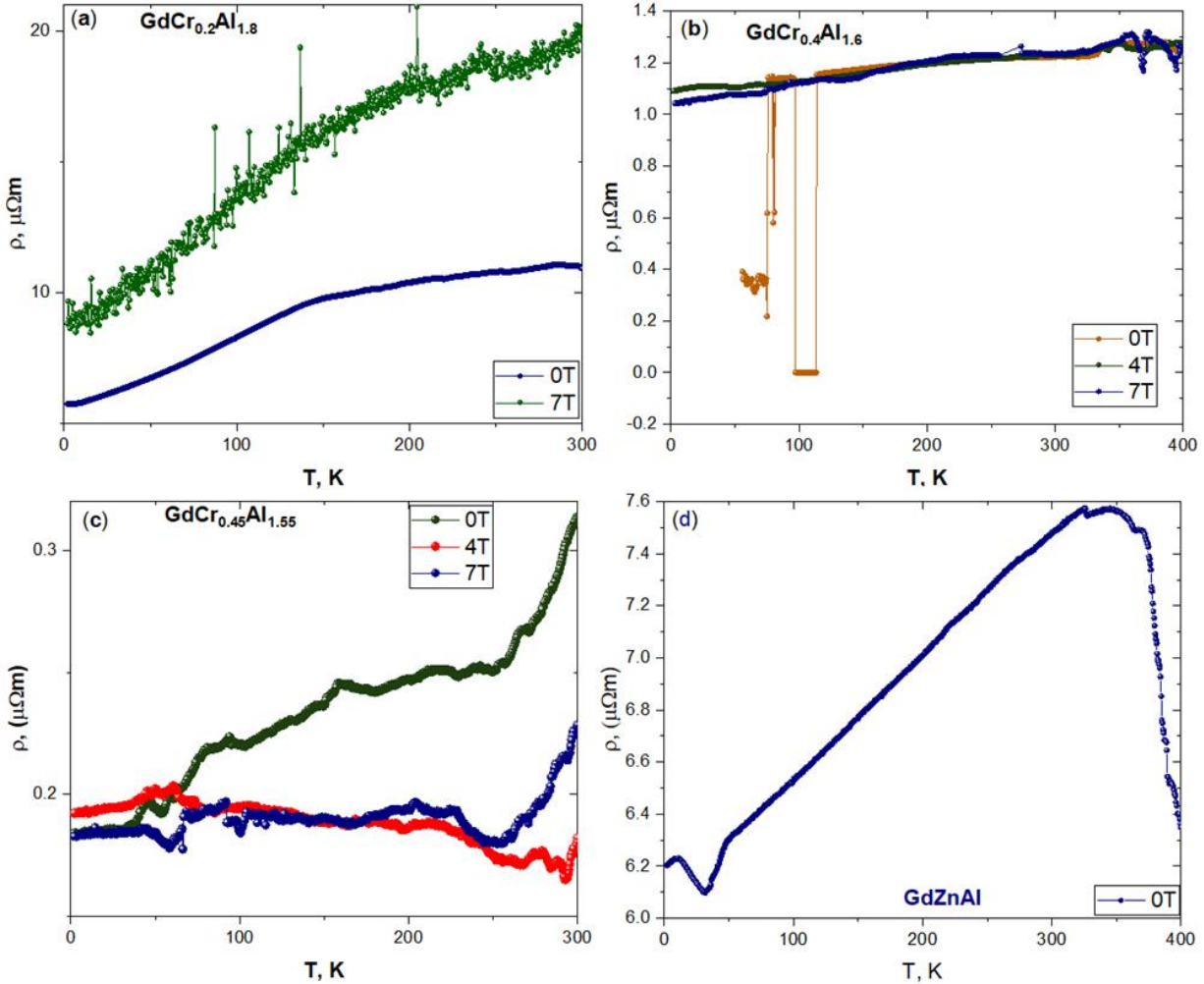


Figure 1.23. Resistivity as a function of temperature at various applied magnetic fields for (a) $\text{GdCr}_{0.2}\text{Al}_{1.8}$, (b) $\text{GdCr}_{0.4}\text{Al}_{1.6}$, (c) $\text{GdCr}_{0.45}\text{Al}_{1.55}$ and (d) GdZnAl .

The increase in the resistivity indicates an enhanced electron scattering in the vicinity of a magnetic phase transition. Interestingly, at 4T, the $\text{GdCr}_{0.45}\text{Al}_{1.55}$ exhibits a reverse trend from the one at 0 and 7 T. Its resistivity increases with decreasing temperature which is an indication of a semiconductor behavior. The trend at 4T for $\text{GdCr}_{0.4}\text{Al}_{1.6}$ (3.9b) however remains the same as in the case of 0 and 7T.

The GdZnAl analog (3.9d) at 0 T also exhibits a metallic character (between 48-300 K) like the Gd-Cr-Al variant before reaching a transition at 48 K where the resistivity decreases with decreasing temperature. This transition around 48 K is consistent with the AFM peak present in the magnetic susceptibility curve for GdZnAl (4a). A second transition at 300 K is marked by a decrease in resistivity with decreasing temperature. The source of this transition is however not known since it does not coincide with any transition in our susceptibility curve.

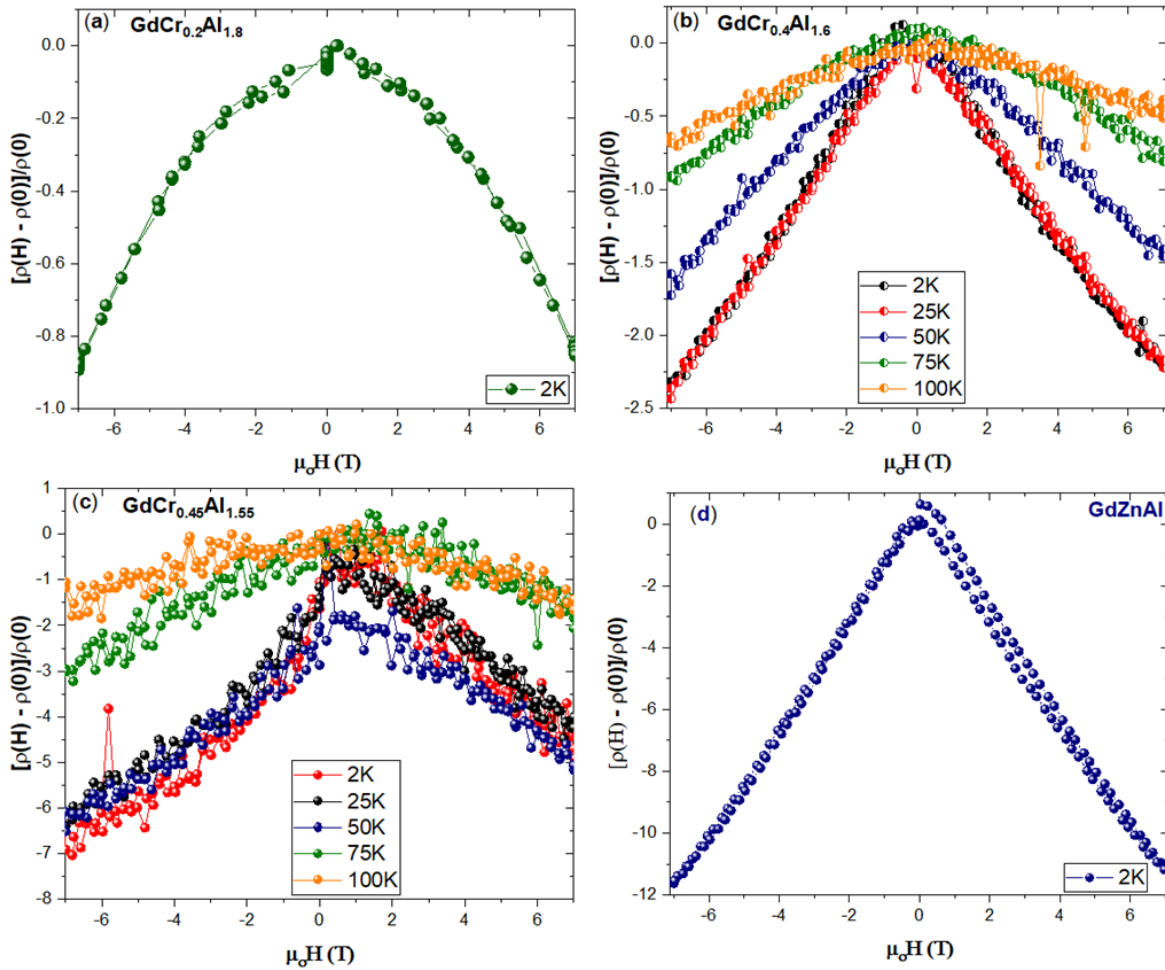


Figure 1.24. Magnetoresistance as a function of applied magnetic field at various temperatures for (a) GdCr_{0.2}Al, (b) GdCr_{0.4}Al_{1.5} and (c) GdCr_{0.45}Al_{1.5} and (d) GdZnAl.

Figure 3.10(a-d) displays the magnetoresistance $MR = [\rho(H) - \rho(0)]/\rho(0) \times 100\%$, as a function of magnetic field at different temperatures (GdCr_{0.4}Al_{1.6} and GdCr_{0.45}Al_{1.55}) and 2 K (GdCr_{0.2}Al_{1.8}, GdZnAl), where $\rho(H)$ is the resistance under an applied magnetic field and $\rho(0)$ under zero field. The MR patterns for all the compounds show a non-linear dependence on the

magnetic field and present systematic variation with temperature over a wide range of 2 K to 100 K and remains unsaturated throughout the entire field. The *MR* is all negative and their magnitude decreases with the increase of temperature. The largest negative *MR* of -0.9%, -2.5%, -7.0% and -11.8% for GdCr_{0.2}Al_{1.8}, GdCr_{0.4}Al_{1.6}, GdCr_{0.45}Al_{1.55}, and GdZnAl respectively is observed at 2 K for the change of 7 T magnetic field. On increasing the temperature for GdCr_{0.4}Al_{1.6} and GdCr_{0.45}Al_{1.55}, the *MR* decreases and is nearly independent of the magnetic field at 100 K.

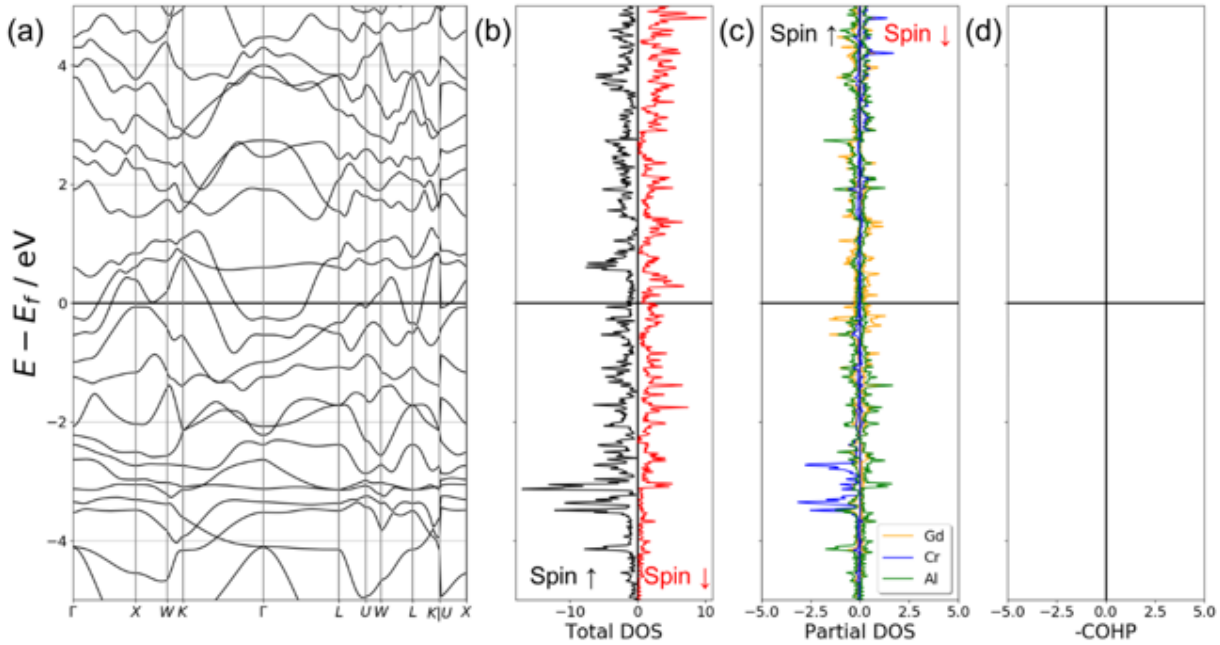


Figure 1.25. (a) The electronic band structure of GdCr_{0.5}Al_{1.5} indicates metallic behavior. (b) The (b) total and (c) partial DOS is split into their spins.

3.4 Conclusion

This study focused on, ternary Laves phases (Gd-Cr-Al and GdZnAl) and confirmed their cubic MgCu₂-type and hexagonal MgZn₂-type structures, respectively. Their physical properties with respect to susceptibility, magnetization, electrical resistivity were investigated. The Curie temperature, T_C of the Gd-Cr-Al compounds increased in increasing Cr concentration. Although we weren't successful in synthesizing the equimolar Gd-Cr-Al compound, the T_C of the GdCr_{0.45}Al_{1.55} ($T_C = 271$ K) is larger than all the other GdTAl systems except for GdMnAl ($T_C = 274$ K), which is 3 K greater. This increase in T_C is attributed to the decrease in the VEC at the transition metal magnetic centers. A combination of electronic structure calculations and transport measurements indicate the metallic character of the new compounds. Unlike the Cr analog, the Zn

analogs exhibit a giant magnetocaloric effect with an entropy value of $20.50 \text{ J kg}^{-1} \text{ K}^{-1}$ at $H_{\text{max}} = 0.5 \text{ T}$ with an RCP of 243 J kg^{-1} . This high entropy value of GdZnAl indicates its potential as a candidate material for low-temperature magnetic refrigeration.

3.5 References

1. F. Stein, *Intermetallics* 12 (2004) 713–720.
2. S.K. Dhar, C. Mitra, P. Manfrinetti, R. Palenzona, A. Palenzona, *J. Phase Equilibria* 23 (2002) 79.
3. D.T. Adroja, B.D. Rainford, S.K. Malik, H. Takeya, K.A. Gschneidner Jr, V.K. Pecharsky, *J. Alloys Comp.* 288 (1999) 7.
4. K. Kamioka, A. Oyamada, K. Hashi, S. Maegawa, T. Goto, H. Kitazawa, Y. Isikawa, *Phys. B* 259 (1999) 121.
5. K. Nakamura, Y. Kitaoka, K. Asayama, T. Takabatake, G. Nakamoto, H. Tanaka, H. Fujii, *Phys. B* 206 (1995) 829.
6. M. Napoletano, F. Canepa, P. Manfrinetti, F. Merlo, *J. Mater. Chem.* 10 (2000) 1663.
7. N.K. Singh, K.G. Suresh, R. Nirmala, A.K. Nigam, S.K. Malik, *J. Appl. Phys.* 101 (2007) 093904.
8. Y. Pan, A.M. Nikitin, T.V. Bay, Y.K. Huang, C. Paulsen, B.H. Yan, A. de Visser, *Europhys. Lett.* 104 (2013) 27001.
9. Xiaofeng Liu, Satoru Matsuishi, Satoru Fujitsu, Toru Ishigaki, Takashi Kamiyama, and Hideo Hosono, *J. Am. Chem. Soc.* 2012, 134, 11687–11694
10. Etienne Gaudin, Samir F. Matar, Rainer Pöttgen, Matthias Eul, and Bernard Chevalier, *Inorg. Chem.* 2011, 50, 11046–11054
11. Tadhg Mahon, Etienne Gaudin, Antoine Villesuzanne, Rodolphe Decourt, Jean-Louis Bobet, Olivier Isnard, Bernard Chevalier, and Sophie Tence,
12. Sophie Tencé, Tadhg Mahon, Etienne Gaudin, Bernard Chevalier, Jean-Louis Bobet, Roxana Flacau, Birgit Heying, Ute Ch. Rodewald, Rainer Pöttgen, *Journal of Solid-State Chemistry* 242 (2016) 168–174
13. F. Chu, D. J. Thoma, P. G. Kotula, S. Gerstl, T. E. Mitchell, I. M. Anderson and J. Bentley, *Acta mater.* Vol. 46, No. 5, pp. 1759-1769, 1998
14. F. Stein, M. Palm, G. Sauthoff, *Intermetallics* 12 (2004) 713–720.

15. A. Ormeci, F. Chu, J. M. Wills, T. E. Mitchell, R.C. Albers, D. J. Thoma, S. P. Chen, 1996 Phys. Rev. B 54 12753
16. P. Spatz, K. Gross, A. Züttel, F. Fauth, P. Fischer, L. Schlapbach, J. Alloys Comp. 261 (1997) 263.
17. M. Oboz, E. Talik, J. Alloys Comp. 509 (2011) 5441.
18. S. K. Dhar, C. Mitra, P. Manfrinetti, R. Palenzona, A. Palenzona, J. Phase Equilibria 23 (2002) 79.
19. M. Bacmann, D. Fruchart, J.L. Soubeyroux, J.H.V. J Brabers, F.R. de Boer, K.H.J. Buschow, J. Alloys Comp. 209 (1994) 135.
20. H. Oesterreicher, J. Less-Common Met. 25 (1971) 341.
21. Q.Y. Dong, B.G. Shen, J. Chen, J. Shen, H.W. Zhang, J.R. Sun, J. Appl. Phys. 105 (2009) 07A305 (and references therein).
22. H. Oesterreicher, J. Less-Common Met. 25 (1971) 228.
23. A.E. Dwight et al., Trans. Metall. Sot. AIME 242 (1968) 2075.
24. H. Oesterreicher, J. Less-Common Met. 30 (1973) 225
25. X.X. Zhang, F.W. Wang, G.H. Wen, J. Phys.: Condens. Matter 13 (2001) L747.
26. Q.Y. Dong, B.G. Shen, J. Chen, J. Shen, H.W. Zhang, J.R. Sun, J. Appl. Phys. 105 (2009) 07A305
27. A. Simon, Angew. Chem., Int. Ed. Engl. 1983, 22, 97.
28. P. Javorsky', L. Havela, V. Sechovsky', H. Michor, K. Jurek, J. Alloys Comp. 264 (1998) 38.
29. P. Giannozzi, S. Baroni, N. Bonini, M. Calandra, R. Car, C. Cavazzoni, D. Ceresoli, G. Chiarotti, M. Cococcioni, I. Dabo, et al. Quantum ESPRESSO: a modular and open-source software project for quantum simulations of materials J. Phys.: Condens. Matter, 21 (2009), p. 395502
30. J. P. Perdew, K. Burke, and M. Ernzerhof, Phys. Rev. Lett. **77**, 3865 (1996).
31. S. Kirklin, J. E. Saal, B. Meredig, A. Thompson, J. W. Doak, M. Aykol, S. Rühl, and C. Wolverton, npj Computational Materials (2015) 1, 15010.
32. A.D. Becke, E.R. Johnson Exchange-hole dipole moment and the dispersion interaction revisited J. Chem. Phys., 127 (2007), p. 154108

33. A. Kokalj, Computer graphics and graphical user interfaces as tools in simulations of matter at the atomic scale, *Comp. Mater. Sci.*, 2003, 28, 155-168

CHAPTER 4. MANIPULATION OF THE STRUCTURAL, MAGNETIC, AND MAGNETOCALORIC PROPERTIES IN $\text{GdNi}_{3-x-y}\text{Co}_x\text{Al}_y$ VIA VALENCE ELECTRON PERTURBATION.

We have demonstrated in chapter 3 that small perturbations of the density of states (DOS) at the Fermi level lead to slightly different magnetic behaviors of GdAl . Most especially, the decrease in the valence electron concentration at the Fermi level which leads to an increase in the curie temperature. Realizing that fewer d-electrons at the Fermi level leads to an increase in T_c , we decided to apply this hypothesis in other systems. We have, therefore, chosen GdNiAl_2 to explore. GdNiAl_2 is a known MCE material which exhibits an isothermal magnetic entropy change of $\Delta S_M = 16.0 \text{ Jkg}^{-1}\text{K}^{-1}$ at $T_C = 28\text{K}$ under a magnetic field change of 0-5 T. However, the low T_C limits its application as a room temperature magnetic refrigerant. We, therefore, substituted Co for (Ni/Al) in the structure of GdNiAl_2 , with the goal to perturb the position of the Fermi level of Ni since that will lead to a decrease in the VEC. In this chapter, we report the magnetic, structural, MCE, and transport properties of $\text{GdNi}_{3-x-y}\text{Co}_x\text{Al}_y$.

4.1 Introduction

The study of rare-earth (R) and transition-metal (T) based intermetallic compounds has drawn a lot of attention in recent decades because of potential multifunctional properties, such as giant magnetocaloric effects (MCEs).¹⁻² Magnetocaloric effect is a thermodynamic phenomenon of a magnetic material which relates the magnetic variables (magnetization, magnetic moment and magnetic field) of a magnetic material to its entropy and temperature.³⁻⁵ It is an intrinsic phenomenon of all magnetic materials and usually manifests as the temperature change in an adiabatic process (ΔT_{ad}) and the magnetic entropy change in an isothermal process (ΔS_M). The search for materials with promising MCE characteristics in the field of magnetic cooling is considered as the main pursuit in this field. In this regard, the MCE properties of certain rare-earth based intermetallics have been investigated experimentally and theoretically. Some of them have been discovered to have low-temperature MCE characteristics at higher applied fields.⁶⁻¹² However, practically applicable rare-earth based intermetallics with MCE characteristics that could provide sustainable operation in the applied magnetic field ($<2 \text{ T}$) are yet to be found.

The intermetallic rare-earth compounds RNiAl_2 have gained a lot of attention in recent years due to the second-order metamagnetic transition in them, which lead to large MCE.¹³⁻¹⁴ GdNiAl_2 exhibits an isothermal magnetic entropy change of $\Delta S = 16.0 \text{ J/kg.K}$ at $T_C = 28\text{K}$ under a magnetic field change from 0 to 5T.¹⁴ Zhang et al. have recently investigated the MCE in HoNiAl_2 and ErNiAl_2 compounds, and a large MCE of $14.0 \text{ Jkg}^{-1}\text{K}^{-1}$ and $21.2 \text{ Jkg}^{-1}\text{K}^{-1}$ was observed around the transition temperature of 7.5 K and 5.0 K for HoNiAl_2 and ErNiAl_2 respectively.¹³ However, the low T_C for the RNiAl_2 compounds limits their application as a room temperature magnetic refrigerant as the MCE exhibits its maximum value around the vicinity of the T_C .

It is known that the substitution of p-electron element X and the 3d sublattice of a transition metal element by another transition metal element has a very strong influence on the value of the T_C . Bajorek et al studied the partial substitution of Ni atoms in $\text{Gd}(\text{Ni}_{1-x}\text{T}_x)_3$ by other 3d (Fe, Co) elements. The substitution leads to some changes (increasing ordering temperature, decrease saturation magnetization, and MCE) in magnetic properties, which are correlated with their electronic structure. Most importantly, the Ni/T re-placement causes the increase in T_C as well as a decrease in the magnetic saturation value.¹⁵⁻¹⁶

In this paper, we are focused on the influence of cobalt substitution on the structure, MCE, and, magnetic properties of the GdNiAl_2 compound. Their structure, MCE, and magnetic properties will be compared to the newly synthesized GdCo_2Al and GdCoAl_2 .

4.2 Experimental details

4.2.1 Synthesis

General Details. The following reagents were used as received: Finely dispersed powder of gadolinium (Alfa Aesar, 99.9%), aluminum powder (Alfa Aesar, 99.9%), cobalt powder (Alfa Aesar, 99.9%) and nickel powder (Alfa Aesar, 99.9%). All manipulations during sample preparation were carried out in an argon-filled glovebox (content of $\text{O}_2 < 0.5 \text{ ppm}$).

Synthesis of $\text{GdNi}_{3-x-y}\text{Co}_x\text{Al}_y$. All the compounds were prepared by argon arc melting on a water-cooled copper crucible from elemental ingots with a purity of 99.9%. The $\text{GdNi}_{3-x-y}\text{Co}_x\text{Al}_y$ compounds were prepared by arc-melting of stoichiometric amounts of Gd, Co, Ni, and Al. The loss in weight was less than 1%. Each compound was re-melted four times to ensure homogeneity.

The samples were placed in carbon-coated quartz tubes, sealed and annealed at 1123K [(GdNiAl₂, GdCo_{0.5}Ni_{0.5}Al₂, GdCo_{0.75}Ni_{0.25}Al₂), 1273K (GdCoAl₂) and 1223K (GdCo_{0.25}Ni_{2.5}Al_{0.25}, GdCo_{0.5}Ni₂Al_{0.5}, GdCoNiAl, GdCo_{1.5}Ni_{0.5}Al, GdCoNi_{1.5}Al_{0.5}, GdCo₂Al, GdCo_{1.5}NiAl_{0.5}, GdCo₂Ni_{0.5}Al_{0.5})] for 7days in an argon atmosphere and subsequently quenched in air..

4.2.2 Physical property Measurements

Magnetic and resistivity measurements of GdNi_{3-x-y}Co_xAl_y, were carried out on a Quantum Design Magnetic Property Measurement System using the Quantum Design superconducting quantum interference device (SQUID) magnetometer option and the Physical Property Measurement System (PPMS), respectively. Both field cooled (FC) and zero-field cooled (ZFC) measurements have been performed in the 2-400 K temperature range of with an applied field up to 0.01 T. Field-dependent magnetization measurements were performed at 2 K and above room temperature. The temperature dependence electrical resistivity measurements were carried out using the standard four-probe DC technique in the temperature-dependent resistivity measurements were also performed at 2 K with an applied field up to 7 T.

4.2.3 Structure Determination

Powder X-ray diffraction (PXRD) measurements were performed on the powdered samples of GdNi_{3-x-y}Co_xAl_y using a PANalytical Empyrean X-ray Powder Diffractometer operating at 45 kV/40 mA with (Cu Kα1, $\lambda = 1.540598$) radiation. The lattice parameters and crystal structure of the samples were analyzed by Rietveld refinement using the FULLPROF software.

4.3 Results and Discussion

4.3.1 Structural Characterization

The synthesis of the polycrystalline GdNiAl₂, GdCo_{0.5}Ni_{0.5}Al₂, GdCo_{0.75}Ni_{0.25}Al₂, GdCoAl₂, GdCo_{0.25}Ni_{2.5}Al_{0.25}, GdCo_{0.5}Ni₂Al_{0.5}, GdCoNiAl, GdCo_{1.5}Ni_{0.5}Al, GdCoNi_{1.5}Al_{0.5}, GdCo₂Al, GdCo_{1.5}NiAl_{0.5} and GdCo₂Ni_{0.5}Al_{0.5} compounds were reproduced by a stoichiometric reaction of the elements using the arc melting synthetic approach. Figure 4.1 a-c shows the Rietveld

refinements for PXRD data of $\text{GdCo}_x\text{Ni}_{1-x}\text{Al}_2$, $\text{GdCo}_x\text{Ni}_{3-x-y}\text{Al}_y$ and GdCoAl_2 respectively. All the compounds except $\text{GdCo}_{0.5}\text{Ni}_2\text{Al}_{0.5}$, $\text{GdCo}_{1.5}\text{Ni}_{0.5}\text{Al}$, $\text{GdCoNi}_{1.5}\text{Al}_{0.5}$, and $\text{GdCo}_{1.5}\text{NiAl}_{0.5}$ contain either GdNi_3 (0.3 wt%) or NiAl (0.2% wt%) as a secondary phase.

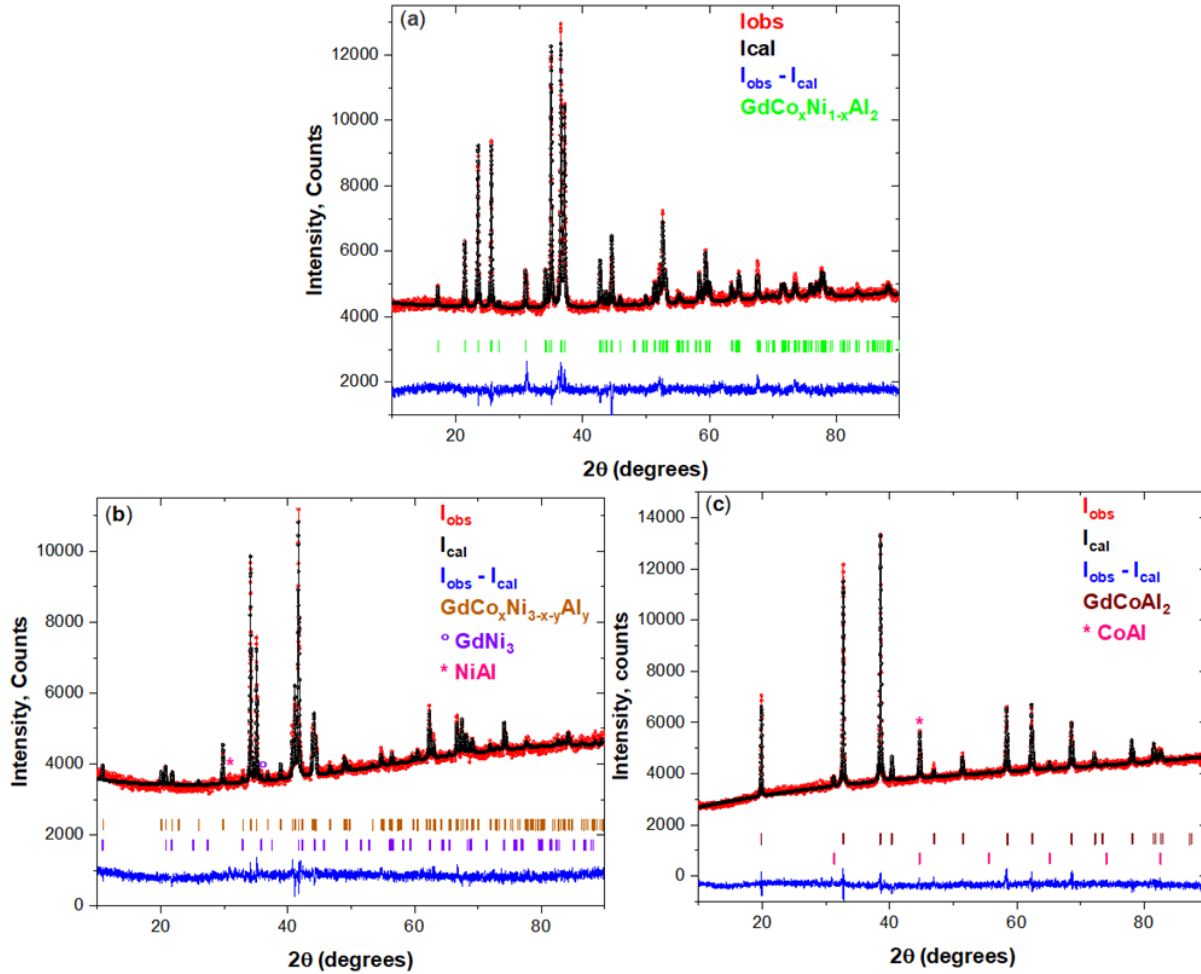


Figure 4.1. Rietveld refinement of the powder X-ray diffraction patterns of (a) $\text{GdCo}_x\text{Ni}_{1-x}\text{Al}_2$, (b) $\text{GdCo}_x\text{Ni}_{3-x-y}\text{Al}_y$, (c) GdCoAl_2 .

The Rietveld refinement of all the compounds showed that the major phases contain about 98-99 wt% of the hexagonal ($P6_3/mmc$) structure for $\text{GdCo}_{0.25}\text{Ni}_{2.5}\text{Al}_{0.25}$, $\text{GdCo}_{0.5}\text{Ni}_2\text{Al}_{0.5}$, GdCoNiAl , $\text{GdCo}_{1.5}\text{Ni}_{0.5}\text{Al}$, $\text{GdCoNi}_{1.5}\text{Al}_{0.5}$, GdCo_2Al , $\text{GdCo}_{1.5}\text{NiAl}_{0.5}$ (Fig. 4.1a). The remaining compounds, GdNiAl_2 , $\text{GdCo}_{0.5}\text{Ni}_{0.5}\text{Al}_2$, $\text{GdCo}_{0.75}\text{Ni}_{0.25}\text{Al}_2$ (Fig. 4.1b) and GdCoAl_2 (Fig. 4.1c) however, contain the Orthorhombic ($Cmcm$) and cubic ($Fd-3m$) structure respectively. The refined lattice parameters of all the compounds from Rietveld refinements are listed in Table 4.1. As can be seen from Table 4.1, the lattice parameters and unit cell volume of all the compounds, especially

the Co-doped ones, increase with increasing Co concentration. The unit cell parameters (a , c , V) for the GdNiAl_2 compound is in good agreement with those presented in the literature.¹⁴

Table 4.1. Lattice parameters from Rietveld refinements of the powder X-ray diffraction data of $\text{GdNi}_{3-x-y}\text{Co}_x\text{Al}_y$.

Compound	$a/\text{\AA}$	$c/\text{\AA}$	$V/\text{\AA}^3$	Structure
GdNiAl_2	4.08	6.93	286.7	Cmcm
$\text{GdCo}_{0.5}\text{Ni}_{0.5}\text{Al}_2$	4.060	6.95	290.8	Cmcm
$\text{GdCo}_{0.75}\text{Ni}_{0.25}\text{Al}_2$	4.058	6.98	291.5	Cmcm
GdCoAl_2	7.780	7.78	470.4	$\text{Fd}\bar{3}\text{m}$
$\text{GdCo}_{0.25}\text{Ni}_{2.5}\text{Al}_{0.25}$	5.048	16.34	360.6	$\text{P6}_3/\text{mmc}$
$\text{GdCo}_{0.5}\text{Ni}_2\text{Al}_{0.5}$	5.109	16.26	367.7	$\text{P6}_3/\text{mmc}$
GdCoNiAl	5.262	15.84	379.6	$\text{P6}_3/\text{mmc}$
$\text{GdCo}_{1.5}\text{Ni}_{0.5}\text{Al}$	5.257	15.95	381.8	$\text{P6}_3/\text{mmc}$
$\text{GdCoNi}_{1.5}\text{Al}_{0.5}$	5.110	16.30	384.1	$\text{P6}_3/\text{mmc}$
GdCo_2Al	5.218	16.27	385.2	$\text{P6}_3/\text{mmc}$
$\text{GdCo}_{1.5}\text{NiAl}_{0.5}$	5.112	16.31	400.1	$\text{P6}_3/\text{mmc}$
$\text{GdCo}_2\text{Ni}_{0.5}\text{Al}_{0.5}$	5.104	16.34	414.6	$\text{P6}_3/\text{mmc}$

4.3.2 Crystal Chemistry

The substitution of Co for Ni in GdNiAl_2 ($\text{GdNi}_{1-x}\text{Co}_x\text{Al}_2$) maintained the orthorhombic (Cmcm) structure as indicated by figure 4.1a. The structure, however, changed from the Cmcm to a hexagonal ($\text{P6}_3/\text{mmc}$) structure when either Ni or Al in GdNiAl_2 , has been substituted with Co ($\text{GdNi}_{3-x-y}\text{Co}_x\text{Al}_y$). The crystal structure of GdNiAl_2 and $\text{GdNi}_{3-x-y}\text{Co}_x\text{Al}_y$ compounds are shown in figure 4.2. The structure of GdNiAl_2 can be described to be analogous to the MgCuAl_2 type structure. The Gd, Ni, and Al atoms are located on the Mg, Cu, and Al site of the prototype, respectively. The GdNiAl_2 crystal structure has a polyanionic $[\text{NiAl}_2]^{\delta-}$ framework, with the cavities filled with Gd cations. In addition, the Gd and Al atoms form a tricapped trigonal prism shape around the Ni atoms.

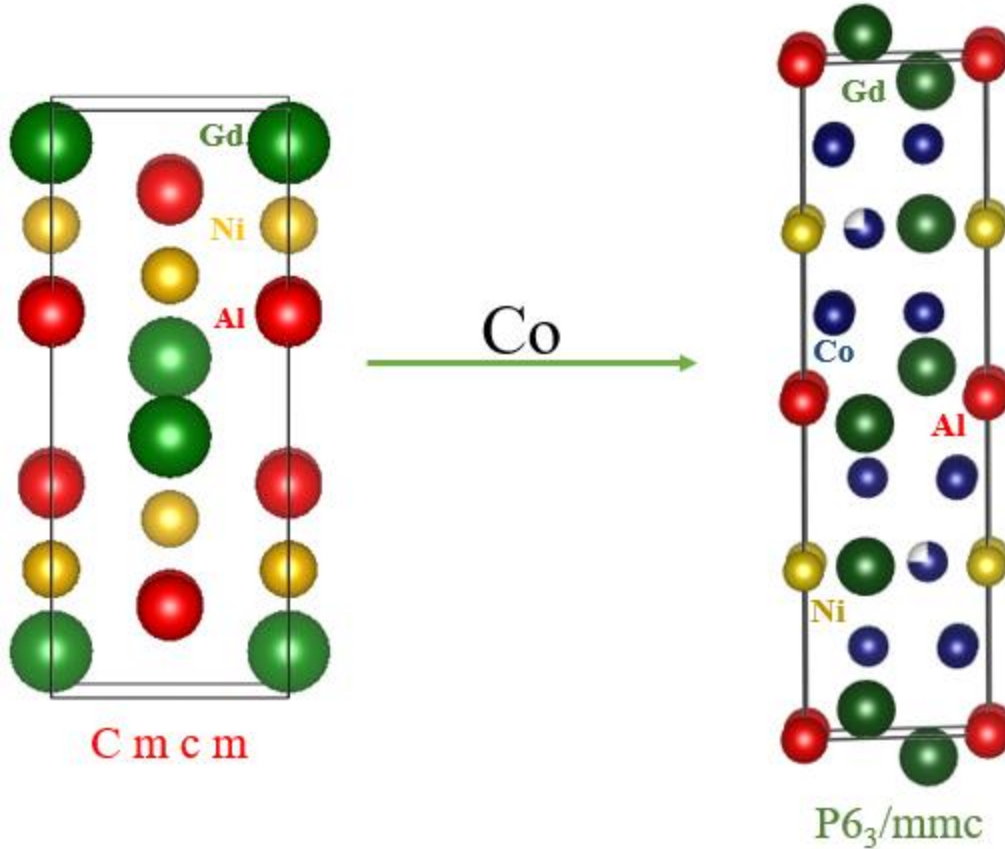


Figure 4.2. Crystal structure of GdNiAl_2 (left) and $\text{GdNi}_{3-x-y}\text{Co}_x\text{Al}_y$ (right)

$\text{GdNi}_{3-x-y}\text{Co}_x\text{Al}_y$ has a CeNi_3 crystal-type structure. This compound is in the form of the GdNi_3 series where the Ni, Co and Al occupy the same site. The Gd and (Ni, Co, Al) atoms in $\text{GdNi}_{3-x-y}\text{Co}_x\text{Al}_y$ compound occupy the 3a (0;0;0) and 6c (0;0;z) positions, respectively in the structure, as shown in Figure 4.2b. The structure of CeNi_3 consists of RT_2 (MgZn₂-type structure) and RT_5 (CaCu₅ structure type) blocks, which alternate in the direction perpendicular to the z-axis.

4.3.3 Magnetic Properties of $\text{GdNi}_{3-x-y}\text{Co}_x\text{Al}_y$ phases

To probe the effects of Ni and Al substitution by Co on the magnetic behavior of $\text{GdNi}_{3-x-y}\text{Co}_x\text{Al}_y$ samples, temperature-dependent magnetic susceptibility data (Figs 3a-f and 4g-l) were collected. Low-temperature FC and ZFC magnetic susceptibility data were measured under 0.01 T applied magnetic field in the temperature range of 2 to 400 K. All samples show Ferromagnetic (FM) behavior with a transition temperature (T_C) ~ 32, 110, 137 K (Fig. 4.3a) for GdNiAl_2 , $\text{GdCo}_{0.5}\text{Ni}_{0.5}\text{Al}_2$, $\text{GdCo}_{0.75}\text{Ni}_{0.25}\text{Al}_2$, respectively. The T_C values for the remaining compounds are

listed in table 4.2. In addition, a magnetic transition at 340 K is also observed on the temperature-dependent FC susceptibility of $\text{GdCo}_2\text{Ni}_{0.5}\text{Al}_{0.5}$ as shown in figure 4.3b. One can observe from the results that while the Curie temperature, T_c , of $\text{GdNi}_{3-x-y}\text{Co}_x\text{Al}_y$ samples increases with the increasing Co content, this interdependence is not monotonic. This increase in T_c is likely due to the decrease in the VEC at the transition metal magnetic centers as well as the substitution of a magnetic Co for a non-magnetic Al.

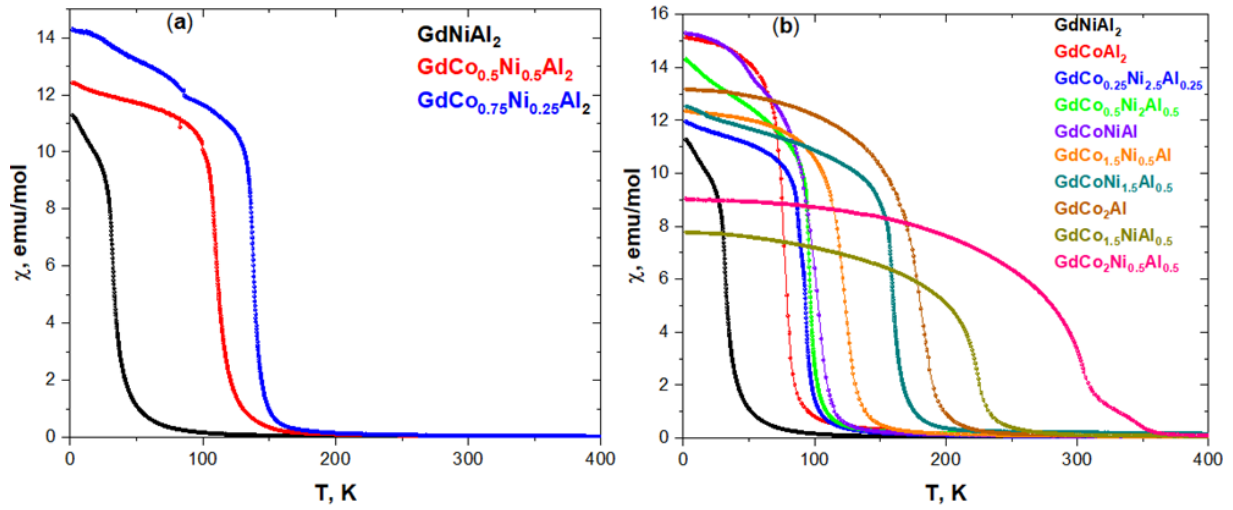


Figure 4.3. Magnetization vs temperature of (a) $\text{GdCo}_x\text{Ni}_{1-x}\text{Al}_2$, (b) $\text{GdCo}_x\text{Ni}_{3-x}\text{Al}_y$ compounds in applied field of 0.01 T.

The FC susceptibility and its inverse were fit to the Curie Weiss law, $\chi = C/(T - \theta) + \chi_0$, where C is the Curie constant, θ is the Weiss constant, and χ_0 is temperature independent paramagnetism. The fit turned out to be very sensitive to χ_0 , due to the relatively limited linear range available in the high-temperature region. The effective magnetic moment estimated from the partially constrained Curie–Weiss fit was calculated using $\mu = (8C)^{1/2}$. The results for this fit are listed in table 4.2. All these values are slightly higher than the value of $7.94 \mu_B$ expected for Gd^{3+} ion. The $\mu_{\text{eff}}/\text{fu}$ values from the transition metal sublattice are also listed in table 4.2. The values show a significant contribution of the transition metals towards the magnetic properties observed in these compounds.

Table 4.2. Magnetic properties $\text{GdCo}_x\text{Ni}_{3-x-y}\text{Al}_y$ compounds: effective magnetic moment per formula unit (M_{eff}/fu) and per transition metals (M_{eff}/T), saturation magnetization per formula unit M_{sat}/fu at 2K and curie temperature (T_c)

Compound	M_{eff}/fu (μ_B)	M_{eff}/T (μ_B)	M_{sat}/fu (μ_B)	T_c (K)
GdNiAl ₂	8.91	4.04	7.70	32
GdCo _{0.5} Ni _{0.5} Al ₂	9.24	4.73	7.89	110
GdCo _{0.75} Ni _{0.25} Al ₂	9.05	4.34	7.89	137
GdCoAl ₂	9.22	4.68	7.30	78
GdCo _{0.25} Ni _{2.5} Al _{0.25}	10.49	4.13	7.48	93
GdCo _{0.5} Ni ₂ Al _{0.5}	10.57	4.41	7.36	91
GdCoNiAl	9.20	3.29	7.20	102
GdCo _{1.5} Ni _{0.5} Al	9.91	4.19	7.16	122
GdCoNi _{1.5} Al _{0.5}	10.76	4.59	7.09	157
GdCo ₂ Al	8.82	2.72	6.50	188
GdCo _{1.5} NiAl _{0.5}	8.97	2.64	6.40	222
GdCo ₂ Ni _{0.5} Al _{0.5}	7.97	0.44	5.60	306

The Weiss temperature is highly dependent on the temperature range of the fit. However, the overall trend is that θ increases as Co is incorporated into the lattice. The fit to the Curie-Weiss law yields positive paramagnetic Weiss temperatures of 103, 133, 87, 86, 95, 162, 125, 161, 191, 225 and 316 K for GdCo_{0.5}Ni_{0.5}Al₂, GdCo_{0.75}Ni_{0.25}Al₂, GdCoAl₂, GdCo_{0.25}Ni_{2.5}Al_{0.25}, GdCo_{0.5}Ni₂Al_{0.5}, GdCoNiAl, GdCo_{1.5}Ni_{0.5}Al, GdCoNi_{1.5}Al_{0.5}, GdCo₂Al, GdCo_{1.5}NiAl_{0.5} and GdCo₂Ni_{0.5}Al_{0.5} respectively. The positive value is an indication of FM dominant nearest neighbor interaction in these systems. However, the parent compound GdNiAl₂ yielded a negative paramagnetic Weiss temperature of -9K indicating an anti-ferromagnetic nearest neighbor interaction between the Gd and Ni magnetic sublattices.

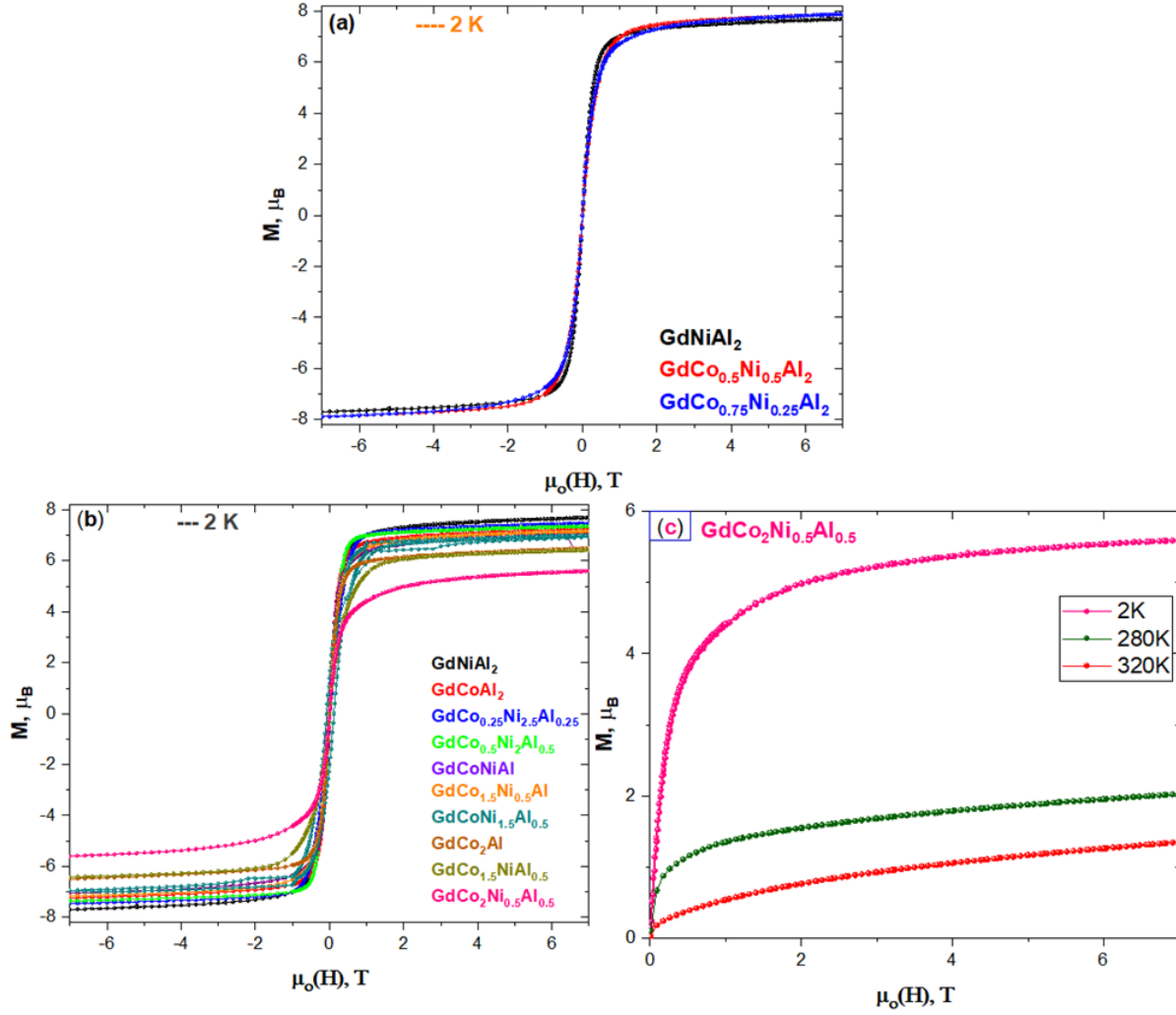


Figure 4.4. Magnetization vs magnetic field of (a) $GdCo_xNi_{1-x}Al_2$, (b) $GdCo_xNi_{3-x}Al_y$ compounds at 2 K and (c) $GdCo_2Ni_{0.5}Al_{0.5}$ at 2, 280, 320 K in fields up to 7 T.

The FM-like character of various $GdNi_{3-x-y}Co_xAl_y$ samples was further confirmed by isothermal magnetization measurements at various temperatures between 2 and 320 K under applied magnetic field sweeping from -7 to $+7$ T (Fig. 4.4a-c). The M - H curves for all samples display the characteristic S-shape hysteresis loop expected for FM materials. A negligible hysteretic behavior was observed in all the compounds, suggesting negligible magnetic anisotropy in the system. At 2 K, the saturation magnetization reaches a plateau of $\sim 7.7, 7.9, 7.9, 7.3, 7.5, 7.4, 7.1, 7.0, 7.0, 6.5$, and $6.4 \mu_B$ per formula unit (f.u.) at around 1 T for $GdNiAl_2$, $GdCo_{0.5}Ni_{0.5}Al_2$, $GdCo_{0.75}Ni_{0.25}Al_2$, $GdCoAl_2$, $GdCo_{0.25}Ni_{2.5}Al_{0.25}$, $GdCo_{0.5}Ni_2Al_{0.5}$, $GdCoNiAl$, $GdCo_{1.5}Ni_{0.5}Al$, $GdCoNi_{1.5}Al_{0.5}$, $GdCo_2Al$, $GdCo_{1.5}Ni_{0.5}Al_{0.5}$. It, however, reaches $5.6 \mu_B$ at 4 T for

GdCo₂Ni_{0.5}Al_{0.5}. Further, an increase in temperature for GdCo₂Ni_{0.5}Al_{0.5} (Fig. 4.4c) to 280 and 320 K further decreased the saturation magnetization value to 1.2 and 0.8 μ_B per formula unit (f.u.) respectively.

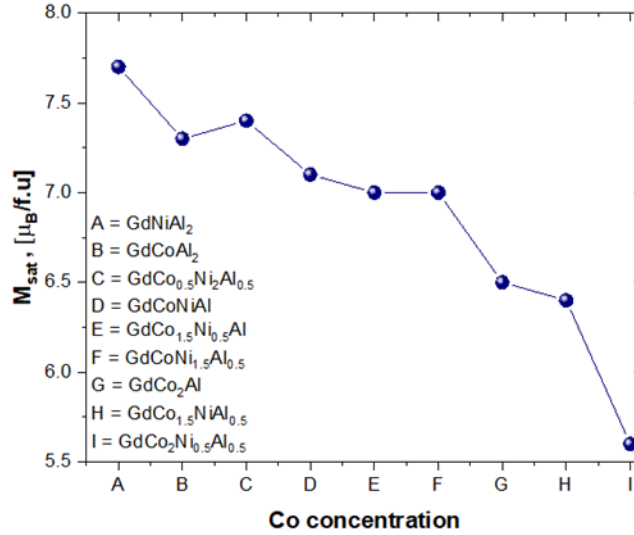


Figure 4.5. Saturation magnetic moments M_{sat} obtained from magnetization isotherms $M(H)$ measured at 2 K for the GdNi_{3-x-y}Co_xAl_y compounds.

The saturation magnetization values for GdNiAl₂, GdCo_{0.5}Ni_{0.5}Al₂, GdCo_{0.75}Ni_{0.25}Al₂, GdCoAl₂, GdCo_{0.25}Ni_{2.5}Al_{0.25}, GdCo_{0.5}Ni₂Al_{0.5}, GdCoNiAl are substantially larger compared to the theoretical ordered moment (7 μ_B) of Gd³⁺ ion. The value for GdCo_{1.5}Ni_{0.5}Al, GdCoNi_{1.5}Al_{0.5} compounds is close to the theoretical M_{sat} of Gd³⁺. However, the M_{sat} values are lower in GdCo₂Al, GdCo_{1.5}NiAl_{0.5}, GdCo₂Ni_{0.5}Al_{0.5}. The saturation magnetization values at 2 K becomes smaller with increasing Co concentration shown in Figure 4.5. This trend further indicates a large contribution from the Co spins to the overall magnetic moment, which helps in increasing the AFM nearest neighbor interaction between it and Gd magnetic sublattices. The results of magnetization measurements of the GdNi_{3-x-y}Co_xAl_y are summarized in Table 4.2.

4.3.4 Magnetocaloric effect of GdNi_{3-x-y}Co_xAl_y phases

A set of magnetic isothermals with decreasing and increasing applied fields were measured up to 5 T to get insight on the MCE of these compounds. The isothermal magnetic entropy change, ΔS_M , can be calculated by applying the Maxwell equation based on the measurement of isothermal M-H curves.

$$\Delta S_M = - \int H (\partial M / \partial T) H dH$$

where T, H, S_M , and M represent the temperature, applied magnetic field, the material magnetic entropy, and magnetization of the system, respectively.

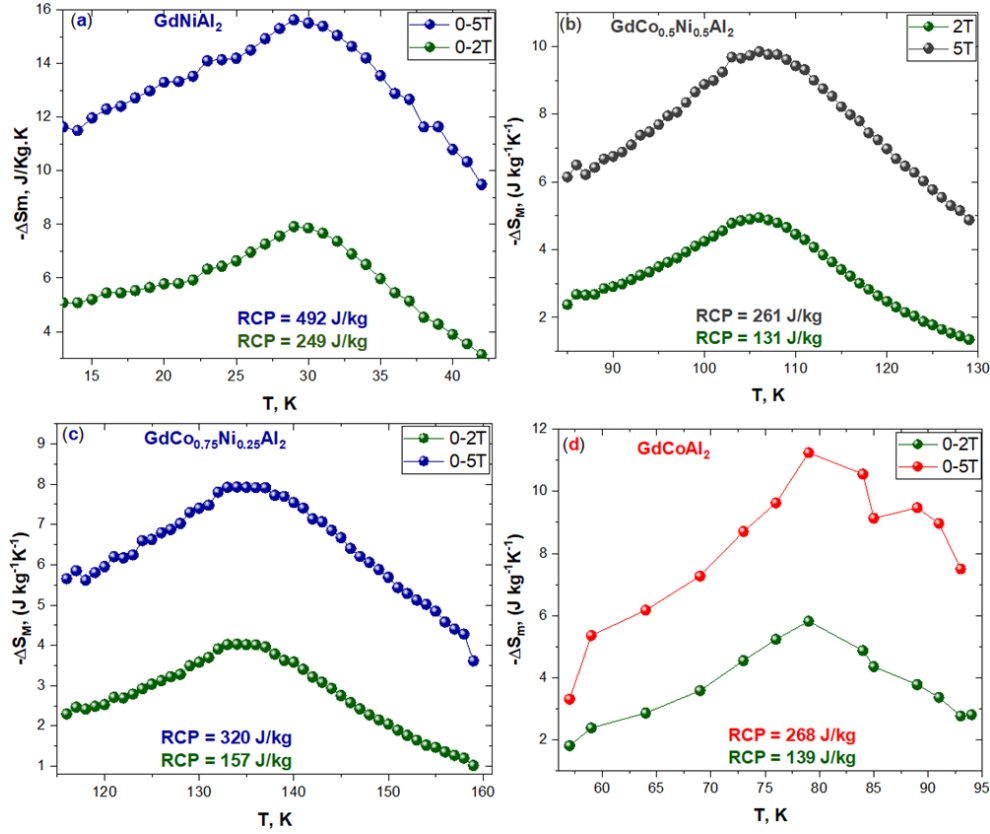


Figure 4.6 Isothermal magnetic entropy changes for (a) GdNiAl_2 (b) $\text{GdCo}_{0.5}\text{Ni}_{0.5}\text{Al}_2$, (c) $\text{GdCo}_{0.75}\text{Ni}_{0.25}\text{Al}_2$, (d) GdCoAl_2 for magnetic changes of $\mu_0\Delta H = 2$ T and 5 T.

The resulting $-\Delta S_M$ vs. T plots with the magnetic field changes up to 0-2 T and 0-5 T are displayed in Figures 4.6a-d, 4.7e-h, and 4.8i-l. For the magnetic field changes of 0-2, and 0-5 T, the values of $-\Delta S_M^{\max}$ evaluated are shown in table 4.3a and 4.3b. It can be observed from the $-\Delta S_M^{\max}$ that the entropy values at both 2 and 5T start to decrease with the introduction of Co. This decrease in the $-\Delta S_M$ can be attributed to the decrease in the magnetic saturation value (since the magnetic entropy depends on the magnetic magnetization value) as shown in figure 4.9a.

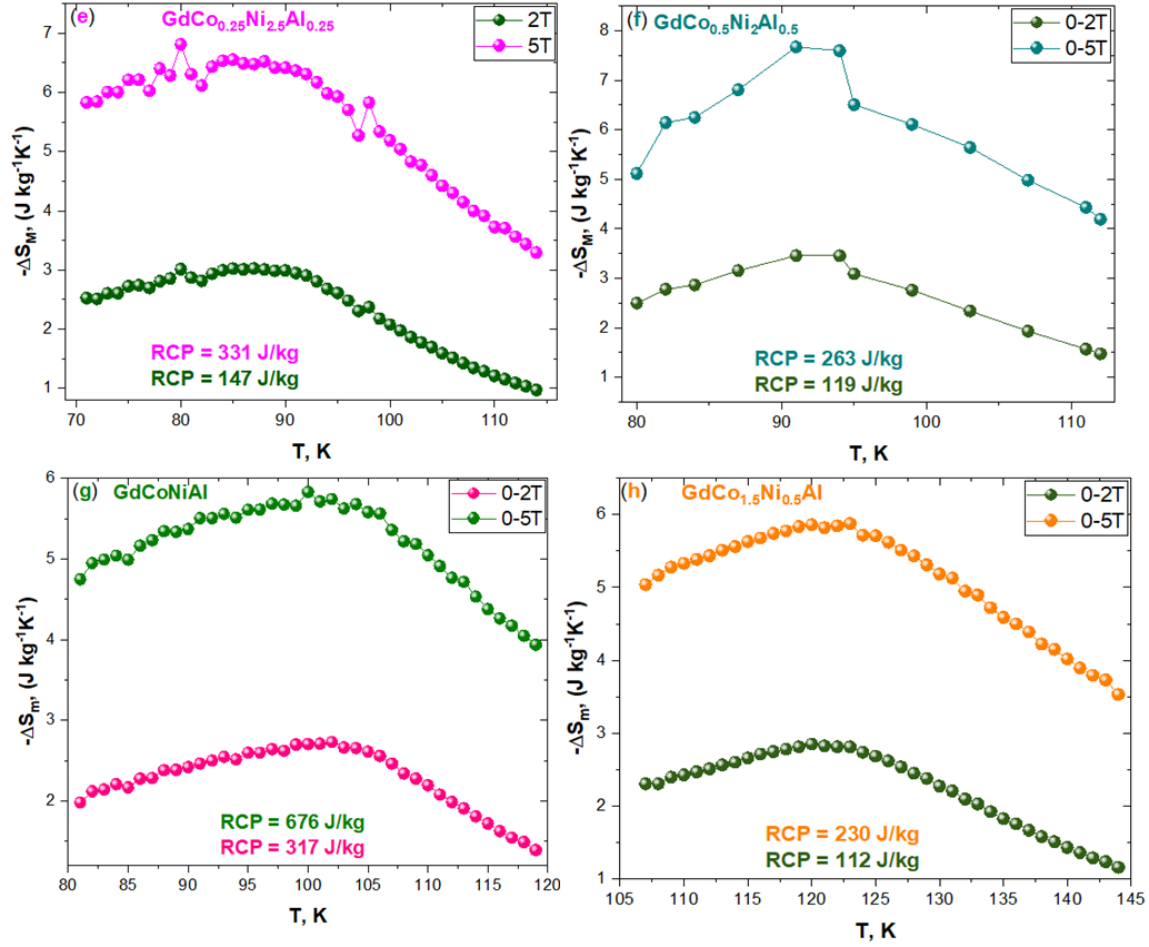


Figure 4.7. Isothermal magnetic entropy changes for (e) $\text{GdCo}_{0.25}\text{Ni}_{2.5}\text{Al}_{0.25}$, (f) $\text{GdCo}_{0.5}\text{Ni}_2\text{Al}_{0.5}$, (g) GdCoNiAl , (h) $\text{GdCo}_{1.5}\text{Ni}_{0.5}\text{Al}$, for magnetic changes of $\mu_0\Delta H = 2$ T and 5 T.

The Unit cell volume dependence of the Magnetic entropy change for the $\text{GdNi}_{3-x-y}\text{Co}_x\text{Al}_y$ compounds is shown in figure 4.9b. One can see a drastic decrease in the magnetic entropy value as the cobalt content increases. This behavior can be related to the randomly aligned atoms due to an increase in the unit cell volume from GdNiAl_2 (286.7 \AA^3) to $\text{GdCo}_2\text{Ni}_{0.5}\text{Al}_{0.5}$ (414.6 \AA^3). This random alignment of the magnetic spins causes loss in magnetic entropy, which is emanating from the energy needed to realign the magnetic spins by the field. Interestingly, the $-\Delta S_M(T)$ for most of the compounds spanned a wide range of temperatures. Such MCE characteristics are crucial for practical applications.

Large values of the RCP in J/kg at $\Delta H = 0-5\text{T}$ calculated for these compounds are shown in table 4.3a and 4.3b respectively. The RCP values obtained for GdNiAl_2 and GdCoNiAl are

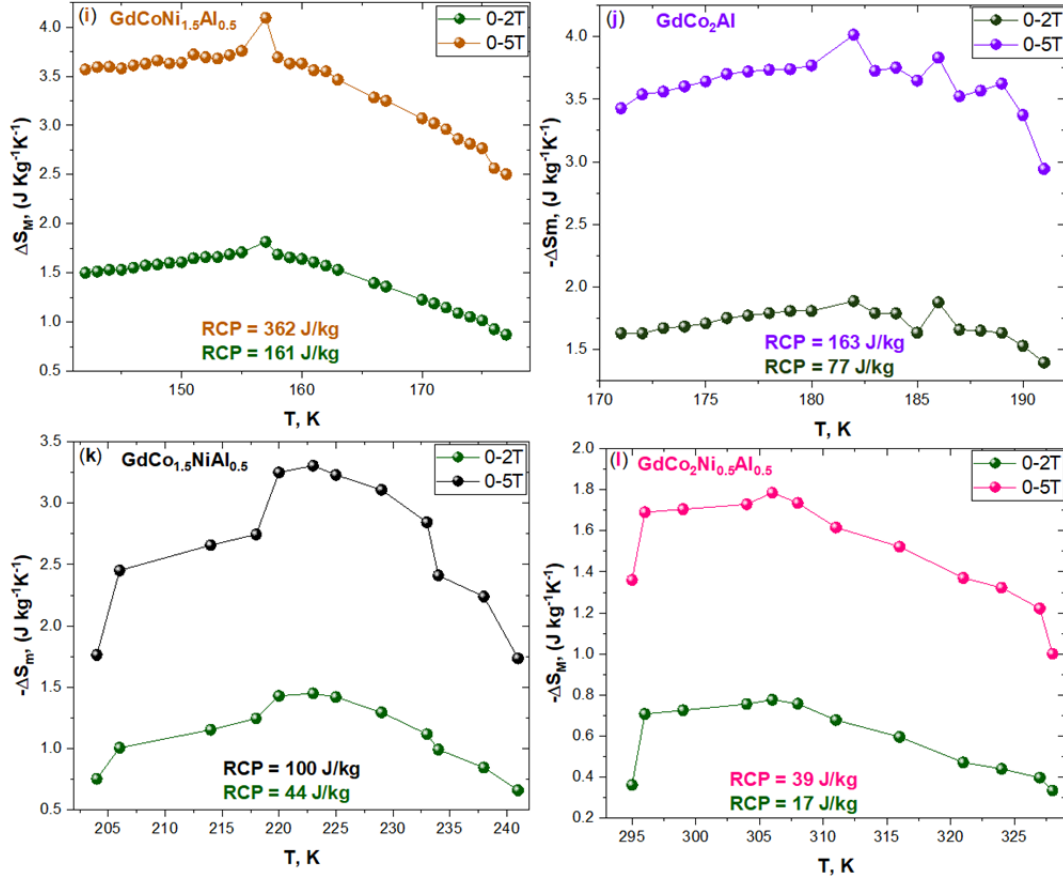


Figure 4.8. Isothermal magnetic entropy changes for (i) $\text{GdCoNi}_{1.5}\text{Al}_{0.5}$, (j) GdCo_2Al , (k) $\text{GdCo}_{1.5}\text{NiAl}_{0.5}$ and (l) $\text{GdCo}_2\text{Ni}_{0.5}\text{Al}_{0.5}$ for magnetic changes of $\mu_0 \Delta H = 2$ T and 5 T.

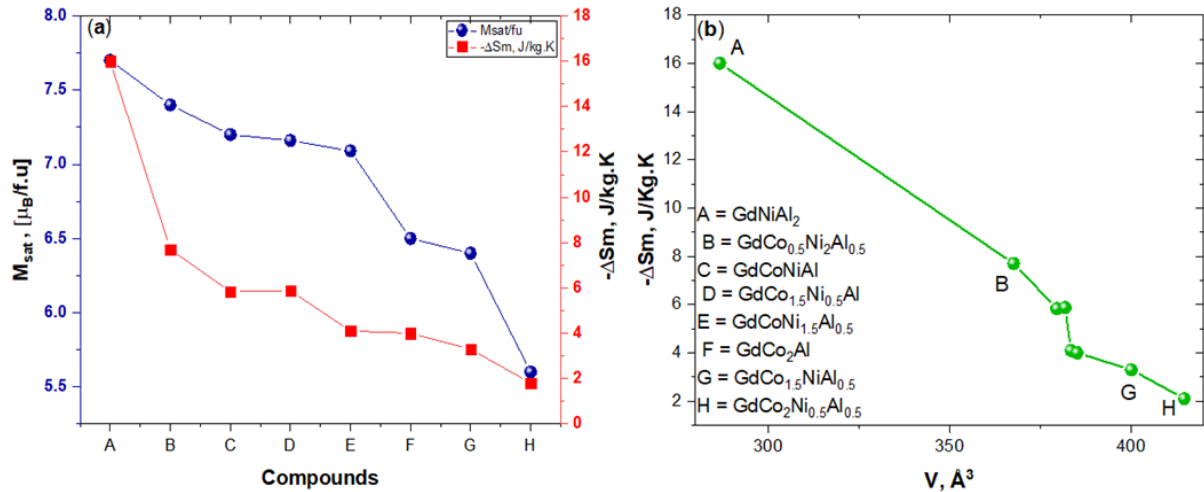


Figure 4.9. (a) Change of magnetic entropy and saturated magnetization versus the Co-concentration, (b) change of magnetic entropy versus the unit cell volume for the $\text{GdCo}_x\text{Ni}_{3-x}\text{Al}$ compounds.

greater than the best magnetocaloric prototype materials such as $\text{Gd}_5\text{Si}_2\text{Ge}_2$ and Gd with an RCP of 440 J/kg and 400 J/kg respectively .¹⁷ Due to the large RCP values for most of the compounds over a wide range of temperature, they can be considered as potential candidates for magnetic cooling technology. These values are comparable to other Gd-Ni-Al and Gd-Co-Al compounds, as shown in Table 4.3.

Table 4.3a. The T_C , $-\Delta S_M^{\max}$, and RCP for $\Delta H = 0-5$ T for $\text{GdNi}_{3-x-y}\text{Co}_x\text{Al}_y$ and some recently reported magnetocaloric materials

Compound	T_C (K)	$-\Delta S_M$	RCP(Jkg ⁻¹)	Ref
GdNiAl ₂	32	16.0	492	This work
GdCo _{0.5} Ni _{0.5} Al ₂	110	9.9	261	This work
GdCo _{0.75} Ni _{0.25} Al ₂	137	7.9	320	This work
Gd ₃ Ni ₈ Al	62	11.0	480	18
GdNiAl	66	10.6	460	19
GdCoAl ₂	79	11.2	268	This work
GdCo _{0.25} Ni _{2.5} Al _{0.25}	93	6.6	331	This work

Table 4.4b. The T_C , $-\Delta S_M^{\max}$, and RCP for $\Delta H = 0-5$ T for $\text{GdNi}_{3-x-y}\text{Co}_x\text{Al}_y$ and some recently reported magnetocaloric materials

Compound	T_C (K)	$-\Delta S_M$	RCP(Jkg ⁻¹)	Ref
GdCo _{0.5} Ni ₂ Al _{0.5}	91	7.7	263	This work
GdCoAl	100	10.4	-	20
GdCoNiAl	100	5.83	676	This work
GdCo _{1.5} Ni _{0.5} Al	123	5.88	230	This work
GdCoNi _{1.5} Al _{0.5}	157	4.1	362	This work
GdCo ₂ Al	188	4.0	163	This work
GdCo _{1.5} NiAl _{0.5}	222	3.3	100	This work
GdCo ₂ Ni _{0.5} Al _{0.5}	306	1.8	39	This work

4.3.5 Magnetoresistance of GdCo₂Al

Corroborating the magnetic properties of GdCo₂Al, the temperature dependence of the electrical resistivity $\rho(T)$ was measured at different fields from room temperature down to $T = 2$ K. The temperature-dependent $\rho(T)$ of the GdCo₂Al at both 0 and 7 T (Fig. 4.10) decrease linearly with decreasing temperature, typical behavior for metallic compounds. Interestingly, two upturns were observed at (50, 250 K) and (100, 250 K) for 0 T and 7 T respectively. The anomaly at these temperatures at not seen in our magnetic measurement (figure 4.3b). A small negative magnetoresistance effect of $MR = 0.8\%$ in a 7 T field at 2 K is observed, as shown in the inset to Figure 4.10, consistent with partial suppression of the spin scattering term.

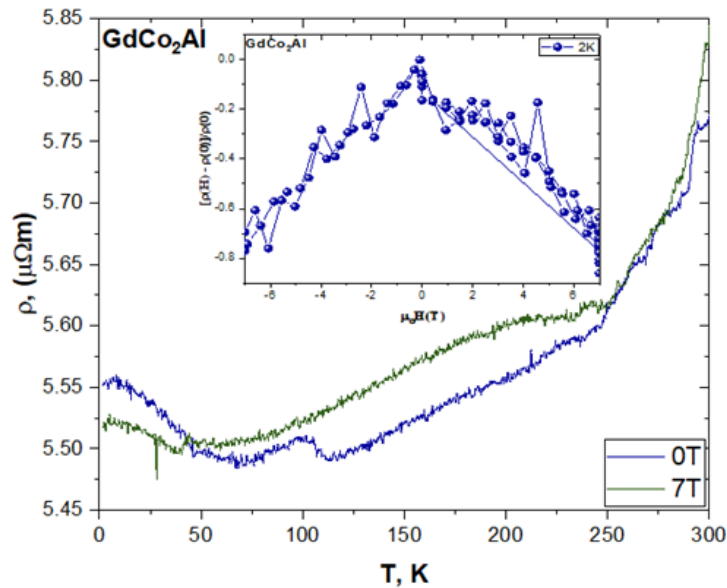


Figure 4.10. Resistivity as a function of temperature at 0 and 7T applied magnetic fields for GdCo₂Al. Inset magnetoresistance as a function of applied field at 2K.

4.4 Conclusion

A new system of intermetallic compounds GdNi_{3-x-y}Co_xAl_y has been studied. The influence of partial substitution of Ni and Al by Co in GdNi_{3-x-y}Co_xAl_y on the MCEs, magnetic phase transitions, magnetic properties, and crystal structure were investigated. The experimental results show that with the exception of GdCoAl₂ (cubic, Fd-3m), Cmc₂m (GdCo_{0.5}Ni_{0.5}Al₂, GdCo_{0.75}Ni_{0.25}Al₂), all the compounds adopt the hexagonal (P6/mmc) space group. The unit cell parameters for the hexagonal based compounds increases with increasing Co concentration. A

magnetic PM to FM transition was found, which was characterized by rare-earth-transition metal exchange interactions (Gd-Co/Ni) interaction. The curie temperature T_C increased on increasing Co concentration which is due to the reduction in the VEC at the transition metal magnetic centers.

The saturation magnetization value decreased with increasing the Co concentration indicating the compound $GdNi_{3-x-y}Co_xAl_y$ possesses ferrimagnetic behavior, with the magnetic spins of Gd and Co-Ni sublattices ordering antiparallel to each other. Large values of magnetic entropy changes were observed near T_C . The peak values of the magnetic entropy change in the vicinity of T_C $\Delta H = 0-5$ T were found to decrease from 15.8 to 1.8 J kg⁻¹K⁻¹ for $GdNiAl_2$ to $GdCo_2Ni_{0.5}Al_{0.5}$ respectively. Large values of the RCP = 492 and 676 J/kg were found corresponding to the compounds $GdNiAl_2$ and $GdCoNiAl$, respectively, with $\Delta H = 0-5$ T. Some of the values obtained are comparable to the best magnetocaloric prototype materials such as $Gd_5Si_2Ge_2$ and Gd with an RCP of 440 J/kg and 400 J/kg respectively. This suggests that $GdNi_{3-x-y}Co_xAl_y$ may be considered as a potential candidate for the magnetic refrigerant.

4.5 References

1. R. Nirmala, Ya. Mudryk, V. K. Pecharsky, and K. A. Gschneidner, Jr., Phys. Rev. B 76, 014407 (2007).
2. K. A. Gschneidner, Jr., V. K. Pecharsky, and A. O. Tsokol, Rep. Prog. Phys. 68, 1479 (2005).
3. V. Franco, J.S. Blázquez, B. Ingale, A. Conde, Ann. Rev. Mater. Res. 42 (2012) 305.
4. K.A. Gschneidner Jr., V.K. Pecharsky, A.O. Tsokol, Rep. Prog. Phys. 68 (2005) 1479.
5. B.G. Shen, J.R. Sun, F.X. Hu, H.W. Zhang, Z.H. Cheng, Adv. Mater. 21 (2009) 4545.
6. L. Li, K. Nishimura, W.D. Hutchison, Z. Qian, D. Huo, T. Namiki, Appl. Phys. Lett. 100 (2012) 152403.
7. L. Li, O. Niehaus, M. Kersting, R. Pöttgen, Appl. Phys. Lett. 104 (2014) 092416.
8. R. Nirmala, A.V. Morozkin, R. Rajivgandhi, A.K. Nigam, S. Quezado, S.K. Malik, J. Magn. Magn. Mater. 418 (2016) 118.
9. Ling-wei Li, Chin. Phys. B 25 (2016) 037502.
10. L. Li, G. Hu, Y. Qi, I. Umehara, Sci. Rep. 7 (2017) 42908.
11. J.C. Debnath, J. Wang, Intermetallics 78 (2016) 50.

12. L.W. Li, M. Kadonaga, D.X. Huo, Z.H. Qian, T. Namiki, K. Nishimura, Appl. Phys. Lett. 101 (2012) 122401
13. Y. Zhang, D. Guo, Y. Yang, J. Wang, S. Geng, X. Li, Z. Ren, G. Wilde, Intermetallics 88 (2017) 61–64.
14. S.N. Dembele, Z. Ma, Y.F. Shang, H. Fu, E.A. Balfour, R.L. Hadimani, D.C. Jiles, B.H. Teng, Y. Luo, Journal of Magnetism and Magnetic Materials 391 (2015) 191–194
15. A. Bajorek, A. Chrobak, G. Chełkowska, M. Kwiecien-Grudziecka, Journal of Alloys and Compounds 494 (2010) 22–27.
16. A. Bajorek, A. Chrobak, G. Chełkowska, M. Kwiecien-Grudziecka, Journal of Alloys and Compounds 485 (2009) 6–12.
17. V. K. Pecharsky, K. A. Gschneidner Jr., Phys. Rev. Lett. 1997, 78, 4494–4497.
18. M. X. Wang, H. FU, Q. Zheng and J. Tang, Modern Physics Letters B Vol. 26, No. 25 (2012) 1250167.
19. M. Oboz, E. Talik, J. Alloys Comp. 509 (2011) 5441.
20. X.X. Zhang, F.W. Wang, G.H. Wen, J. Phys.: Condens. Matter 13 (2001) L747.

CHAPTER 5. MAGNETOCALORIC EFFECT (MCE) AND MAGNETIC PROPERTIES OF GdNiGa_2 AND THE CO-DOPED GADOLINIUM NICKEL GALLIDES ($\text{GdNi}_{3-x-y}\text{Co}_x\text{Ga}_y$)

The studies described in chapter four focused on the magnetocaloric and structural properties of $\text{GdCo}_x\text{Ni}_{3-x-y}\text{Al}_y$. Most importantly, we have examined the effect of Co substitution in the Ni/Al sublattice on the magnetocaloric, magnetic, and structural properties of GdNiAl_2 material. One thing that is clear from the chapter above is the drastic decrease in the magnetic entropy value as the cobalt content increases. This behavior can be related to the randomly aligned atoms due to an increase in the unit cell volume from GdNiAl_2 (286.7 \AA^3) to $\text{GdCo}_2\text{Ni}_{0.5}\text{Al}_{0.5}$ (414.6 \AA^3). In the present chapter, what we sort to do is to control the unit cell volume in $\text{GdCo}_x\text{Ni}_{3-x-y}\text{Al}_y$ in order to mitigate the decrease in the MCE value. In the present chapter, we describe the extension of these studies to the gallium ($\text{GdCo}_x\text{Ni}_{3-x-y}\text{Ga}_x$) analogs, in order to understand the influence of changes in the unit cell volume and magnetocaloric properties. In the case of the ($\text{GdCo}_x\text{Ni}_{3-x-y}\text{Ga}_x$) system, Ga has metallic radius ($r_{\text{Ga}} = 1.35 \text{ \AA}$) smaller than that of Al ($r_{\text{Al}} = 1.43 \text{ \AA}$), which minimizes the unit cell volume effects.

5.1 Introduction

Conventional gas expansion/compression refrigeration technology is the leading cooling application in modern society today.¹⁻² However, the compressing and expanding processes based on gas expansion/compression has environmental and energy efficiency drawbacks.³⁻⁴ A promising alter-native technology (Magnetic refrigeration) based on the MCE provides an alternative for cooling technology applications with high energy efficiency, environmental friendliness and low power consumption advantages.⁵⁻¹¹ To be an alternative to the conventional gas compression/expansion refrigeration devices and to replace it in the immediate future, magnetic cooling systems require materials with improved magnetocaloric properties.¹²⁻¹⁶ The MCE is intrinsic to all magnetic materials; however, the magnitude of the MCE depends on the properties of the respective magnetic material and how strongly their magnetic spins are attracted to the magnetic field applied.

The magnetocaloric properties of many rare-earth based intermetallic systems have been comprehensively studied over the last three decades, targeting not only an application in the field

of this technology but also expanding the basic understanding of the behaviors of these materials.¹⁷⁻
¹⁸ The most popularly known examples are the $\text{Gd}_5\text{Si}_2\text{Ge}_2$, MnFePAs , MnAs , NiMnSn , and LaFeSi , etc.¹⁹⁻²⁶ This technology has extended functionality for ultra-low temperature in various cryogenic applications such as cryogenic technology in space science, hydrogen gas liquefaction, and other fuel gases, etc. An example of such low temperature, MCE phases include ErCo_2 , TmZn , Gd_2CuSi_3 , Ho_5Pd_2 , Tb_3Co , ErAl_2 , HoCuGe , $\text{Ho}_2\text{Cu}_2\text{Cd}$, etc.²⁷⁻³⁸

To quantify the quality of a magnetocaloric material for sub-room temperature (250-290 K) application, several indicators are of interest. The magnetic entropy change, which is usually estimated at different magnetic fields must be relatively high. Field changes of 0-2 T up to 0-5 T are utilized depending on the application.³⁹ In addition, the RCP is estimated, which is a measure of the amount of heat transferred from the hot to the cold sinks and vice versa in one thermodynamic cycle of a magnetic refrigerator and must also be large. Thus, a large entropy changes in a wide temperature range is required.⁴⁰ Heat capacity (CP) is also another parameter, a low amount of it is needed since a high amount of it increases the thermal load and large energy would be needed to heat the sample itself, which will result in an entropy loss.

The ternary intermetallic RTAl_2 ,⁴¹⁻⁴⁹ RTGa_2 ⁵⁰⁻⁵⁷ and RTIn_2 ⁵⁷⁻⁷⁷ and RTTl_2 ⁷⁸⁻⁸⁰ (R-rare earth, T = Ni, Cu, Pt, Pd) compounds have been studied extensively over the course of the last 10–20 years, with a focus on their physical properties. These group of compounds adopts the MgCuAl_2 -type structure with an orthorhombic, Cmcm space group.⁸¹⁻⁸² The RNiAl_2 are the most investigated due to their exotic magnetic and interesting magnetocaloric properties they show. Complex magnetic behaviors and low transition temperatures (Gd = 28 K, Tb = 11.7, 20 K, Ho = 7.8 K, Er = 5.1 K, Tm = 2.4/4.0 K), were observed in these materials. The magnetic and magnetocaloric ($-\Delta S_M = 16.0 \text{ Jkg}^{-1}\text{K}^{-1}$, 5 T) properties of the GdNiAl_2 compound was studied. The magnetocaloric properties of the TbNiAl_2 with an entropy value of $13.8 \text{ Jkg}^{-1}\text{K}^{-1}$ was obtained. In addition, the magnetocaloric effect of HoNiAl_2 ($-\Delta S_M = 14.0 \text{ Jkg}^{-1}\text{K}^{-1}$, 5 T), ErNiAl_2 ($-\Delta S_M = 21.2 \text{ Jkg}^{-1}\text{K}^{-1}$, 5 T) and TmNiAl_2 ($-\Delta S_M = 20.7 \text{ Jkg}^{-1}\text{K}^{-1}$, 5 T) was recently discovered.⁸³⁻⁸⁴

In contrast, the magnetocaloric properties of the gallides, indides, and thallides analogs have not yet been studied to the best of our knowledge. Here, we report on the investigations of the magnetic and the magnetocaloric properties of GdNiGa_2 and its Co substituted ($\text{GdNi}_{3-x-y}\text{Co}_x\text{Ga}_y$) variants.

5.2 Experimental details

5.2.1 Synthesis

General Details. The following reagents were used as received: Finely dispersed powder of gadolinium (Alfa Aesar, 99.9%), Gallium ingot (Alfa Aesar, 99.9%), cobalt powder (Alfa Aesar, 99.9%) and nickel powder (Alfa Aesar, 99.9%). All manipulations during sample preparation were carried out in an argon-filled glovebox (content of O₂ < 0.5 ppm).

Synthesis of GdNi_{3-x-y}Co_xGa_y. The stoichiometric amounts of all the compounds with a purity of 99.9% on a water-cooled copper crucible, were prepared in a high-purity argon atmosphere by arc-melting. The GdNi_{3-x-y}Co_xGa_y compounds were prepared by arc-melting of stoichiometric amounts of Gd, Co, Ni, and Ga. The loss in weight was less than 1%. Each compound was re-melted several times to ensure compositional homogeneity. The samples were placed in carbon-coated quartz tubes, sealed and annealed at 1123K (GdNiGa₂), 1173K (GdCo_{0.25}Ni_{2.5}Ga_{0.25}) and 1223K (GdCo_{0.5}Ni₂Ga_{0.5}, GdCoNiAl, GdCo_{1.5}Ni_{0.5}Ga, GdCoNi_{1.5}Ga_{0.5}, GdCo₂Ga, GdCo_{1.5}NiGa_{0.5}, and GdCo₂Ni_{0.5}Ga_{0.5}) for 7days in an argon atmosphere and subsequently quenched in air.

5.2.2 Physical property Measurements

Magnetic measurements of GdNi_{3-x-y}Co_xGa_y, was carried out on a Quantum Design Magnetic Property Measurement System using the Quantum Design superconducting quantum interference device (SQUID) magnetometer option and the Physical Property Measurement System (PPMS), respectively. Both field cooled (FC) and zero-field cooled (ZFC) measurements have been performed in the 2-400 K temperature range of with an applied field up to 0.01 T. Field-dependent magnetization measurements were performed at 2 K and above room temperature.

5.2.3 Structure Determination

Powder X-ray diffraction (PXRD) measurements were carried on the powdered samples of GdNi_{3-x-y}Co_xGa_y using a PANalytical Empyrean X-ray Powder Diffractometer operating at 45 kV/40 mA with (Cu K α 1, λ = 1.540598) radiation. The lattice parameters and crystal structure of the samples were analyzed by Rietveld refinement using the FULLPROF software.

5.2.4 Energy dispersive X-ray Fluorescence (EDXRF) Data

Energy dispersive X-ray fluorescence (EDXRF) data were collected on the polycrystalline samples using a Malvern Panalytical Epsilon4 X-ray fluorescence spectrometer equipped with a 15 W silver anode X-ray tube, a ten-sample changer, and helium gas flush option, and an energy dispersive silicon drift detector.

Samples were packed as powders into XRF cups of appropriate sizes using either 4 μm polypropylene (“prolene”) or 3.6 μm mylar foil. Prior to data collection, a recalibration standard based on elements Al, Ca, Fe, K, Mg, Na, P, S and Si (“Omnian Monitor”) was measured for drift correction in the soft X-ray region. Data were collected using the Epsilon software¹⁾ employing the “Omnian” data collection procedure. Data were collected with six different acceleration voltages between 5 and 50 kV and varying thickness Ti, Al, Cu and Ag filters. Currents were set automatically so that the detector dead time does not exceed 50% (to avoid excessively large escape and sum peaks), or to the maximum tube power of 15W. Data were analyzed using the standardless Omnian procedure, with data processing parameters being defined prior to analysis for each type of sample using the Epsilon Dashboard software.²⁾ After automatic quantification, spectra were visually inspected for miss-assigned peaks and elements were removed or added as required before final reanalysis. Data are reported in weight % or weight ppm.

5.3 Results and Discussion

5.3.1 Structural Characterization

The PXRD patterns of RNiGa_2 and $\text{GdNi}_{3-x-y}\text{Co}_x\text{Ga}_y$ compounds shown in Fig. 5.1a-b were obtained at room temperature and then fitted by the Rietveld refinement method. Refinement results indicate that the GdNiGa_2 and $\text{GdNi}_{3-x-y}\text{Co}_x\text{Ga}_y$ adopt the orthorhombic (Cmcm) MgCuAl_2 -type and hexagonal ($\text{P6}_3/\text{mmc}$) CeNi_3 -type structure. Bragg peaks corresponding to impurity phases were observed for some of the compounds (Fig. D.1). The chemical composition of GdNiGa_2 and $\text{GdNi}_{3-x-y}\text{Co}_x\text{Ga}_y$ compounds was examined by Energy dispersive X-ray Fluorescence (EDXRF). Analysis of the result shows that the ratio of Gd, Co, Ni and Ga atoms for all the compounds are close (Table 2) to the nominal chemical composition. The lattice cell parameters of all the compounds listed in Table 1, were extracted from the refinement of the powder X-ray diffraction data. Figure 2 depicts the trend of the unit cell volumes, which increases

with increasing Co concentration due to different covalent radii for the transition metals. GdCoNiGa, GdCo_{1.5}Ni_{0.5}Ga, and GdCo₂Ga compounds were not included in figure 2 for the purpose of clarity. The exclusion was due to higher Ga concentration: larger covalent radius of Ga compares to the transition metals. The GdNiGa₂ compound was also not included due to different structure; hence different atoms per unit cell.

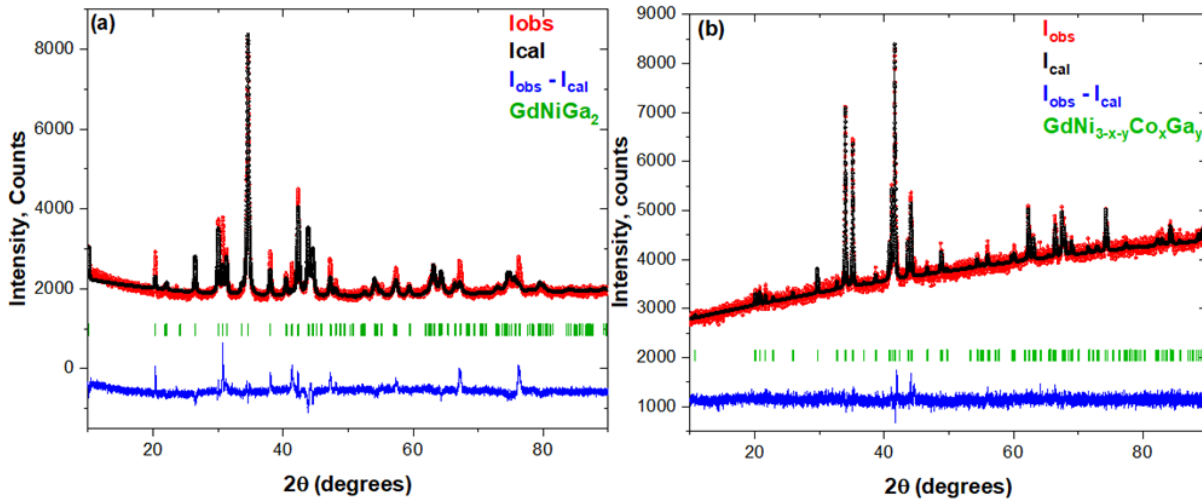


Figure 5.1. Rietveld refinement of the powder X-ray diffraction patterns of (a) GdNiGa₂, (b) GdNi_{3-x-y}Co_xGa_y.

Table 5.1. Lattice parameters from Rietveld refinements of the powder X-ray diffraction data of GdNiGa₂ GdNi_{3-x-y}Co_xGa_y

Compound	a/Å	c/Å	V/Å ³	Structure
GdNiGa ₂	4.13	4.06	292.9	Cmcm
GdCo _{0.25} Ni _{2.5} Ga _{0.25}	5.033	16.34	358.6	P6 ₃ /mmc
GdCo _{0.5} Ni ₂ Ga _{0.5}	5.084	16.39	366.8	P6 ₃ /mmc
GdCoNiGa	5.102	16.35	368.0	P6 ₃ /mmc
GdCo _{1.5} Ni _{0.5} Ga	5.171	16.33	378.2	P6 ₃ /mmc
GdCoNi _{1.5} Ga _{0.5}	5.094	16.40	368.5	P6 ₃ /mmc
GdCo ₂ Ga	5.169	16.39	377.8	P6 ₃ /mmc
GdCo _{1.5} NiGa _{0.5}	5.098	16.40	369.2	P6 ₃ /mmc
GdCo ₂ Ni _{0.5} Ga _{0.5}	5.103	16.41	370.1	P6 ₃ /mmc

5.3.2 Magnetic Properties of GdNi_{3-x-y}Co_xGa_y phases

FC-ZFC data have been obtained for the polycrystalline samples of GdNiGa₂ and the GdNi_{3-x-y}Co_xGa_y series. The temperature dependence of the magnetic susceptibility plot for all the compounds is shown in Figure 5.3a-b. All the transition temperatures were determined at the inflection point of the FC magnetic susceptibility curve at 0.01 T. The GdNiGa₂ (Figure 5.3a) exhibits an anti-ferromagnetic (AFM) behavior with a Neel temperature of $T_N = 19.8$ K. The effective magnetic moment (μ_{eff}) obtained experimentally is $9.56 \mu_B/\text{fu}$ which larger than the theoretical values of $\mu_{\text{calc}} = 7.94 \mu_B$ for a free Gd³⁺ ion. Hence, the Ni contributes substantially to the magnetic behavior of GdNiGa₂. Negative paramagnetic Weiss constant (θ_p) of -20 K was obtained indicating dominant anti-ferromagnetic interactions in the paramagnetic region.

All the compounds in the GdNi_{3-x-y}Co_xGa_y series, however, show two successive magnetic transitions in the magnetic susceptibility curves which correspond to FM to PM transitions and FM to FM transition except for GdCo₂Ga and GdCo_{0.25}Ni_{2.5}Ga_{0.25} which exhibit only an FM to PM transition (Figure 5.3b). The major transition temperatures are listed in table 5.3. These values, however, increase with increasing Co content as shown in Table 5.3. The remaining transitions which are due to impurities (Appendix Fig. D.1 and D.2) are shown in fig. 5.3b. The effective magnetic moment per formula unit obtained using the temperature dependence of the reciprocal magnetic susceptibility curve of GdNi_{3-x-y}Co_xGa_y is listed in table 5.4.

Table 5.2. Elemental composition of GdNiGa₂ and GdNi_{3-x-y}Co_xGa_y series from Energy Dispersive X-ray Fluorescence analysis (EDXRF).

Nominal Chemical Composition	XRF Composition
GdNiGa ₂	Gd _{1.13} Ni _{1.05} Ga _{1.82}
GdCo _{0.25} Ni _{2.5} Ga _{0.25}	Gd _{1.01} Co _{0.26} Ni _{2.42} Ga _{0.31}
GdCo _{0.5} Ni ₂ Ga _{0.5}	Gd _{1.01} Co _{0.53} Ni _{2.01} Ga _{0.46}
GdCoNiGa	Gd _{1.02} Co _{1.09} Ni _{1.00} Ga _{0.88}
GdCo _{1.5} Ni _{0.5} Ga	Gd _{1.08} Co _{1.61} Ni _{0.52} Ga _{0.80}
GdCoNi _{1.5} Ga _{0.5}	Gd _{1.01} Co _{1.08} Ni _{1.45} Ga _{0.46}
GdCo ₂ Ga	Gd _{1.03} Co _{2.13} Ga _{0.84}
GdCo _{1.5} NiGa _{0.5}	Gd _{0.99} Co _{1.56} Ni _{0.99} Ga _{0.46}
GdCo ₂ Ni _{0.5} Ga _{0.5}	Gd _{0.98} Co _{2.07} Ni _{0.50} Ga _{0.46}

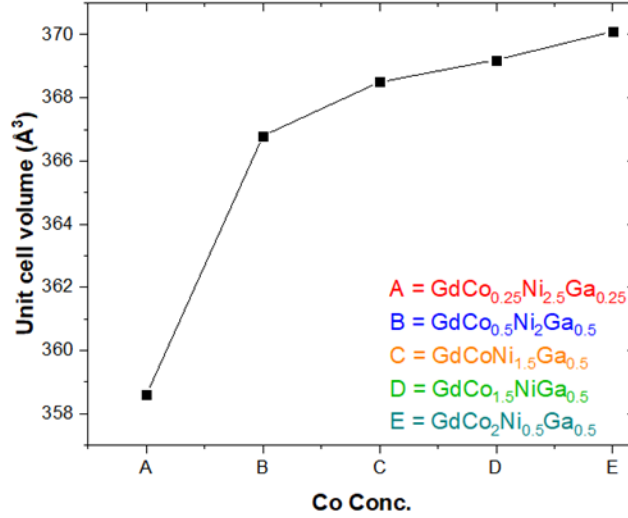


Figure 5.2. Variation of unit cell volume of the GdCo_{0.25}Ni_{2.5}Ga_{0.25}, GdCo_{0.5}Ni₂Ga_{0.5}, GdCoNi_{1.5}Ga_{0.5}, GdCo_{1.5}NiGa_{0.5} and GdCo₂Ni_{0.5}Ga_{0.5} as a function of the Co concentration.

All the effective magnetic moment values are higher than the theoretical effective moment value of 7.94 μ_B of free Gd³⁺ ion. This suggests a significant contribution from the transition metal magnetic sublattices. The paramagnetic Weiss constant for all the compounds obtained is in line with the ferromagnetic nearest-neighbor dominant interactions (Table 5.3). The values of the paramagnetic Weiss constant, however, increases with increasing Co content.

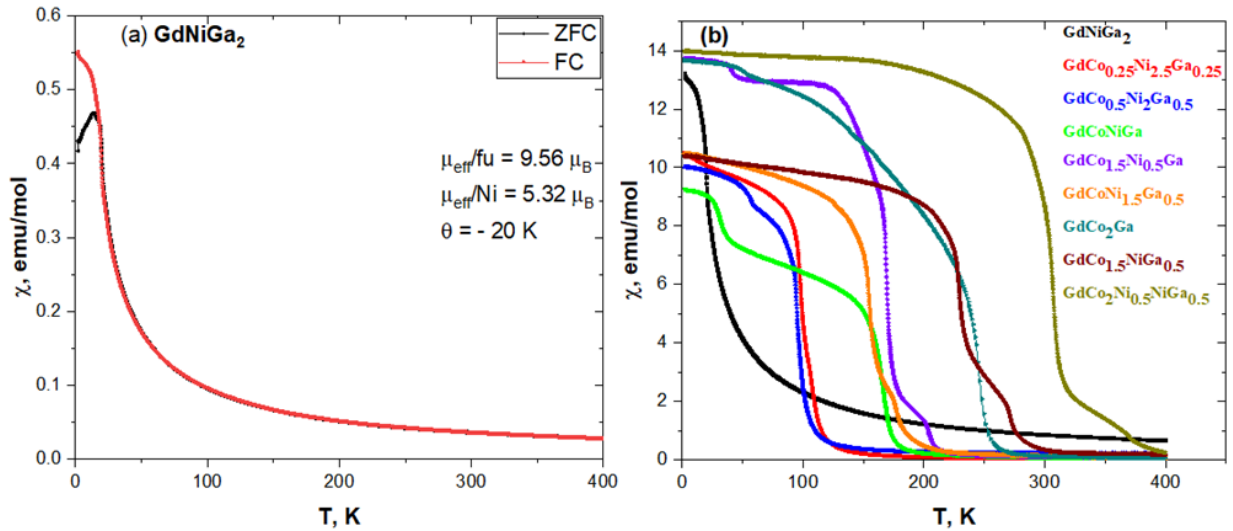


Figure 5.3. Magnetic susceptibility of (a) GdNiGa₂, (b) GdNi_{3-x-y}Co_xGa_y series, measured under the field of 0.01 T.

Table 5.3. Magnetic Properties of GdNiGa₂ and GdNi_{3-x-y}Co_xGa_y Compounds: T_c, Curie Temperature; θ , Paramagnetic Weiss Temperature.

Compound	T _c , (K)	θ , (K)
GdNiGa ₂	19.75	-20
GdCo _{0.25} Ni _{2.5} Ga _{0.25}	98.0	108
GdCo _{0.5} Ni ₂ Ga _{0.5}	94.2	93
GdCoNiGa	165.0	213
GdCo _{1.5} Ni _{0.5} Ga	169.0	132
GdCoNi _{1.5} Ga _{0.5}	154.0	177
GdCo ₂ Ga	245.0	235
GdCo _{1.5} NiGa _{0.5}	230.0	263
GdCo ₂ Ni _{0.5} Ga _{0.5}	306.0	356

Figure 5.4 depicts the field dependence of magnetization recorded at 2 K under an applied magnetic field of -7 to $+7$ T. No hysteresis was observed for all the compounds during measurements of the field-dependent magnetization. With the exception of GdNiGa₂ which shows a typical AFM (Figure 5.4a) curve with magnetization saturation (μ_{sat}) of $3.58 \mu_{\text{B}}$, the rest of the compounds (GdNi_{3-x-y}Co_xGa_y) series exhibit a ferromagnetic behavior as plotted in (Figure 5.4b). The saturation magnetization values at 2 K and 7 T exhibits a decreasing trend with increasing Co content as depicted by Figure 5.5. The values are greater (GdCo_{0.25}Ni_{2.5}Ga_{0.25}, GdCo_{0.5}Ni₂Ga_{0.5}, GdCoNiGa, GdCo_{1.5}Ni_{0.5}Ga) and lower (GdCoNi_{1.5}Ga_{0.5}, GdCo₂Ga, GdCo_{1.5}NiGa_{0.5}, GdCo₂Ni_{0.5}Ga_{0.5}) than the expected value of $\mu_{\text{sat, theo}}/\text{Gd}^{3+} = 7 \mu_{\text{B}}$ according to $gJ \times J$. The deviation of the μ_{sat} values from the ideal $7 \mu_{\text{B}}/\text{Gd}^{3+}$, suggest a large contribution from the Co spins to the overall magnetic moment. The results of magnetization measurements of the GdNi_{3-x-y}Co_xGa_y are summarized in Table 5.4.

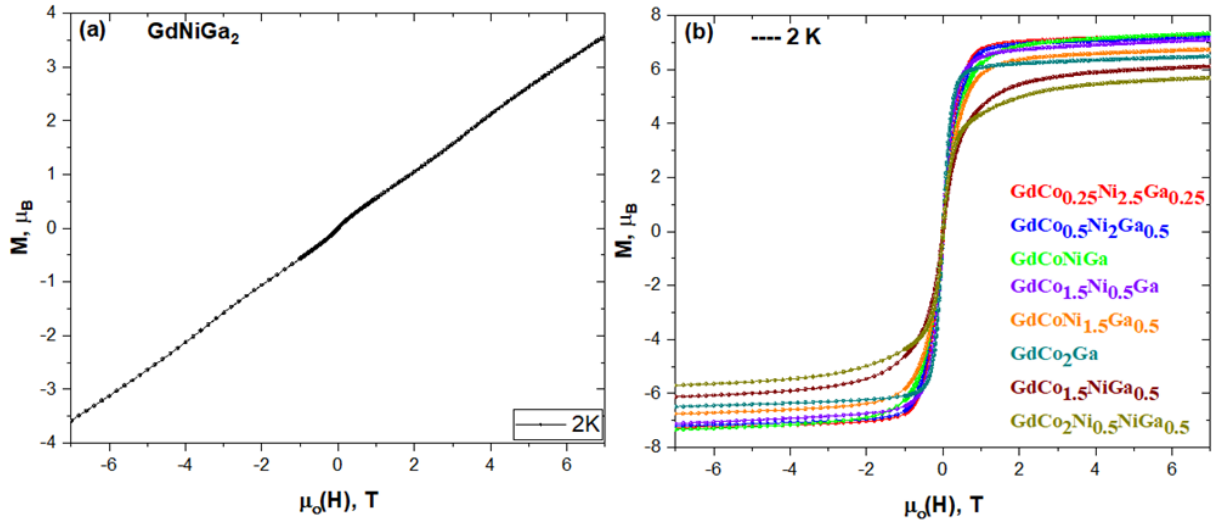


Figure 5.4. Field dependence of magnetization for (a) GdNiGa_2 and (b) $\text{GdNi}_{3-x-y}\text{Co}_x\text{Ga}_y$ at 2 K.

Table 5.4. Magnetic Properties of Compounds of $\text{GdNi}_{3-x-y}\text{Co}_x\text{Ga}_y$: μ_{eff} , Effective Magnetic Moment; μ_{sat} , Saturation Magnetization at 2 K and 7 T; T_c , Curie Temperature.

Compound	M_{eff}/μ_B	M_{sat}/μ_B	T_c (K)
$\text{GdCo}_{0.25}\text{Ni}_{2.5}\text{Ga}_{0.25}$	8.29	7.27	98.0
$\text{GdCo}_{0.5}\text{Ni}_2\text{Ga}_{0.5}$	12.01	7.20	94.2
GdCoNiGa	7.98	7.34	165.0
$\text{GdCo}_{1.5}\text{Ni}_{0.5}\text{Ga}$	12.03	7.11	169.0
$\text{GdCoNi}_{1.5}\text{Ga}_{0.5}$	10.91	6.75	154.0
GdCo_2Ga	8.19	6.49	245.0
$\text{GdCo}_{1.5}\text{NiGa}_{0.5}$	10.20	6.12	230.0
$\text{GdCo}_2\text{Ni}_{0.5}\text{Ga}_{0.5}$	9.71	5.69	306.0

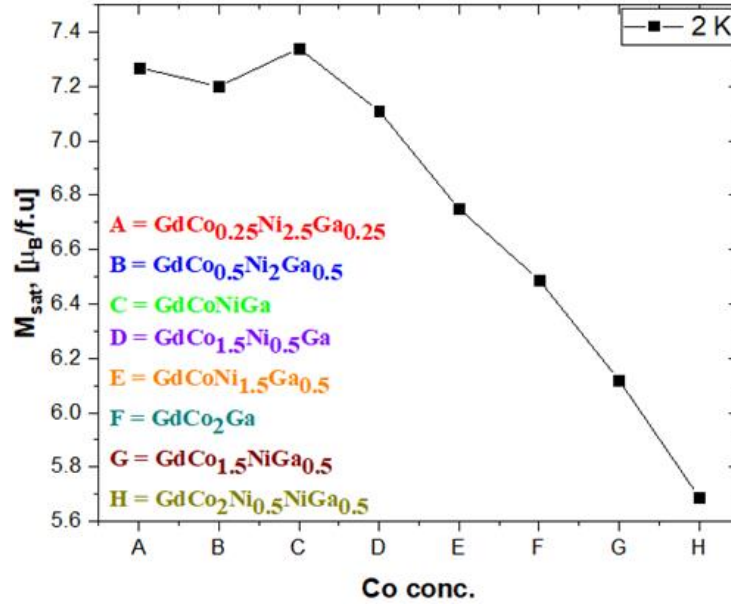


Figure 5.5. Saturation magnetic moments M_{sat} measured at 2 K for the $\text{GdNi}_{3-x-y}\text{Co}_x\text{Ga}_y$ compounds as a function of the Co concentration.

5.3.3 Magnetocaloric effect of $\text{GdNi}_{3-x-y}\text{Co}_x\text{Al}_y$ phases

The magnetocaloric properties were investigated for GdNiGa_2 and $\text{GdNi}_{3-x-y}\text{Co}_x\text{Ga}_y$ series by measuring several magnetization isotherms with increasing magnetic field at different temperatures around the vicinity of the transition temperature.

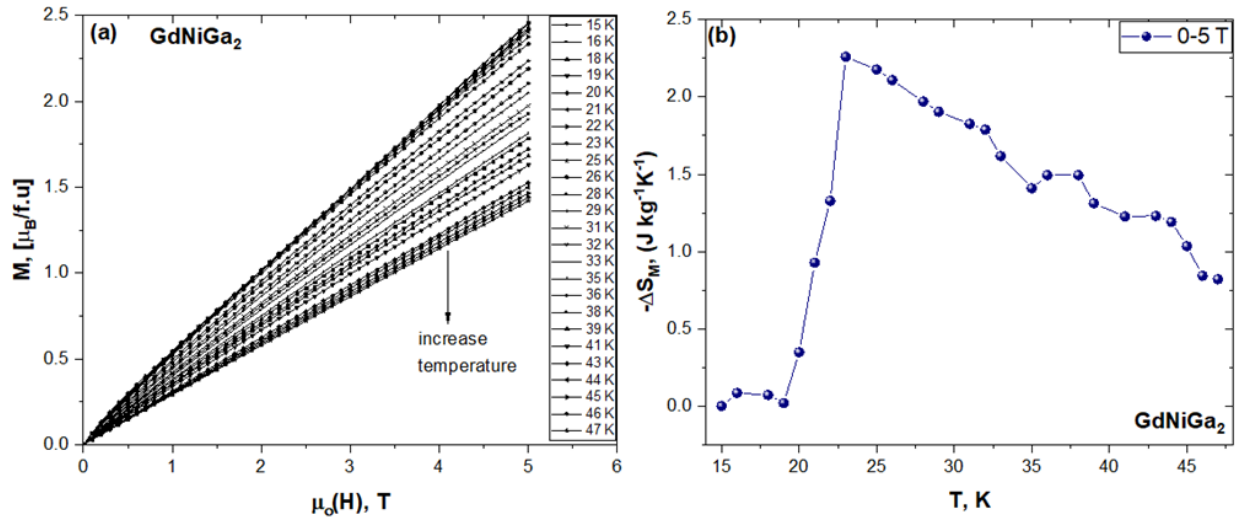


Figure 5.6. (a) Selected magnetization isotherms for GdNiGa_2 , measured between 11 and 47 K. (b) Magnetic entropy change of GdNiGa_2 for a $\Delta H = 0-2$ T.

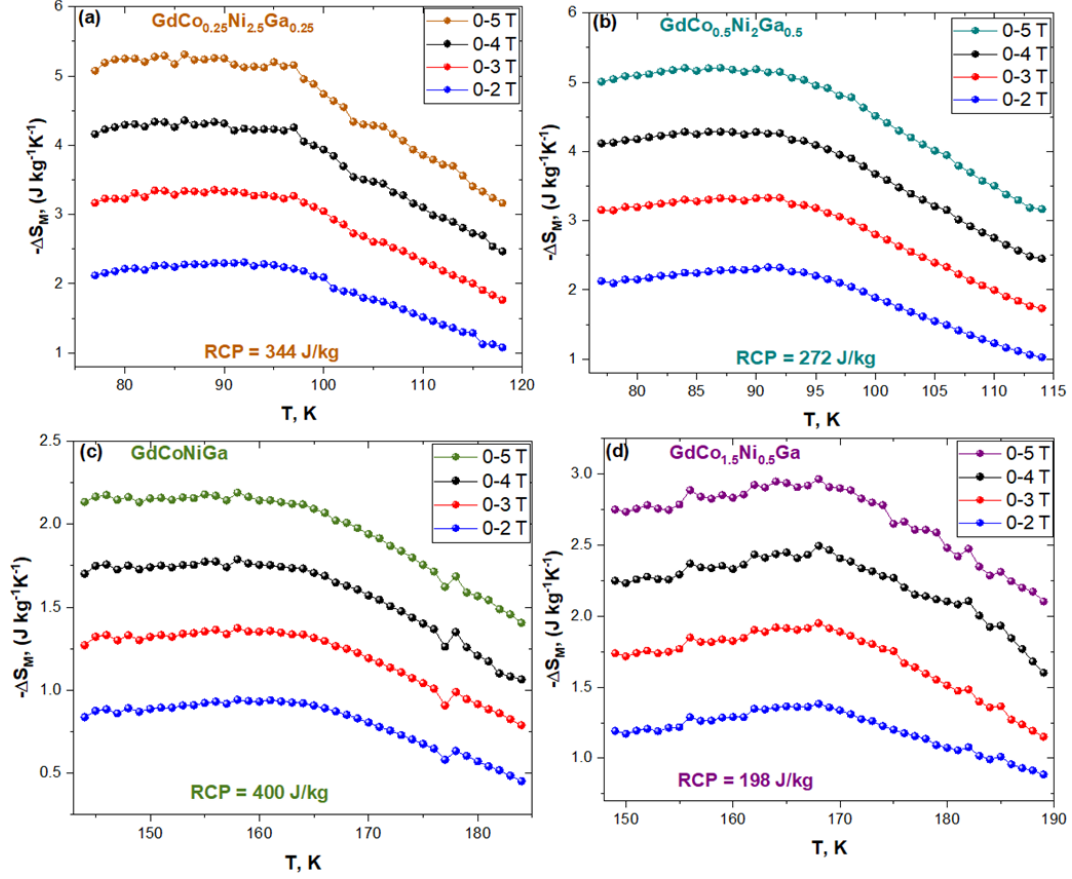


Figure 5.7. Temperature dependence of the magnetic entropy change ΔS_M of (a) $\text{GdCo}_{0.25}\text{Ni}_{2.5}\text{Ga}_{0.25}$, (b) $\text{GdCo}_{0.5}\text{Ni}_2\text{Ga}_{0.5}$, (c) GdCoNiGa (d) $\text{GdCo}_{1.5}\text{Ni}_{0.5}\text{Ga}$ compounds.

Figure 5.6 depicts selected magnetization isotherms between 15-47 K and Temperature dependence of the magnetic entropy change ΔS_M of GdNiGa_2 . The isothermal magnetization curve conforms with the AFM behavior described above. The ΔS_M values were estimated using the Maxwell thermodynamic equation: $\Delta S_M = - \int H (\partial M / \partial T) H dH$, for magnetic field changes of 0-2, 0-3, 0-4 and 0-5 T. The calculated entropy change for GdNiGa_2 reaches an of $2.25 \text{ J kg}^{-1} \text{K}^{-1}$, at 23 K. The introduction of Co leads to a change in both the structure and magnetization, as indicated above.

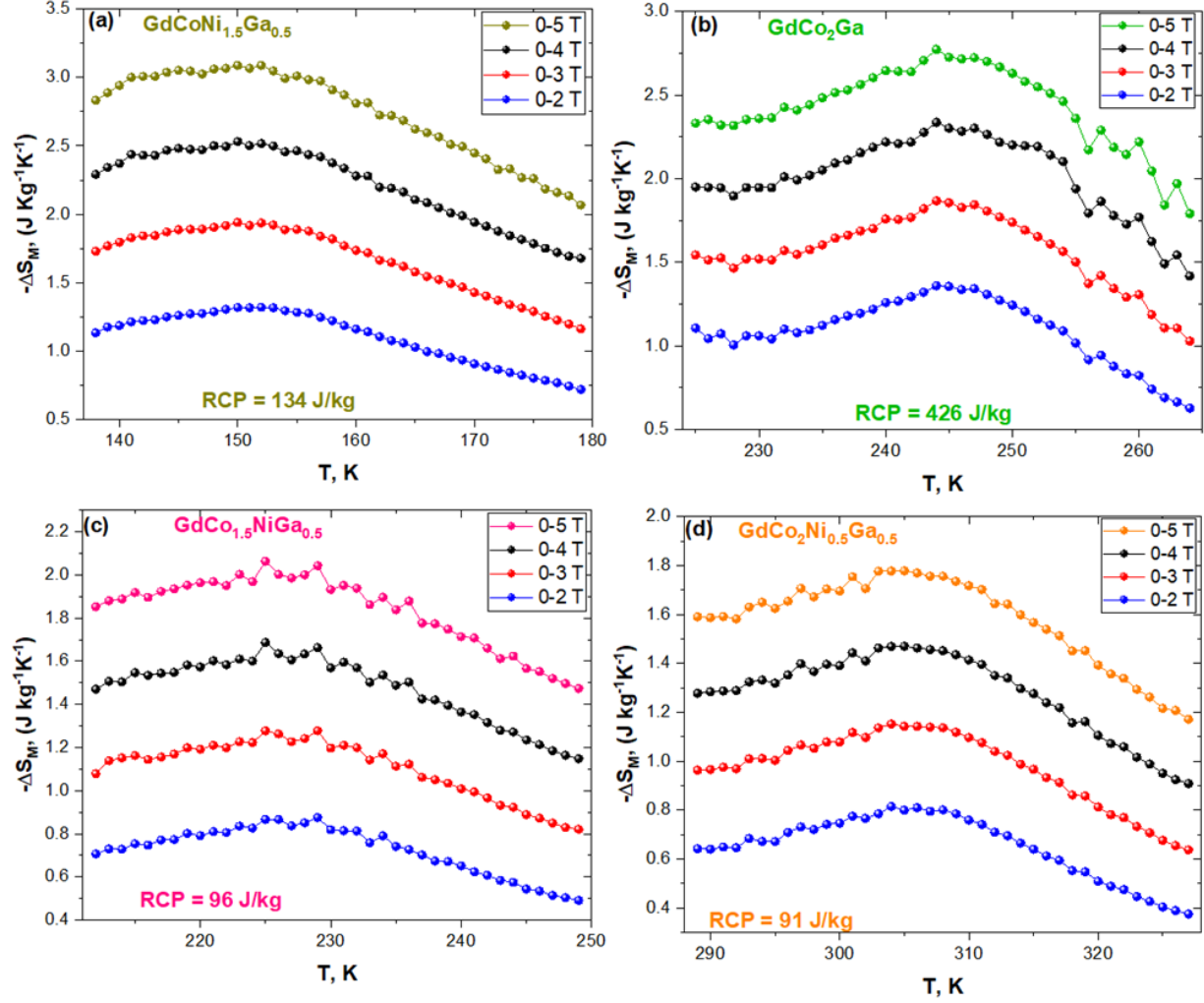


Figure 5.8. Temperature dependence of the magnetic entropy change ΔS_M of (a) $\text{GdCoNi}_{1.5}\text{Ga}_{0.5}$, (b) GdCo_2Ga , (c) $\text{GdCo}_{1.5}\text{NiGa}_{0.5}$ (d) $\text{GdCo}_2\text{Ni}_{0.5}\text{Ga}_{0.5}$ compounds.

Figure 5.7a-d and 5.8a-d shows the calculated magnetic entropy changes $-\Delta S_M$ of $\text{GdNi}_{3-x}\text{Co}_x\text{Ga}_y$ for magnetic field changes of 0-2, 0-3, 0-4 and 0-5 T. All curves at the various applied fields show a maximum of the ΔS_M near the major transition temperatures, in line with the susceptibility measurement. The extracted maximum magnetic entropy change values for field changes of ΔH 0-2, 0-3, 0-4, and 0-5 T are listed in Table 5.5. From this table, one can see a decrease in the entropy values as the Co content increases. Increasing magnetic disorder in the magnetic 3d sublattice may be responsible for this behavior. Thus, the 3d-itinerant electrons most of all contribute to the MCE in the $\text{GdNi}_{3-x}\text{Co}_x\text{Ga}_y$ series. Similar behavior was observed in the $(\text{Gd}(\text{Ni}_{1-x}\text{T}_x))_3$; $\text{T} = \text{Co}, \text{Fe}$) compounds.⁸⁵⁻⁸⁷ Figure 5.9a-b depicts the magnetic entropy dependence on the magnetization (magnetic saturation) and the unit cell volume. It is clear from Figure 5.9a

that the entropy increases with increasing saturation magnetization. This can be best explained by the Maxwell equation mentioned above, which shows a strong correlation between the entropy and the magnetization. In addition, the magnetic entropy change decreases with increasing unit cell volume (Figure 5.9b). This could be attributed to the magnetic entropy loss which is emanating from the energy required to realign the magnetic spins by the applied magnetic field due to increasing volume.

The values of the RCP calculated for $\text{GdNi}_{3-x-y}\text{Co}_x\text{Ga}_y$ series are shown below in table 5.5. These values are low compared to MCE materials like GdNiAl_2 (492 J kg^{-1}) studied in chapter 4. They are, however, compared to known MCE materials such as $\text{Gd}_5\text{Si}_2\text{Ge}_2$ (440 J kg^{-1}).

Table 5.5. Maximum of the Magnetic Entropy Change at various applied magnetic fields, the RCP, Relative Cooling Powder calculated at 0-5 T.

Compound	$-\Delta S_M (\text{J kg}^{-1} \text{K}^{-1})$				RCP(Jkg^{-1})
	$\Delta H =$	0-2 T	0-3 T	0-4 T	0-5 T
GdNiGa_2					2.25
$\text{GdCo}_{0.25}\text{Ni}_{2.5}\text{Ga}_{0.25}$		2.29	3.34	4.34	5.31
$\text{GdCo}_{0.5}\text{Ni}_2\text{Ga}_{0.5}$		2.28	3.32	4.29	5.21
GdCoNiGa		0.94	1.37	1.78	2.19
$\text{GdCo}_{1.5}\text{Ni}_{0.5}\text{Ga}$		1.38	1.95	2.49	2.96
$\text{GdCoNi}_{1.5}\text{Ga}_{0.5}$		1.31	1.94	2.53	3.09
GdCo_2Ga		1.36	1.87	2.34	2.77
$\text{GdCo}_{1.5}\text{NiGa}_{0.5}$		0.87	1.28	1.69	2.06
$\text{GdCo}_2\text{Ni}_{0.5}\text{Ga}_{0.5}$		0.80	1.14	1.47	1.78

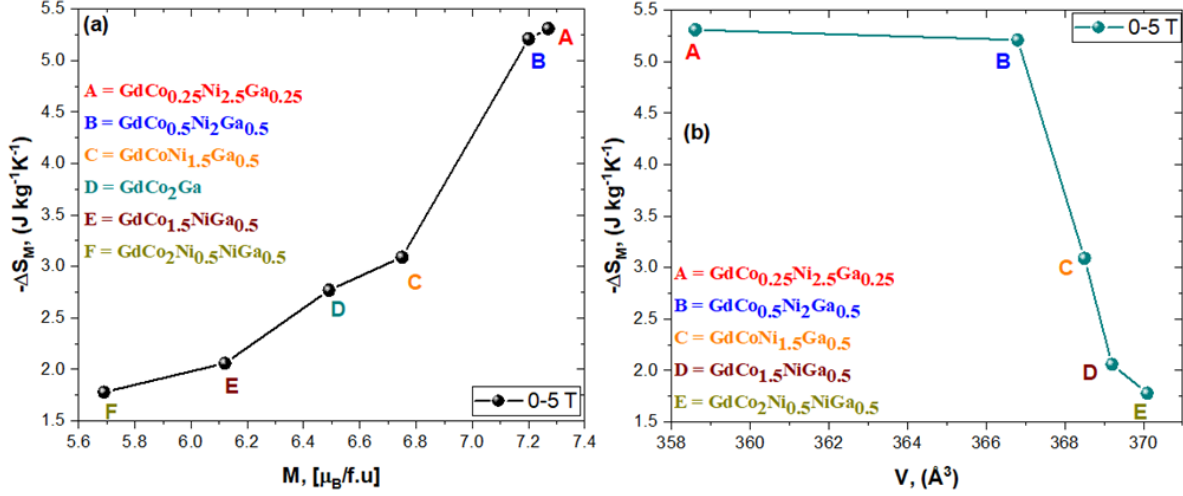


Figure 5.9. The change of magnetocaloric effect at 0-5 T versus (a) saturation magnetization at 2 K and (b) the volume of the unit cell, for some selected phases.

5.4 Conclusion

In this chapter, we have demonstrated that replacing Al with Ga in $(\text{GdNi}_{3-x-y}\text{Co}_x\text{Al}_y)$ with different metallic radius ($\text{Al} = 1.43 \text{ \AA}$, $\text{Ga} = 1.35 \text{ \AA}$) leads to a drastic modification of the unit cell volume, magnetic and magnetocaloric properties, attributed to the local environment of Gd and (Co/Ni). As expected for the $\text{GdNi}_{3-x-y}\text{Co}_x\text{Ga}_y$ series, the unit cell volumes increase almost linearly from $\text{GdCo}_{0.25}\text{Ni}_{2.5}\text{Ga}_{0.25}$ to $\text{GdCo}_2\text{Ni}_{0.5}\text{Ga}_{0.5}$ compounds, attributed to the larger size of Co. As reported for the first time in this work, the GdNiGa_2 orders antiferromagnetically with $T_N = 19.75 \text{ K}$. In the series $\text{GdNi}_{3-x-y}\text{Co}_x\text{Ga}_y$, a linear (almost) increase of the ferromagnetic ordering temperatures with increasing Co content is observed. Upon investigation of the magnetocaloric properties, a maximum magnetic entropy change of $-\Delta S_M^{\text{max}} = 2.25, 5.31, 5.21, 2.19, 2.96, 3.09, 2.77, 2.06$ and $1.78 \text{ J kg}^{-1} \text{ K}^{-1}$ for the field changes of $\Delta H = 5 \text{ T}$ for GdNiGa_2 , $\text{GdCo}_{0.25}\text{Ni}_{2.5}\text{Ga}_{0.25}$, $\text{GdCo}_{0.5}\text{Ni}_2\text{Ga}_{0.5}$, GdCoNiGa , $\text{GdCo}_{1.5}\text{Ni}_{0.5}\text{Ga}$, $\text{GdCoNi}_{1.5}\text{Ga}_{0.5}$, GdCo_2Ga , $\text{GdCo}_{1.5}\text{NiGa}_{0.5}$, and $\text{GdCo}_2\text{Ni}_{0.5}\text{NiGa}_{0.5}$ respectively was observed. The decrease in entropy value of the $\text{GdNi}_{3-x-y}\text{Co}_x\text{Ga}_y$ series can be attributed to the reduced saturation magnetization and increasing volume of the unit cell observed in the $M(H)$ and volume-dependent curves, respectively. The RCP values are low compared to MCE materials like GdNiAl_2 (492 J kg^{-1}) studied in chapter 4 and are, however, compared to know MCE materials such as $\text{Gd}_5\text{Si}_2\text{Ge}_2$ (440 J kg^{-1}).

5.5 References

1. M. H. Phan, S.C. Yu, Review of the magnetocaloric effect in manganite materials, *J. Magn. Mater.* 308 (2007) 325.
2. A. M. Tishin, Y.I. Spichkin, *The Magnetocaloric Effect and its Applications*, Institute of Physics Publishing Ltd., Bristol, 2003.
3. M. Quintero, J. Sacanell, L. Ghivelder, A.M. Gomes, A.G. Leyva, F. Parisi, Magnetocaloric effect in manganites: metamagnetic transitions for magnetic Refrigeration, *Appl. Phys. Lett.* 97 (2010) 121916(1)-121916(3).
4. M. Balli, P. Fournier, S. Jandl, M.M. Gospodinov, A study of the phase transition and magnetocaloric effect in multiferroic $\text{La}_2\text{MnNiO}_6$ single crystals, *J. Appl. Phys.* 115 (2014) 173904(1)-173904(8).
5. J. Glanz, Making a bigger chill with magnets, *Science* 27 (1998) 2045.
6. V.K. Pecharsky, K.A. Gschneider Jr., Magnetocaloric effect and magnetic refrigeration, *J. Magn. Mater.* 200 (1999) 44.
7. O. Tegus, E. Brück, K.H.J. Buschow, F.R. de Boer, Transition-metal-based magnetic refrigerants for room-temperature applications, *Nature* 415 (2002) 150.
8. K.A. Gschneider, V.K. Pecharsky, A.O. Tsokol, Recent developments in magnetocaloric materials, *Rep. Prog. Phys.* 68 (2005) 1479.
9. E. Brück, Topical review e developments in magnetocaloric refrigeration, *J. Phys. D. Appl. Phys.* 38 (2005) R381.
10. N. A. de Oliveira, P.J. von Ranke, Theoretical aspects of the magnetocaloric effect, *Phys. Rep.* 489 (2010) 89.
11. V. K. Pecharsky, K. A. Gschneider Jr., Giant magnetocaloric effect in $\text{Gd}_5(\text{Si}_2\text{Ge}_2)$, *Phys. Rev. Lett.* 78 (1997) 4494.
12. Q. Luo, W.H. Wang, Rare earth based bulk metallic glasses, *J. Non-Crystall. Solids* 355 (2009) 759–777.
13. [2] H. Fu, M. Zou, Magnetic and magnetocaloric properties of ternary Gd–Co–Al bulk metallic glasses, *J. Alloys Compd.* 509 (2011) 4613–4616.
14. S. Lu, M.B. Tang, L. Xia, Excellent magnetocaloric effect of a $\text{Gd}_{55}\text{Al}_{20}\text{Co}_{25}$ bulk metallic glass, *Physica B* 406 (2011) 3398–3401.
15. C. Mayer, S. Gorsse, G. Ballon, R. Caballero-Flores, V. Franco, B. Chevalier, Tunable magnetocaloric effect in Gd-based glassy ribbons, *J. Appl. Phys.* 110 (2011) 053920.

16. D. Ding, M.B. Tang, L. Xia, Excellent glass forming ability and refrigeration capacity of a $\text{Gd}_{55}\text{Al}_{18}\text{Ni}_{25}\text{Sn}_2$ bulk metallic glass, *J. Alloys Compd.* 581 (2013) 828–831.
17. V. K. Pecharsky, K. A. Gschneidner Jr., Magnetocaloric effect and magnetic refrigeration. *J. Magn. Magn. Mater.* 1999, 200, 44–56.
18. V. K. Pecharsky, K. A. Gschneidner Jr., Comparison of the magnetocaloric effect derived from heat capacity, direct and magnetization measurements. *Adv. Cryog. Eng.* 1996, 42, 423–430.
19. V. K. Pecharsky, K. A. Gschneidner Jr., Giant Magnetocaloric Effect in $\text{Gd}_5\text{Si}_2\text{Ge}_2$. *Phys. Rev. Lett.* 1997, 78, 4494–4497.
20. J. Liu, T. Gottschall, K. P. Skokov, J. D. Moore, and O. Gutfleisch, “Giant magnetocaloric effect driven by structural transitions,” *Nat. Mater.* 11, 620–626 (2012).
21. A. Giguère and M. Foldeaki, “Direct measurement of the “giant” adiabatic temperature change in $\text{Gd}_5\text{Si}_2\text{Ge}_2$,” *Phys. Rev. Lett.* 83, 2262 (1999)
22. X. X. Zhang, G. H. Wen, F. W. Wang, W. H. Wang, C. H. Yu, and G. H. Wu, “Magnetic entropy change in Fe-based compound $\text{LaFe}_{10.6}\text{Si}_{2.4}$,” *Appl. Phys. Lett.* 77, 3072–3074 (2000).
23. H. Wada and Y. Tanabe, “Giant magnetocaloric effect of $\text{MnAs}_{1-x}\text{Sbx}$,” *Appl. Phys. Lett.* 79, 3302–3304 (2001).
24. H. Yibole, F. Guillou, L. Zhang, N. H. van Dijk, and E. Bruck, “Direct measurement of the magnetocaloric effect in $\text{MnFe}(\text{P},\text{X})$ ($\text{X}=\text{As}, \text{Ge}, \text{Si}$) materials,” *J. Phys. D Appl. Phys.* 47, 075002 (2014).
25. B. G. Shen, J. R. Sun, F. X. Hu, H. W. Zhang, and Z. H. Cheng, “Recent progress in exploring magnetocaloric materials,” *Adv. Mater.* 21, 4545–4564 (2009).
26. F. X. Hu, B. G. Shen, J. R. Sun, Z. H. Cheng, G. H. Rao, and X. X. Zhang, “Influence of negative lattice expansion and metamagnetic transition on magnetic entropy change in the compound $\text{LaFe}_{11.4}\text{Si}_{1.6}$,” *Appl. Phys. Lett.* 78, 3675–3677 (2001).
27. Y. L. Yi, L. W. Li, K. P. Su, Y. Qi, and D. X. Huo, “Large magnetocaloric effect in a wide temperature range induced by two successive magnetic phase transitions in $\text{Ho}_2\text{Cu}_2\text{Cd}$ compound,” *Intermetallics* 80, 22–25 (2017).
28. Y. Zhang, X. Xu, Y. Yang, L. Hou, Z. Ren, X. Li, and G. Wilde, “Study of the magnetic phase transitions and magnetocaloric effect in $\text{Dy}_2\text{Cu}_2\text{In}$ compound,” *J. Alloys Compd.* 667, 130–133 (2016).
29. F. Wang, F. Y. Yuan, J. Z. Wang, T. F. Feng, and G. Q. Hu, “Conventional and inverse magnetocaloric effect in Pr_2CuSi_3 and Gd_2CuSi_3 compounds,” *J. Alloys Compd.* 592, 63–66 (2014).

30. M. V. de Souza, J. A. da Silva, and L. S. Silva, "Analyses of TmAl_2 and ErAl_2 composite for use as an active magnetic regenerator close to liquid helium temperature," *J. Magn. Mater.* 433, 248–253 (2017).
31. A. Giguere, M. Foldeaki, W. Schnelle, and E. Gmelin, "Metamagnetic transition and magnetocaloric effect in ErCo_2 ," *J. Phys. Condens. Matter.* 11, 6969–6981 (1999).
32. T. Samanta, I. Das, and S. Banerjee, "Magnetocaloric effect in Ho_5Pd_2 : Evidence of large cooling power," *Appl. Phys. Lett.* 91, 082511 (2007).
33. B. Li, J. Du, W. J. Ren, W. J. Hu, Q. Zhang, D. Li, and Z. D. Zhang, "Large reversible magnetocaloric effect in Tb_3Co compound," *Appl. Phys. Lett.* 92, 242504 (2008).
34. Y. Zhang, B. Yang, and G. Wilde, "Magnetic properties and magnetocaloric effect in ternary REAgAl ($\text{RE}=\text{Er}$ and Ho) intermetallic compounds," *J. Alloys Compd.* 619, 12–15 (2015).
35. S. Gupta and K. G. Suresh, "Variations of magnetocaloric effect and magnetoresistance across RCuGe ($\text{R}=\text{Tb}$, Dy , Ho , Er) compounds," *J. Magn. Mater.* 391, 151–155 (2015).
36. J. Chen, B. G. Shen, Q. Y. Dong, F. X. Hu, and J. R. Sun, "Giant reversible magnetocaloric effect in metamagnetic HoCuSi compound," *Appl. Phys. Lett.* 96, 152501 (2010).
37. L. Li, Y. Yuan, Y. Zhang, T. Namiki, K. Nishimura, R. Poettgen, and S. Zhou, "Giant low field magnetocaloric effect and field-induced metamagnetic transition in TmZn ," *Appl. Phys. Lett.* 107, 132401 (2015).
38. S. B. Gupta and K. G. Suresh, "Giant low field magnetocaloric effect in soft ferromagnetic ErRuSi ," *Appl. Phys. Lett.* 102, 022408 (2013).
39. K. A. Gschneidner Jr, V. K. Pecharsky, A. O. Pecharsky, C. B. Zimm, Recent Developments in Magnetic Refrigeration. *Mater. Sci. Forum* 1999, 315-317, 69-76.
40. M. E. Wood, W. H. Potter, General analysis of magnetic refrigeration and its optimization using a new concept: maximization of refrigerant capacity. *Cryogenics* 1985, 25, 667-683.
41. G. Bruzzone, M. Ferretti, F. Merlo, G. L. Olcese, Structural, magnetic and hydrogenation properties of RNiAl_2 ternary compounds. *Lanthanide Actinide Res.* 1986, 1, 153-161.
42. R. E. Gladyshevskii, E. Parthé, Crystal structure of scandium nickel dialuminium, ScNiAl_2 with MgCuAl_2 type. *Z. Kristallogr.* 1992, 198, 291-292.
43. R. E. Gladyshevskii, E. Z. Parthé, *Kristallogr. Cryst. Mater.* 1993, 203, 349-351.
44. C. Tang, Y. Du, H. H. Xu, W. Xiong, L. J. Zhang, F. Zheng, H. Y. Zhou, *Intermetallics* 2008, 16, 432-439.

45. S. N. Dembele, Z. Ma, Y. F. Shang, H. Fu, E. A. Balfour, R. L. Hadimani, D. C. Jiles, B. H. Teng, Y. J. Luo, *Magn. Magn. Mater.* 2015, 391, 191-194.
46. R. Pöttgen, T. Gulden, A. Simon, Miniaturisierte Lichtbogenapparat für den Laborbedarf. *GIT Labor-Fachzeitschrift* 1999, 43, 133–136.
47. K. Yvon, W. Jeitschko, E. Parthé, LAZY PULVERIX, a computer program, for calculating X-ray and neutron diffraction powder patterns. *J. Appl. Crystallogr.* 1977, 10, 73-74.
48. L. J. A. van der Pauw, method of measuring the resistivity and hall coefficient on discs of arbitrary shape. *Philips Res. Repts.* 1958, 13, 1-9.
49. H. Perltz, A. Westgren, The Crystal Structure of Al_2CuMg . *Ark. Kemi Mineral. Geol.* 1943, 16B, 1-5.
50. Yu. P. Yarmolyuk, Yu. Grin, Intermetallic compounds RGa_2Ni and RGa_4Ni in (Y, Sm, Gd, Tb, Dy, Ho, Er, Tm, Yb, Lu)-Ga-Ni system. *Russ. Metall.* 1981, 5, 179-183.
51. V. Y. Markiv, N. Belyavina, New representatives of YbCd_6 and MgCuAl_2 structure types. *Dopov. Akad. Nauk Ukr. RSR, Ser. B* 1983, 12, 30–33.
52. V. V. Romaka, Yu. Grin, Yu. P. Yarmolyuk, R. V. Skolozdra, A. A. Yartys', Magnetic and crystallographic characteristics of compounds RNiGa_2 (R - rare-earth metal). *Ukr. Fiz. Zh. Russ. Ed.* 1983, 28, 227–230.
53. K. Dasculidou-Gritner, H.U. Schuster, Darstellung und Struktur von CaPtGa_2 . *Z. Naturforsch. B: J. Chem. Sci.* 1993, 48b, 844–846.
54. L. O. Vasilechko, Yu. Grin, Yu. P. Yarmolyuk, *Russ. Metall.* 1995, 1, 155-159.
55. Y. Grin, K. Hiebl, P. Rogl, C. Godart, *J. Alloys Compd.* 1996, 239, 127-130.
56. O. Sichevych, Yu. Prots, W. Schnelle, Y. Grin, *Z. Kristallogr. – New Cryst. Struct.* 2011, 226, 439–440.
57. L. Vasylechko, U. Burkhardt, W. Schnelle, H. Borrmann, F. Haarmann, A. Senyshyn, D. Trots, K. Hiebl, Y. Grin, *Solid State Sci.* 2012, 14, 746–760.
58. Yu. V. Verbovytsky, *Chem. Met. Alloys.* 2014, 7, 42–55.
59. V. I. Zaremba, O. Y. Zaremba, Yu. M. Kalychak, O. I. Bodak, *Dopov. Akad. Nauk Ukr. RSR, Ser. B* 1987, 12, 44–46.
60. U. K. Zachwieja, *Z. Anorg. Allg. Chem.* 1995, 621, 1677-1680.
61. Y. Ijiri, F. J. DiSalvo, H. Yamane, *J. Solid State Chem.* 1996, 122, 143-147.
62. Yu. M. Kalychak, Y. V. Galadzhun, J. Stepien-Damm, *Z. Kristallogr. New Cryst. Struct.* 1997, 212, 929.

63. R. D. Hoffmann, U. Ch. Rodewald, R. Z. Pöttgen, B. Naturforsch, J. Chem. Sci. 1999, 54b, 38–44.
64. Yu. V. Galadzhun, R. D. Hoffmann, G. Kotzyba, B. Künnen, R. Pöttgen, Eur. J. Inorg. Chem. 1999, 1999, 975–979.
65. R. D. Hoffmann, R. Pöttgen, G. A. Landrum, R. Dronskowski, B. Künnen, G. Kotzyba, Z. Anorg. Allg. Chem. 1999, 625, 789–798.
66. R. D. Hoffmann, R. Pöttgen, V. I. Zaremba, Yu. M. Z. Kalychak, B. Naturforsch, J. Chem. Sci. 2000, 55b, 834–840.
67. R. D. Hoffmann, R. Pöttgen, Chem. - Eur. J. 2001, 7, 382–387.
68. R. Pöttgen, D. Kußmann, Z. Anorg. Allg. Chem. 2001, 627, 55–60.
69. V. I. Zaremba, V. P. Dubenskiy, R. Z. Pöttgena, B. Naturforsch, J. Chem. Sci. 2002, 57b, 798–802.
70. M. Giovannini, A. Saccone, P. Rogl, R. Ferro, Intermetallics 2003, 11, 197–205.
71. V. I. Zaremba, D. Kaczorowski, U. Ch. Rodewald, R. D. Hoffmann, R. Pöttgen, Chem. Mater. 2004, 16, 466–476.
72. V. Hlukhyy, V. I. Zaremba, Y. M. Kalychak, R. Pöttgen, J. Solid State Chem. 2004, 177, 1359–1364.
73. V. I. Zaremba, I. R. Muts, U. Ch. Rodewald, V. Hlukhyy, R. Pöttgen, Z. Anorg. Allg. Chem. 2004, 630, 1903–1907.
74. J. F. Riecken, R. Pöttgen, Structure Refinement of BaIrIn₂. Z. Naturforsch. B: J. Chem. Sci. 2005, 60b, 118–120.
75. E. V. Murashova, A. I. Tursina, Z. M. Kurenbaeva, A. V. Gribov, Y. D. Seropegin, J. Alloys Compd. 2008, 454, 206–209.
76. I. R. Muts, L. V. Sysa, Yu. V. Galadzhun, V. I. Zaremba, Yu. M. Kalychak, Visn. Lviv. Derzh. Univ., Ser. Khim. 2011, 52, 27–32.
77. A. C. Malingowski, M. Kim, J. Liu, L. Wu, M. C. Aronson, P. G. Khalifah, J. Solid State Chem. 2013, 198, 308–315.
78. S. Liu, J. D. Corbett, Synthesis, Structure, and Properties of the New Intermetallic Compounds SrPdTi₂ and SrPtTi₂. Inorg. Chem. 2003, 42, 4898–4901.
79. R. Kraft, R. Pöttgen, Die ternären Thallide REMgTi (RE=Y, La–Nd, Sm) und EuPdTi₂. Z. Anorg. Allg. Chem. 2004, 630, 1738–1738.

80. R. Kraft, S. Rayaprol, C. P. Sebastian, R. Z. Pöttgen, B. Naturforsch. J. Chem. Sci. 2006, 61b, 159-163.
81. H. Perlitz, A. Westgren, Ark. Kemi, Miner. Geol. 16b, 1 (1943).
82. B. Heying, R.-D. Hoffmann, R. Pöttgen, Z. Naturforsch. 60b, 491 (2005).
83. J. W. Xu, X. Q. Zheng, S. X. Yang, S. H. Shao, J. Q. Liu, J. Y. Zhang, S. G. Wang, Z. Y. Xu, L. C. Wang, S. Zhang, Z. Q. Zhang, and B. G. Shen, J. Appl. Phys. **125**, 225102 (2019)
84. Y. Zhang, D. Guo, Y. Yang, J Wang, S. Geng, X Li, Z. Ren, G Wilde, Intermetallics 88 (2017) 61-64.
85. A. Chrobak, A. Bajorek, G. Chełkowska, G. Haneczok, M. Kwiecien', Phys. Status Solidi (a) 206 (2009) 731.
86. A. Bajorek, A. Chrobak, G. Chełkowska, M. Kwiecien-Grudziecka, Journal of Alloys and Compounds 494 (2010) 22-27
87. A. Bajorek, A. Chrobak, G. Chełkowska, M. Kwiecien-Grudziecka, Journal of Alloys and Compounds 485 (2009) 6-12
88. Epsilon Software, Version 2.1(8.55), 3/18/2019, Malvern PANalytical B.V., Almelo, The Netherlands, 2019.
89. Epsilon Dashboard, Version 2.1.1.10717, 3/18/2019, Malvern PANalytical B.V., Almelo, The Netherlands, 2019.

CHAPTER 6. CONCLUSIONS AND FUTURE WORK

The goal of this dissertation was to reveal the effect of valence electron perturbation at the Fermi level on the structural, magnetic, magnetocaloric, and transport properties of selected rare-earth transition metal-based intermetallic systems. To achieve this goal, we have carried out the synthesis of R-T-Al ($R = \text{Gd, Tb, Dy, Ho}$; $T = \text{Cr, Zn}$), $\text{GdNi}_{3-x-y}\text{Co}_x\text{Al}_y$ and $\text{GdNi}_{3-x-y}\text{Co}_x\text{Ga}_y$ and established correlations between their crystal structures, magnetocaloric, transport and magnetic properties. Previously studied RTAl ($R = \text{Gd, Tb, Dy, Ho}$; $T = \text{Cu, Ni, Co, Fe, Mn}$) shows the interdependence of the structural and magnetic properties on the valence electron concentration (VEC) of the transition metals at the Fermi level. Particularly, the studies saw an increase in transition temperature from 82 K of GdCuAl to 274 K of GdMnAl and are attributed to the decrease in the VEC from Cu to Mn. We, therefore, hypothesized that further decrease in the VEC in Cr at the Fermi level would lead to an increase in the transition temperature in GdCrAl.

The study of $\text{RCr}_x\text{Al}_{2-x}$ and RZnAl phases in Chapters 2 and 3 indeed revealed diverse magnetic, magnetocaloric, and transport behavior of these systems, in contrast to the simple magnetic behavior of the other transition metal analogs. While the former adopts the MgCu_2 cubic structure and exhibits a ferromagnetic transition at (16, 110, 190 and 271 K for Ho, Dy, Tb, and Gd), the latter crystallizes into the MgZn_2 hexagonal phase with a Curie temperature of (20, 105, 130 and 131 K for Ho, Dy, Tb, and Gd). The difference in their properties is attributed to the decrease in the valence electron concentration from Zn to Cr at the Fermi level. Although we have not been stoichiometrically synthesized the equimolar amount of Gd-Cr-Al, we established that substituting the larger Cr in GdTAl ($T = \text{Cu, Ni, Co, Fe, Mn}$) leads to an increase in the ferromagnetic transition temperature. Thus, in the series GdTAl ($T = \text{Zn, Cu, Ni, Co, Fe, Mn, Cr}$) and $\text{GdCr}_{0.4}\text{Al}_{1.6}$, the transition temperature increased from 131 K for GdZnAl to 271 K for $\text{GdCr}_{0.4}\text{Al}_{1.6}$. The magnetocaloric effect in terms of the isothermal magnetic entropy change, ΔS_M , was studied for $\text{RCr}_x\text{Al}_{2-x}$ and RZnAl and compared to the other transition metal congeners. We observed a decrease in the magnetic entropy value from 20.5 for GdZnAl to 0.3 for $\text{GdCr}_{0.45}\text{Al}_{1.55}$, characterized by the increase in cell volume from GdZnAl (123.433 \AA^3) to $\text{GdCr}_{0.45}\text{Al}_{1.55}$ (490.365 \AA^3).

Realizing that the changes in the VEC at the Fermi level dictate the observed changes in the magnetocaloric and magnetic behavior, we investigated the substitution of Co for Ni/Al in the

structure of GdNiAl_2 , keeping in mind that substituting Co for Ni particularly will lead to a decrease in the VEC hence increasing the transition temperature. GdNiAl_2 is a known MCE material which exhibits an isothermal magnetic entropy change of $\Delta S_M = 16.0 \text{ J kg}^{-1} \text{ K}^{-1}$ at $T_C = 28 \text{ K}$ under a magnetic field change of 0-5 T. However, the low T_C limits its application as a room temperature refrigerant. In Chapter 4, we described the study of $\text{GdNi}_{1-x}\text{Co}_x\text{Al}_2$ ($x = 0.5, 0.75, 1$) and $\text{GdNi}_{3-x-y}\text{Co}_x\text{Al}_y$ solid solutions, which revealed that these materials are characterized by a structural change from $\text{GdNi}_{1-x}\text{Co}_x\text{Al}_2$ (Cmcm, orthorhombic) to $\text{GdNi}_{3-x-y}\text{Co}_x\text{Al}_y$ (P6₃/mmc, hexagonal). We have observed an increase in the ferromagnetic transition temperature from 32 K of GdNiAl_2 to 306 K of $\text{GdCo}_2\text{Ni}_{0.5}\text{Al}_{0.5}$. Such an increase in transition temperature with Co content further supports our argument that decreasing VEC at the Fermi level can lead to an increase in transition temperature. Unfortunately, the increase in the Co content leads to a decrease in the magnetic entropy change from $15.8 \text{ J kg}^{-1} \text{ K}^{-1}$ in GdNiAl_2 to $1.8 \text{ J kg}^{-1} \text{ K}^{-1}$ in $\text{GdCo}_2\text{Ni}_{0.5}\text{Al}_{0.5}$ for a field change of 0-5 T. This behavior is to (i) the change in structure from Cmcm to P6₃/mmc; (ii) reduced saturation magnetization value from 7.7 to $5.6 \mu_B/\text{f.u}$ for GdNiAl_2 and $\text{GdCo}_2\text{Ni}_{0.5}\text{Al}_{0.5}$ respectively (iii) increase in unit cell volume from GdNiAl_2 (286.7 \AA^3) to $\text{GdCo}_2\text{Ni}_{0.5}\text{Al}_{0.5}$ (414.6 \AA^3).

The studies in chapter 5 describe the extension of our studies to the Ga (GdNiGa_2 and $\text{GdCo}_x\text{Ni}_{3-x-y}\text{Ga}_y$) analogs of GdNiAl_2 and $\text{GdCo}_x\text{Ni}_{3-x-y}\text{Al}_y$. Interestingly, these structural modifications have a pronounced effect on the magnetic behavior. The Ga analogs exhibit complex magnetic behavior characterized by complex (multiple) magnetic transitions, as opposed to the rather simple magnetism of their Al congeners. While the GdNiAl_2 exhibit a ferromagnetic behavior with a transition temperature of 32 K, the GdNiGa_2 analog is antiferromagnetic with an ordering temperature of 19.8 K. Except for GdNiGa_2 , the $\text{GdNi}_{3-x-y}\text{Co}_x\text{Ga}_y$ solid solution, have a higher ordering temperature compared to their Al analogs. For example, GdCoNiGa and GdCo_2Ga are FM with $T_C = 165$ and 245 K respectively, in contrast, 102 and 188 K respectively for GdCoNiAl and GdCo_2Al . We have also established that substituting Ga for Al leads to a decrease in the unit cell volume characterized by smaller metallic radius ($r_{\text{Ga}} = 1.35 \text{ \AA}$) compared Al ($r_{\text{Al}} = 1.43 \text{ \AA}$). Though the unit cell volume of Ga containing series are smaller compared to the Al analogs, for which we expect a relatively larger magnetic entropy change, their entropies turns out to be much smaller. For example, GdNiGa_2 , $\text{GdCo}_{0.25}\text{Ni}_{2.5}\text{Ga}_{0.25}$ and GdCo_2Ga , has an entropy at 0-5 T to be 2.25, 5.31 and $1.78 \text{ J kg}^{-1} \text{ K}^{-1}$ as oppose to 15.8, 6.6 and $1.8 \text{ J kg}^{-1} \text{ K}^{-1}$ for GdNiAl_2 ,

$\text{GdCo}_{0.25}\text{Ni}_{2.5}\text{Al}_{0.25}$ and GdCo_2Al . This is attributed to the decrease in the saturation magnetization value due to the antiferromagnetic behavior in the parent compound GdNiGa_2 . Although all the Ga phases studied have low MCE values compared to the Al analogs, their higher transition temperatures make them potential materials for magnetic refrigeration application.

This work contributes to our understanding of magneto-structural correlations in rare earth transition metal systems, particularly, rare earth transition metal icosagenides. Further studies will be performed to unravel the exact nature of magnetic transitions and magnetically ordered states in many of these compounds, specifically, the multiple transitions in the $\text{GdNi}_{3-x-y}\text{Co}_x\text{Ga}_y$ solid solutions. Such complicated systems require a combination of various methods, including magnetic and heat capacity measurements, X-ray magnetic circular dichroism, and high-temperature X-ray and neutron diffraction measurements. Finally, the plethora of magnetic behavior of $\text{RCr}_x\text{Al}_{2-x}$ phases opens a new avenue in the synthetic exploration of the other early transition metal (V, Ti, Sc) congeners.

APPENDIX A. FIGURES FROM CHAPTER 2

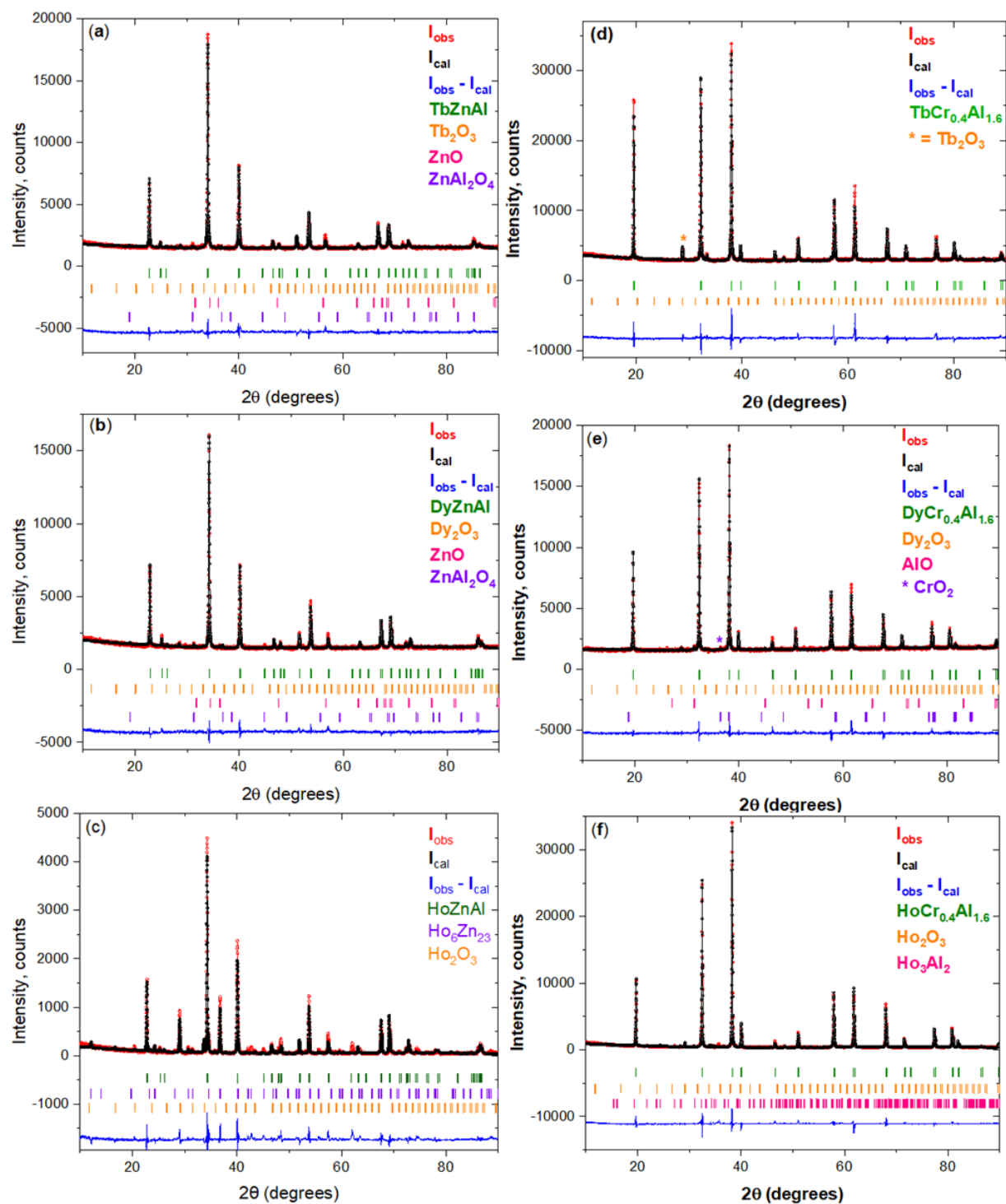


Figure A.1. Rietveld refinement of the powder X-ray diffraction patterns of (a) TbZnAl, (b) DyZnAl, (c) HoZnAl (d) TbCr_{0.4}Al_{1.6}, (e) DyCr_{0.4}Al_{1.6} and (f) HoCr_{0.4}Al_{1.6}.

APPENDIX B. FIGURES FROM CHAPTER 3

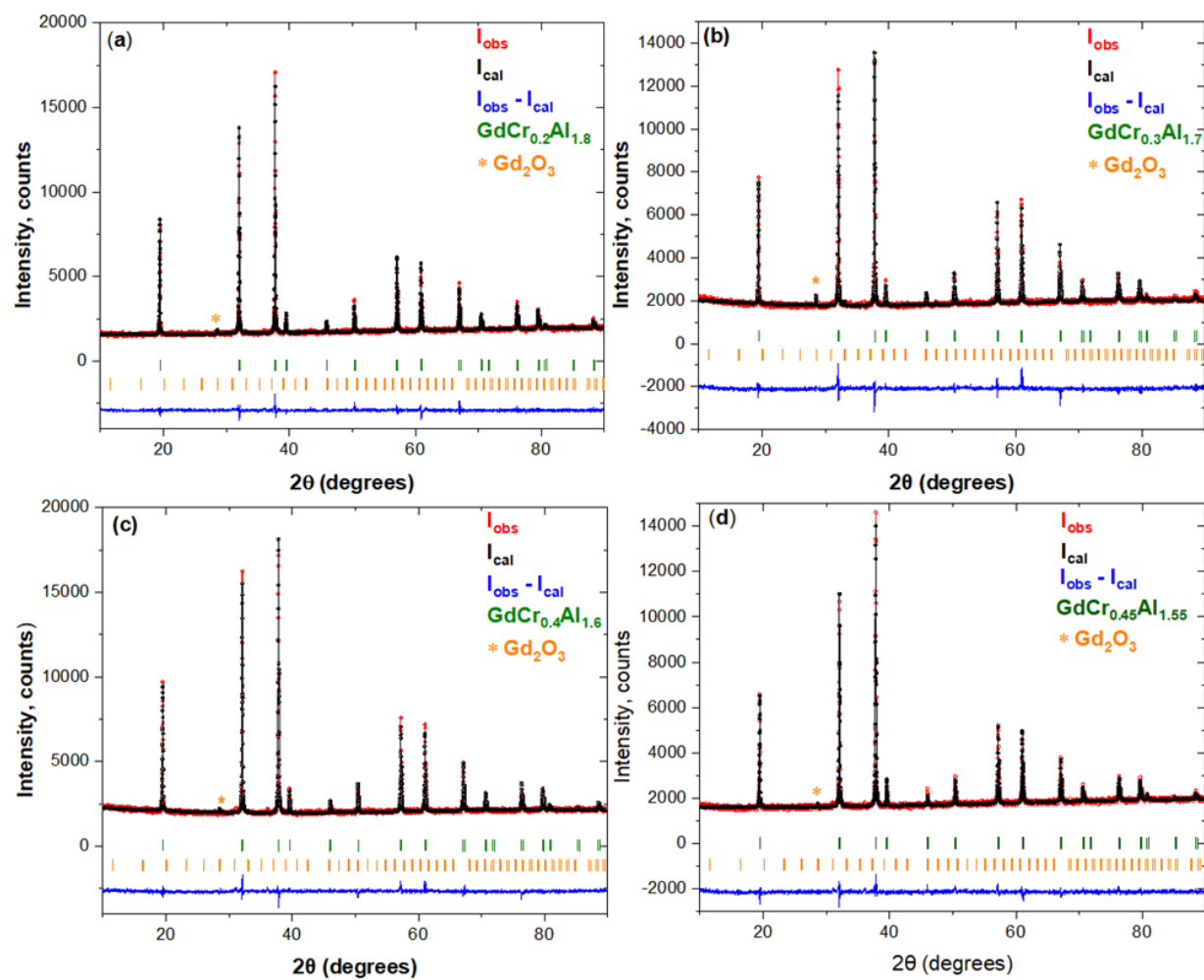


Figure B.1. Rietveld refinement of the powder X-ray diffraction patterns of (a) $\text{GdCr}_{0.2}\text{Al}_{1.8}$, (b) $\text{GdCr}_{0.3}\text{Al}_{1.7}$ and (c) $\text{GdCr}_{0.4}\text{Al}_{1.6}$ and (d) $\text{GdCr}_{0.45}\text{Al}_{1.55}$ compounds

APPENDIX C. FIGURES FROM CHAPTER 4

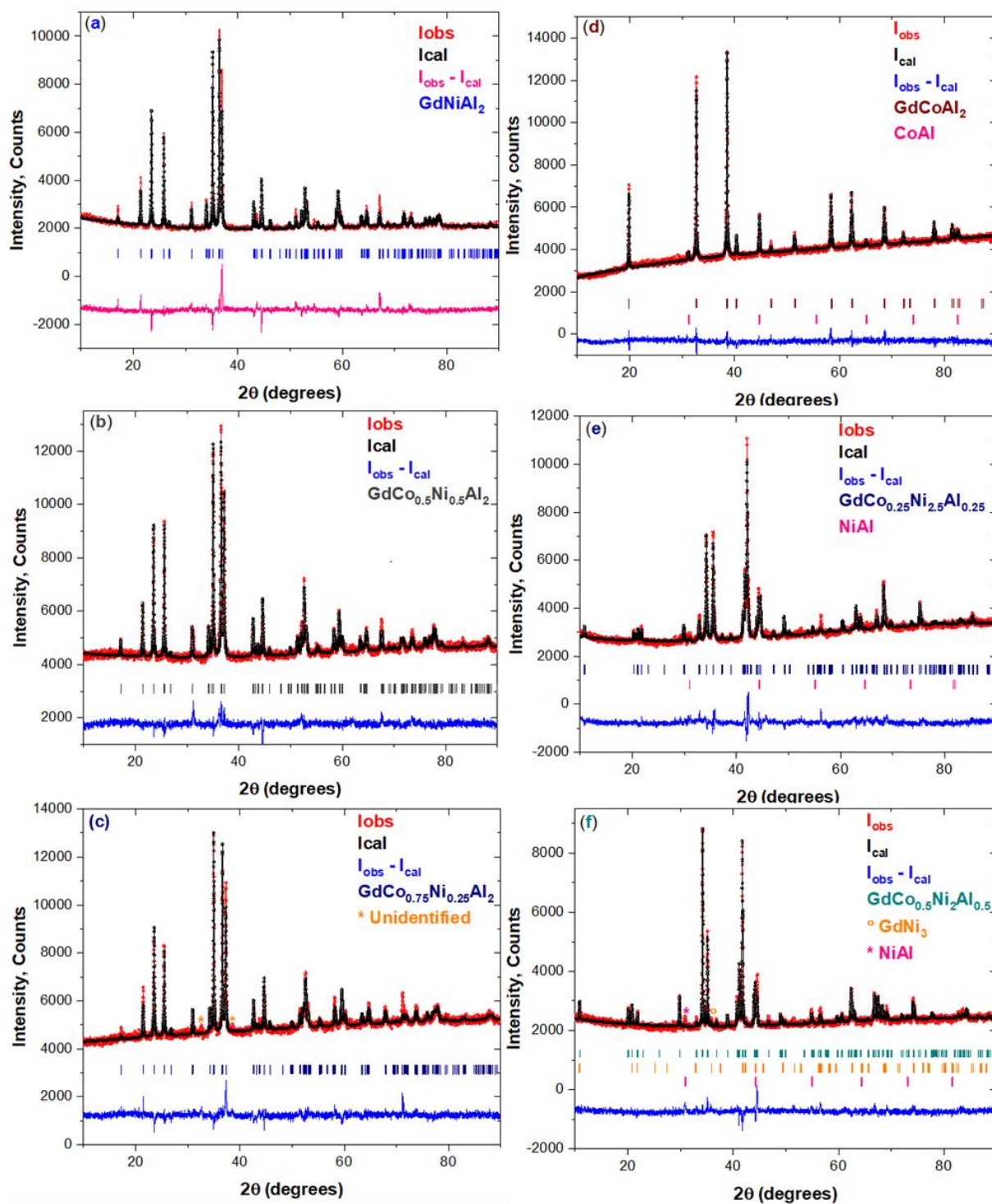


Figure C.1. Rietveld refinement of the powder X-ray diffraction patterns of (a) $GdNiAl_2$, (b) $GdCo_{0.5}Ni_{0.5}Al_2$, (c) $GdCo_{0.75}Ni_{0.25}Al_2$, (d) $GdCoAl_2$, (e) $GdCo_{0.25}Ni_{2.5}Al_{0.25}$, (f) $GdCo_{0.5}Ni_2Al_{0.5}$

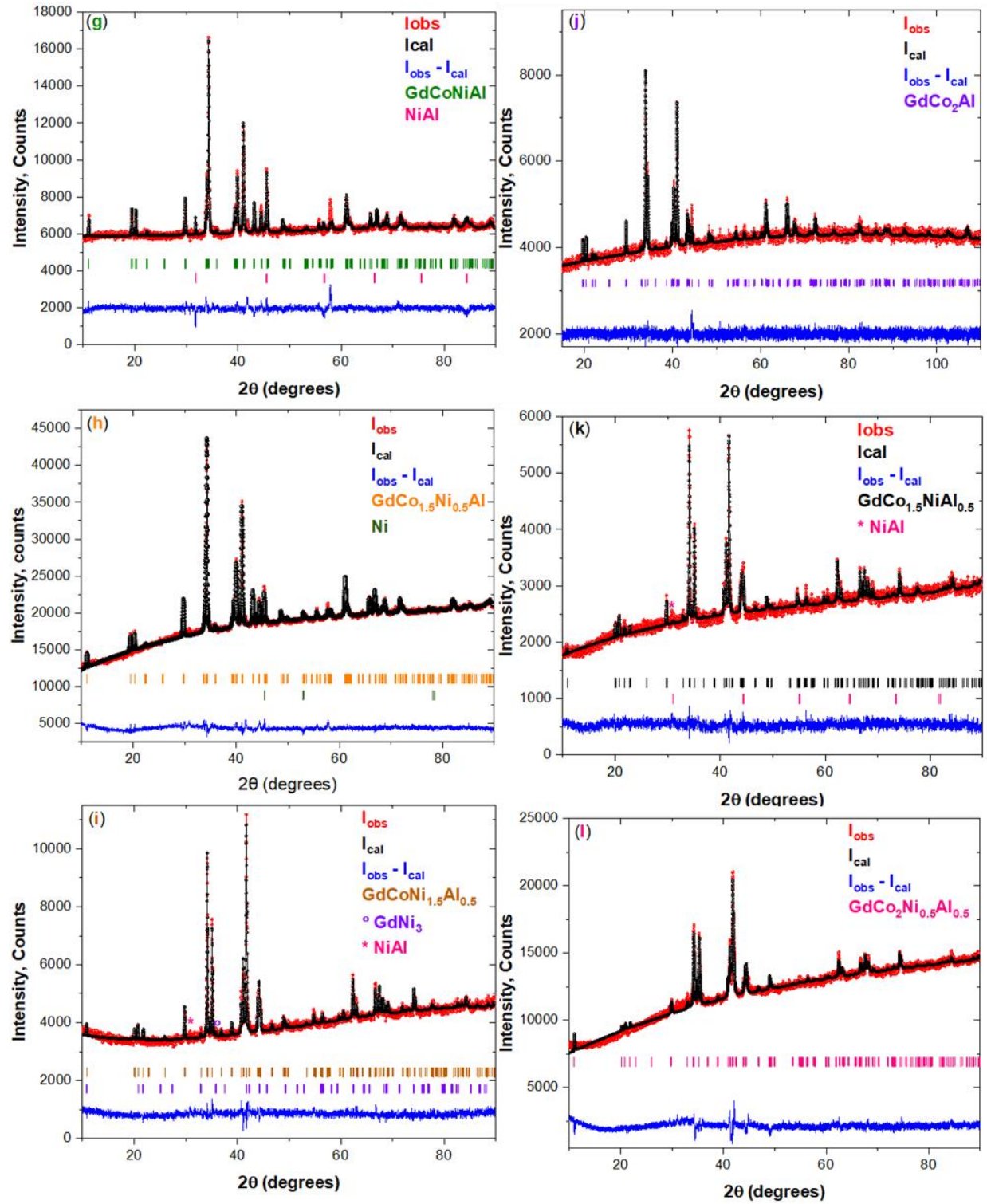


Figure C.2. Rietveld refinement of the powder X-ray diffraction patterns of (g) $GdCoNiAl$, (h) $GdCo_{1.5}Ni_{0.5}Al$, (i) $GdCoNi_{1.5}Al_{0.5}$, (j) $GdCo_2Al$, (k) $GdCo_{1.5}NiAl_{0.5}$ and (l) $GdCo_2Ni_{0.5}Al_{0.5}$.

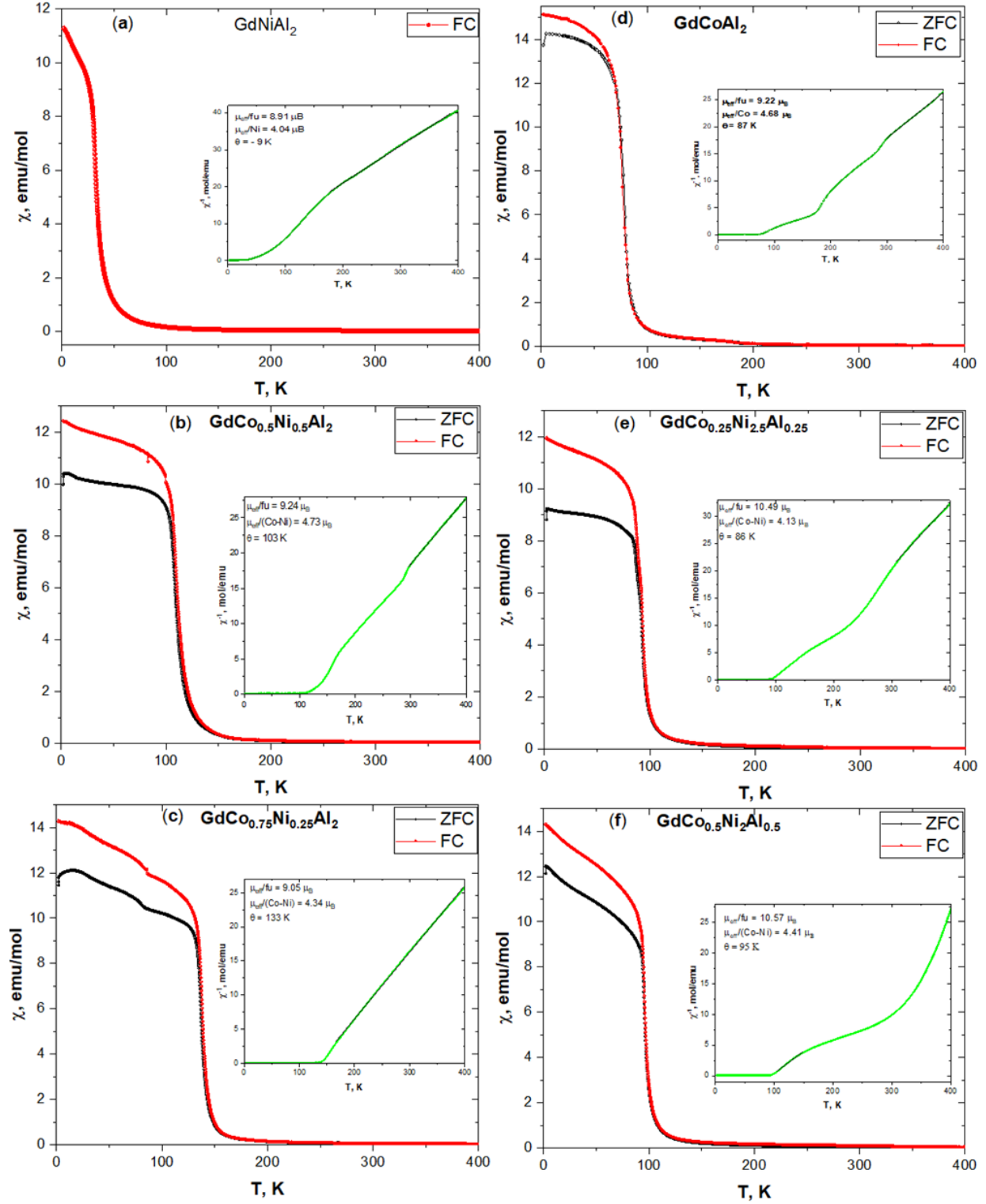


Figure C.3. Temperature dependence of zero-field cooled (ZFC) and field cooled (FC) magnetic susceptibilities of (a) GdNiAl_2 , (b) $\text{GdCo}_{0.5}\text{Ni}_{0.5}\text{Al}_2$, (c) $\text{GdCo}_{0.75}\text{Ni}_{0.25}\text{Al}_2$, (d) GdCoAl_2 , (e) $\text{GdCo}_{0.25}\text{Ni}_{2.5}\text{Al}_{0.25}$ and (f) $\text{GdCo}_{0.5}\text{Ni}_2\text{Al}_{0.5}$ compounds in applied field of 0.01 T.

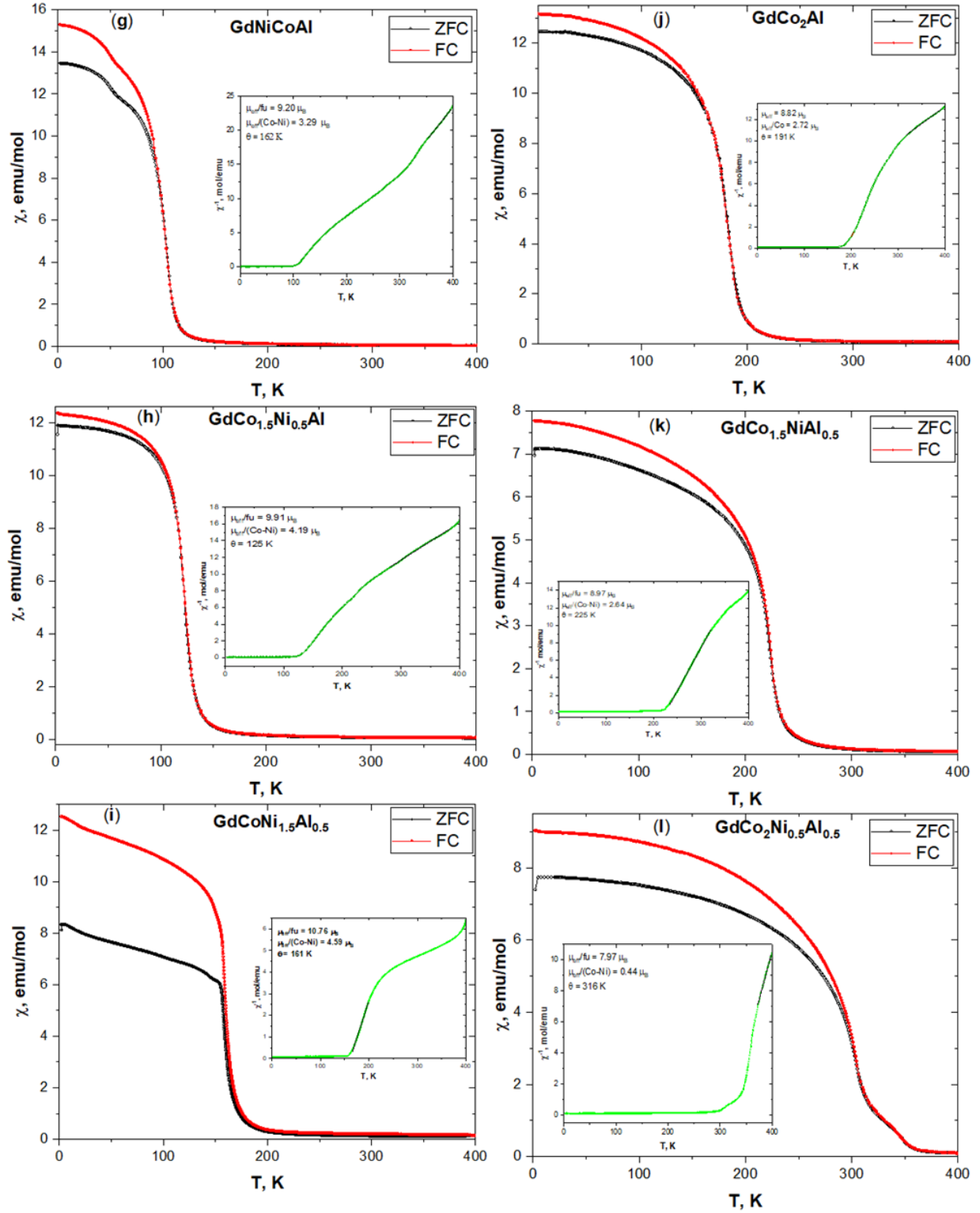


Figure C.4. Temperature dependence of zero-field cooled (ZFC) and field cooled (FC) magnetic susceptibilities of (g) GdCoNiAl, (h) GdCo_{1.5}Ni_{0.5}Al_{0.5}, (i) GdCoNi_{1.5}Al_{0.5}, (j) GdCo₂Al, (k) GdCo_{1.5}NiAl_{0.5} and (l) GdCo₂Ni_{0.5}Al_{0.5} compounds in applied field of 0.01 T.

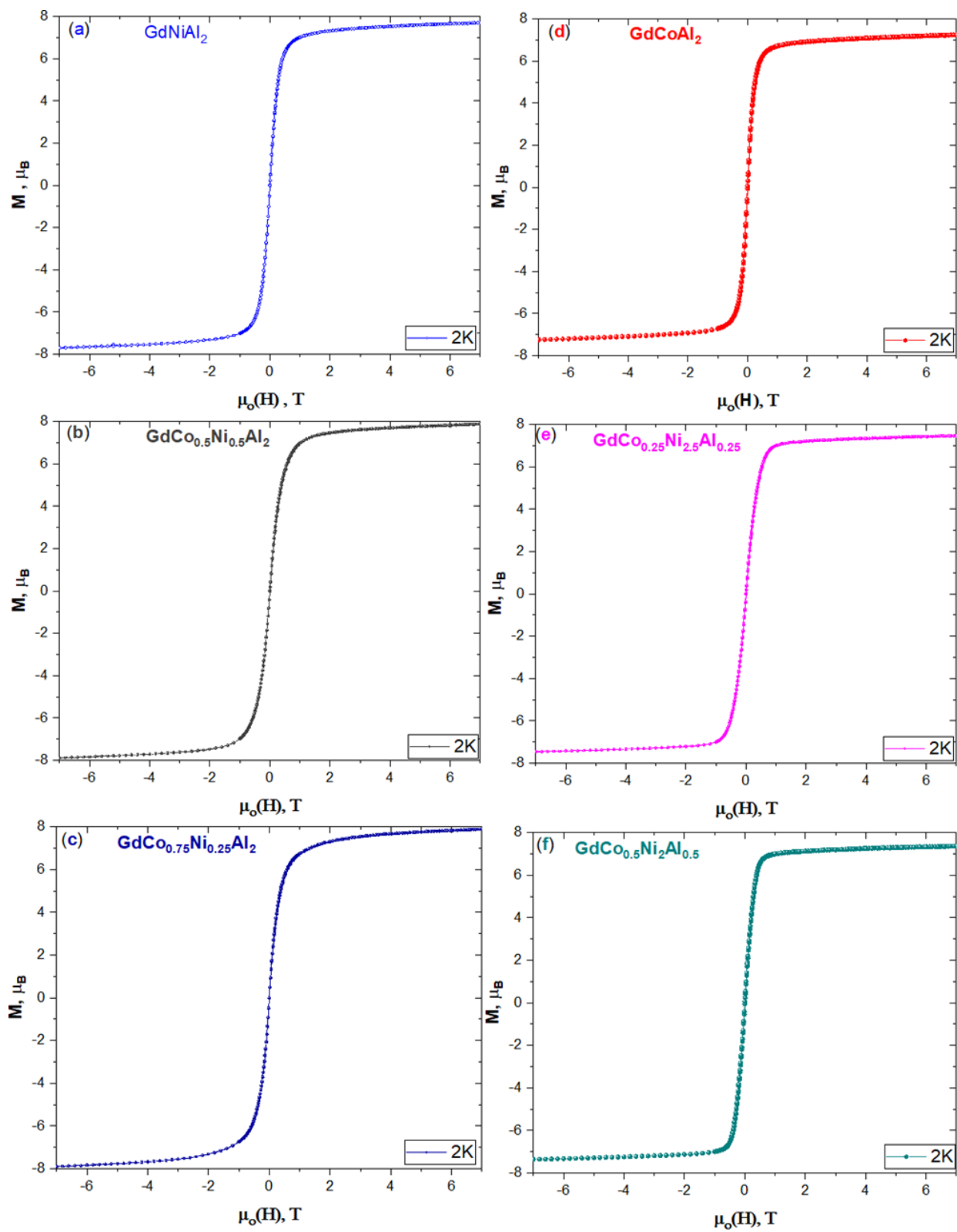


Figure C.5. Field dependence of magnetization for (a) GdNiAl_2 , (b) $\text{GdCo}_{0.5}\text{Ni}_{0.5}\text{Al}_2$ (c) $\text{GdCo}_{0.75}\text{Ni}_{0.25}\text{Al}_2$ (d) GdCoAl_2 , (e) $\text{GdCo}_{0.25}\text{Ni}_{2.5}\text{Al}_{0.25}$ and (f) $\text{GdCo}_{0.5}\text{Ni}_2\text{Al}_{0.5}$ compounds at 2 K in fields up to 7 T.

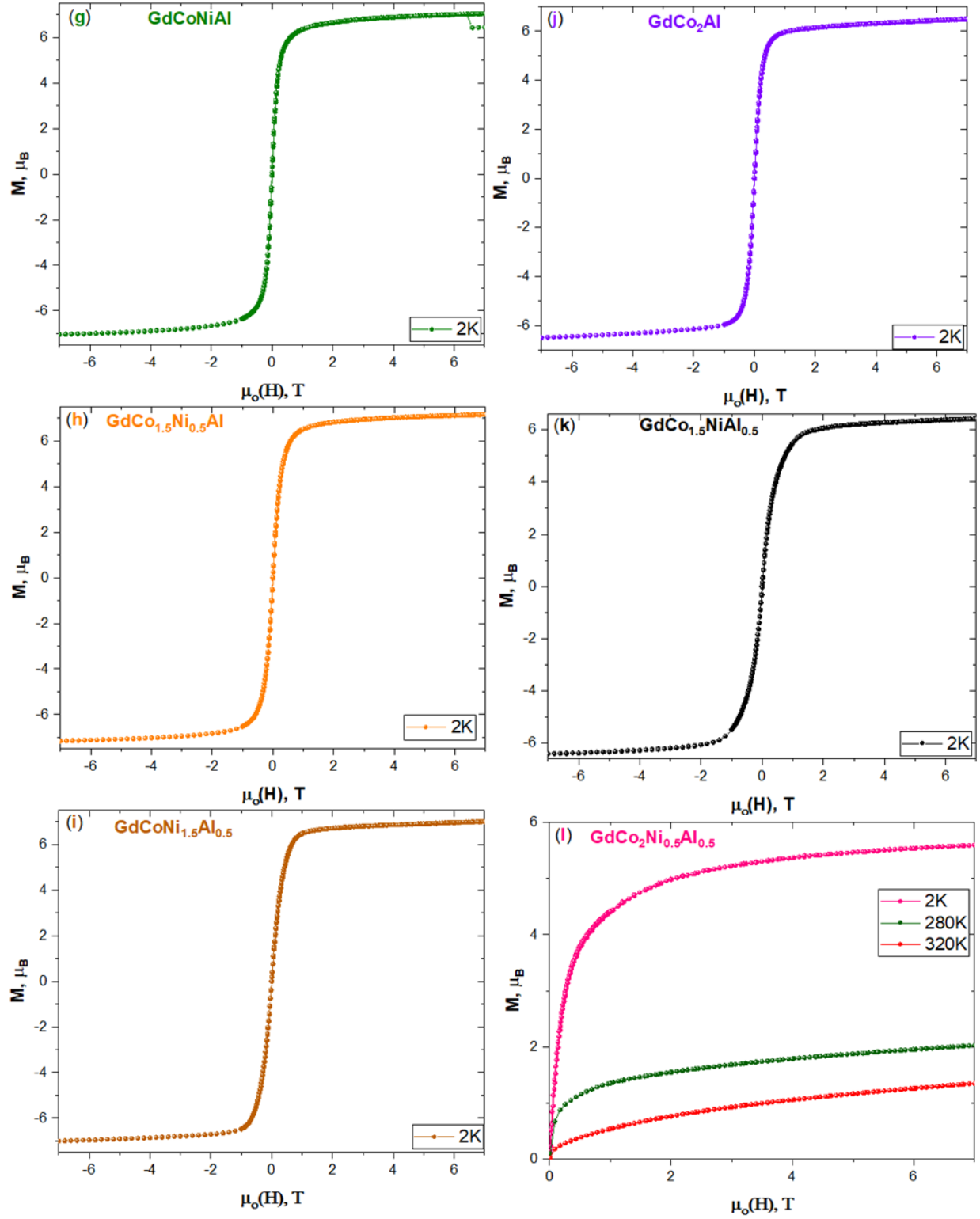


Figure C.6. Field dependence of magnetization for (g) GdCoNiAl, (h) GdCo_{1.5}Ni_{0.5}Al_{0.5}, (i) GdCoNi_{1.5}Al_{0.5}, (j) GdCo₂Al, (k) GdCo_{1.5}NiAl_{0.5} compounds at 2 K and (l) GdCo₂Ni_{0.5}Al_{0.5} at 2, 280, 320 K in fields up to 7 T.

APPENDIX D. FIGURES FROM CHAPTER 5

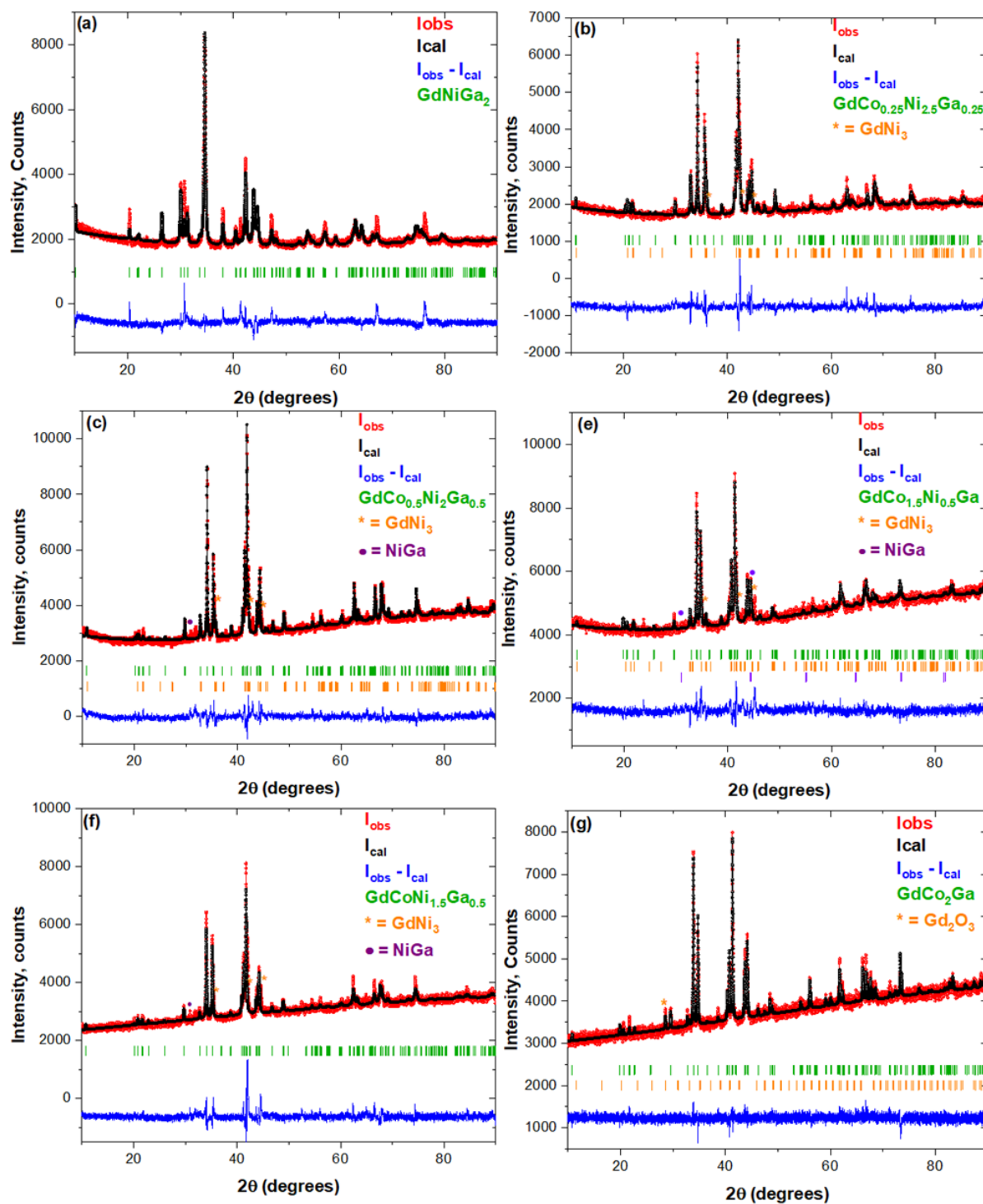


Figure D.1. Rietveld refinement of the powder X-ray diffraction patterns of (a) GdNiGa_2 , (b) $\text{GdCo}_{0.25}\text{Ni}_{2.5}\text{Ga}_{0.25}$, (c) $\text{GdCo}_{0.5}\text{Ni}_2\text{Ga}_{0.5}$, (e) $\text{GdCo}_{1.5}\text{Ni}_{0.5}\text{Ga}$, (f) $\text{GdCoNi}_{1.5}\text{Ga}_{0.5}$ and (g) GdCo_2Ga .

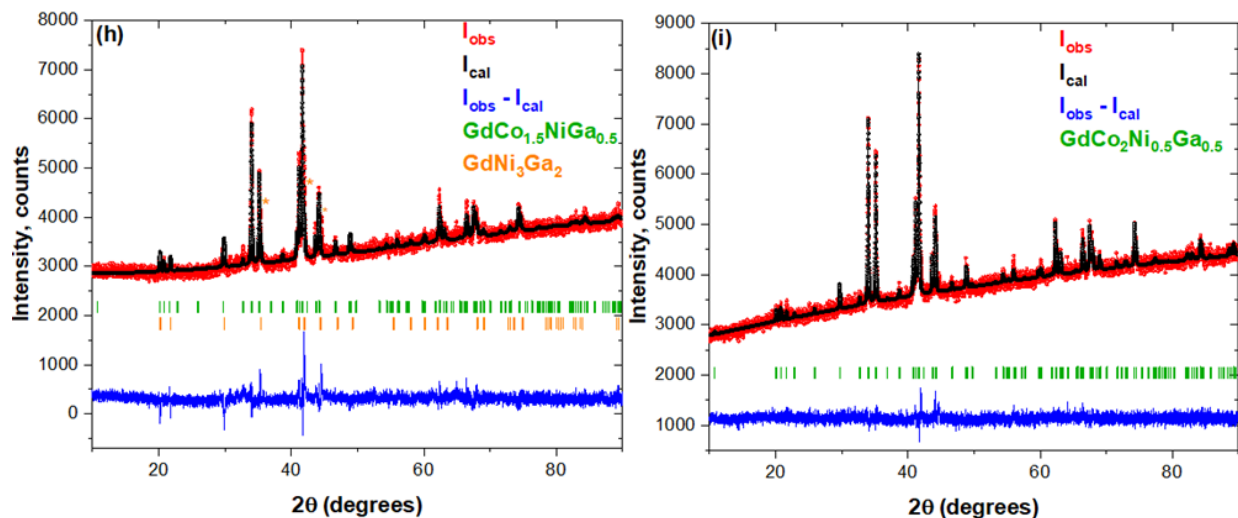


Figure D.2. Rietveld refinement of the powder X-ray diffraction patterns of (h) $\text{GdCo}_{1.5}\text{NiGa}_{0.5}$, (i) $\text{GdCo}_2\text{Ni}_{0.5}\text{Ga}_{0.5}$.

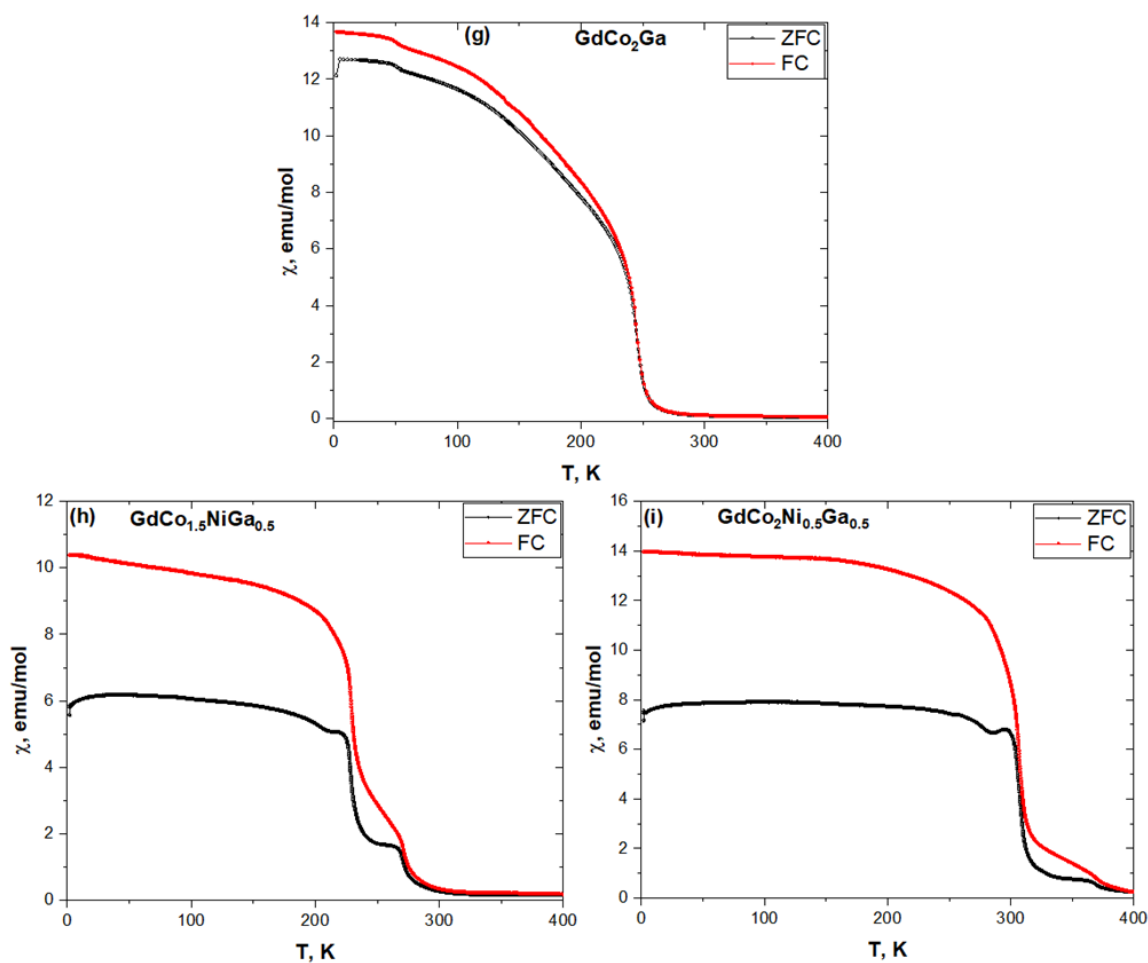


Figure D.3. Temperature dependence of magnetic susceptibility for (g) GdCo_2Ga , (h) $\text{GdCo}_{1.5}\text{NiGa}_{0.5}$, and (i) $\text{GdCo}_2\text{Ni}_{0.5}\text{Ga}_{0.5}$ compounds in applied field of 0.01 T.

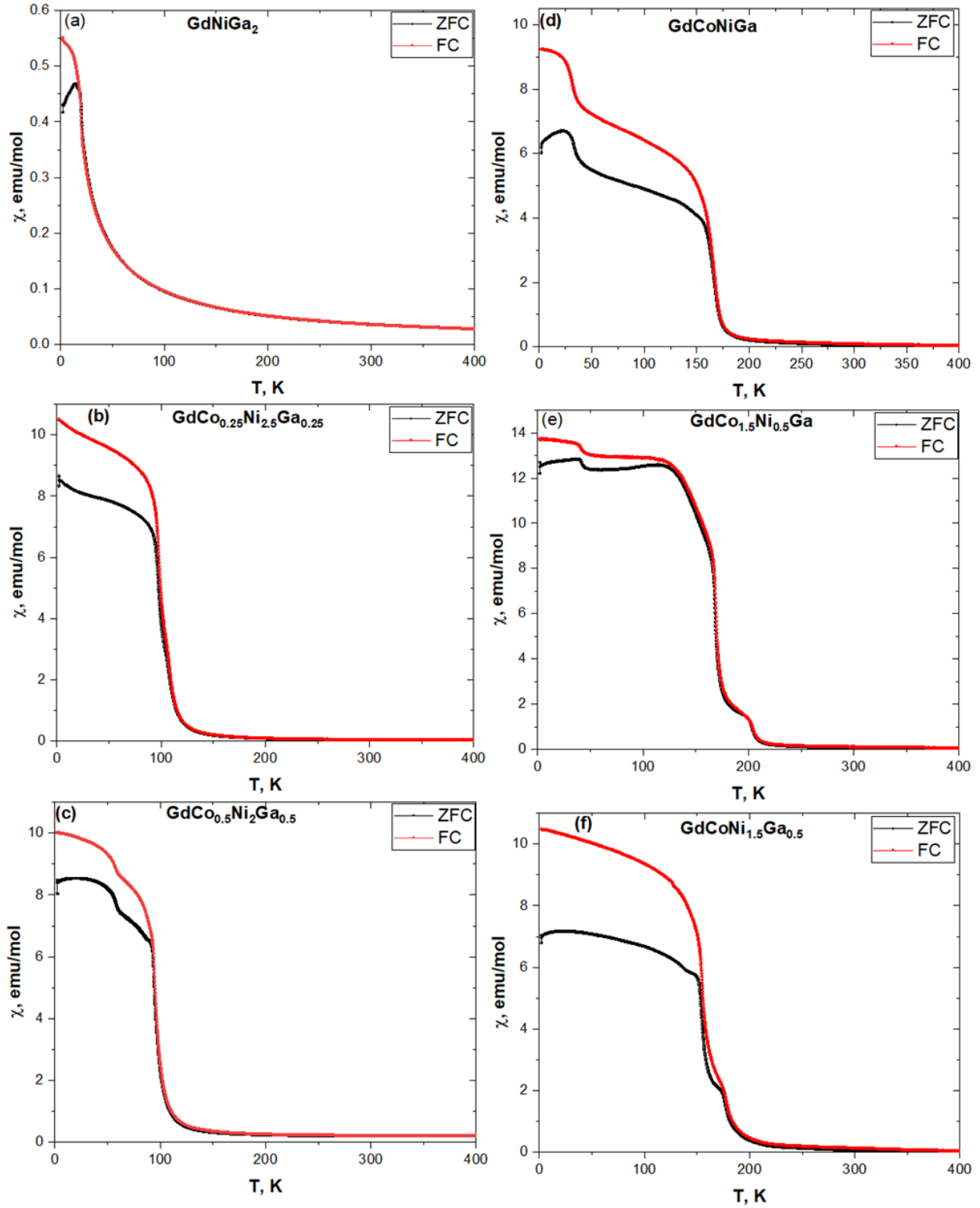


Figure D.4. Temperature dependence of magnetic susceptibility for (a) GdNiGa_2 , (b) $\text{GdCo}_{0.25}\text{Ni}_{2.5}\text{Ga}_{0.25}$, (c) $\text{GdCo}_{0.5}\text{Ni}_2\text{Ga}_{0.5}$, (d) GdCoNiGa , (e) $\text{GdCo}_{1.5}\text{Ni}_{0.5}\text{Ga}$ and (f) $\text{GdCoNi}_{1.5}\text{Ga}_{0.5}$ compounds in applied field of 0.01 T.

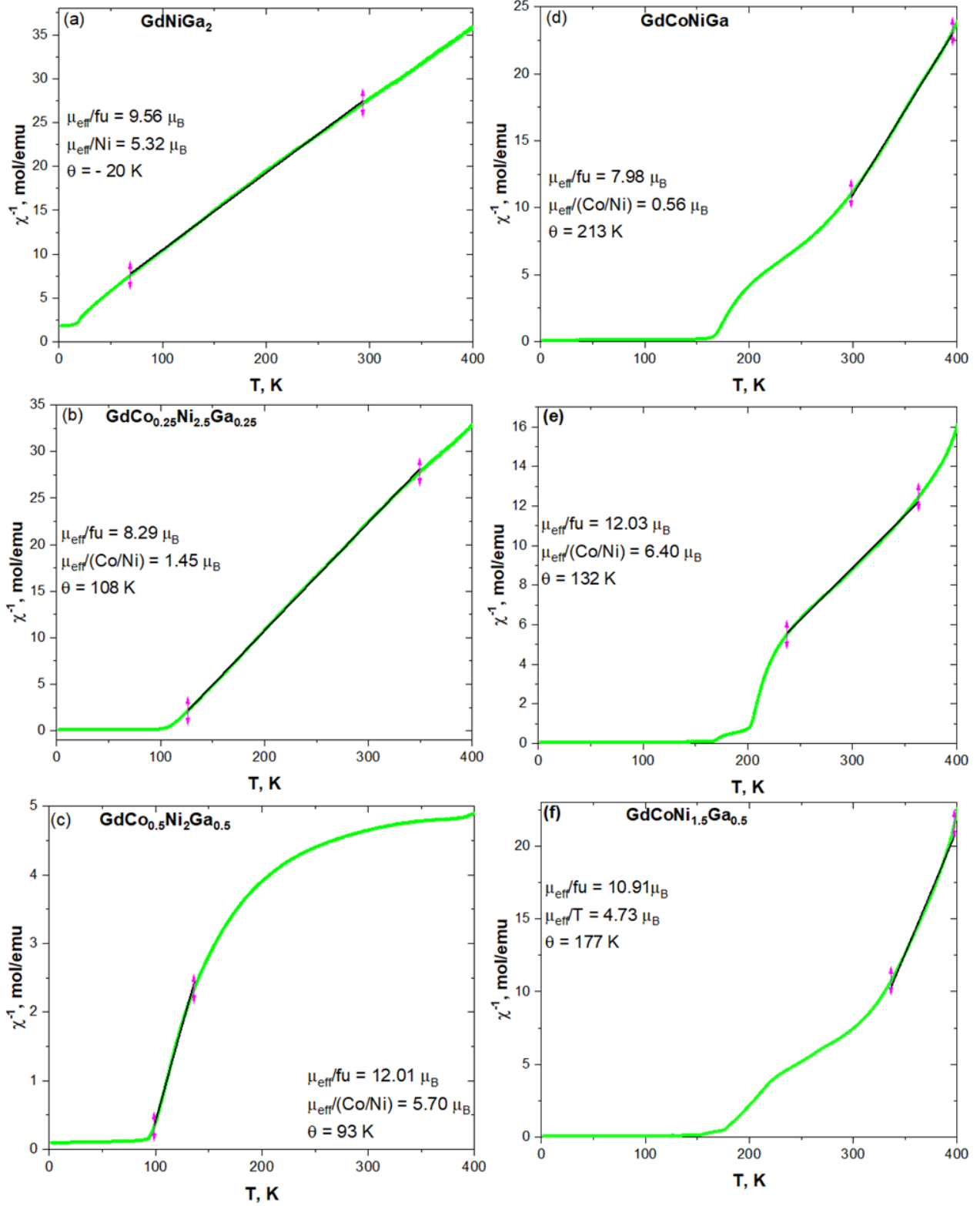


Figure D.5. Linear fit of the inverse susceptibility to the Curie-Weiss law for (a) GdNiGa₂, (b) GdCo_{0.25}Ni_{2.5}Ga_{0.25}, (c) GdCo_{0.5}Ni₂Ga_{0.5}, (d) GdCoNiGa, (e) GdCo_{1.5}Ni_{0.5}Ga and (f) GdCoNi_{1.5}Ga_{0.5} compounds.

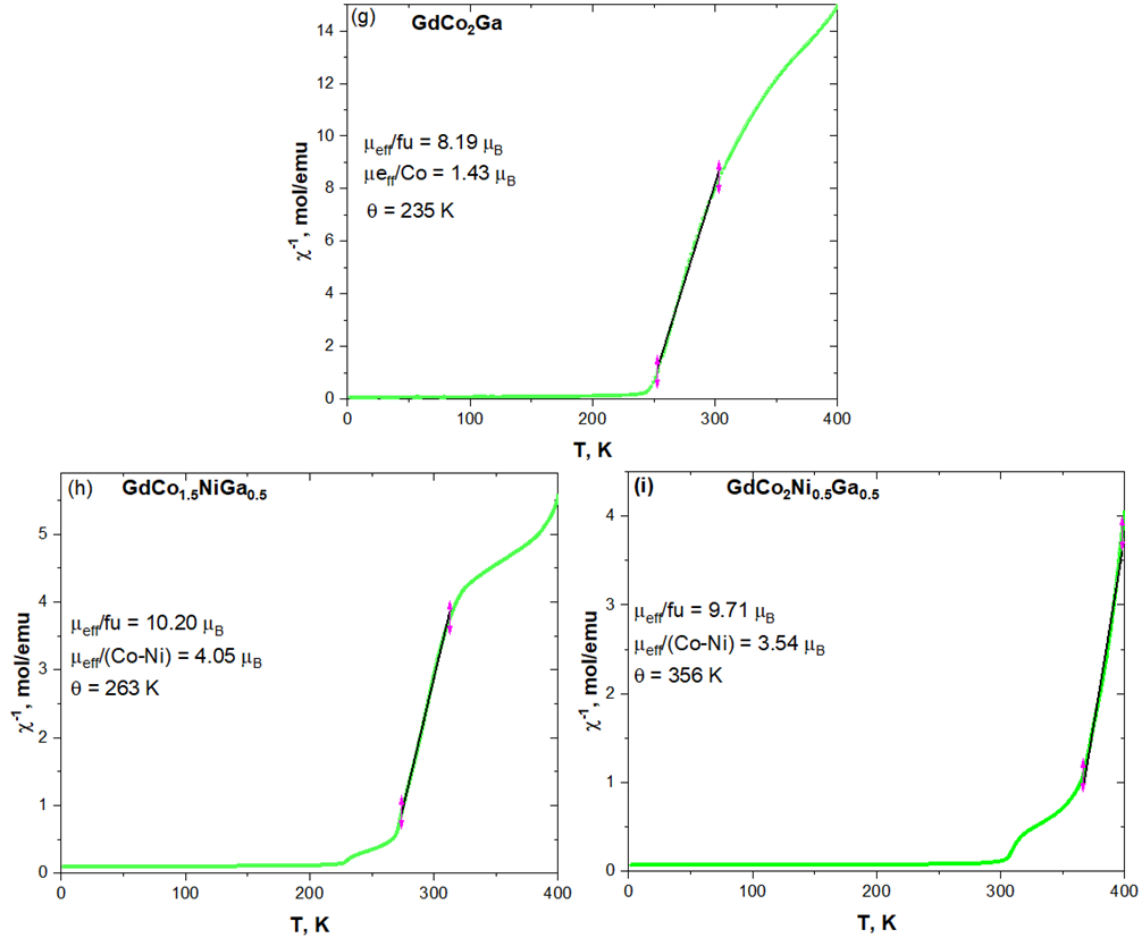


Figure D.6. Linear fit of the inverse susceptibility to the Curie-Weiss law for (g) GdCo_2Ga , (h) $\text{GdCo}_{1.5}\text{NiGa}_{0.5}$, and (i) $\text{GdCo}_2\text{Ni}_{0.5}\text{Ga}_{0.5}$ compounds.

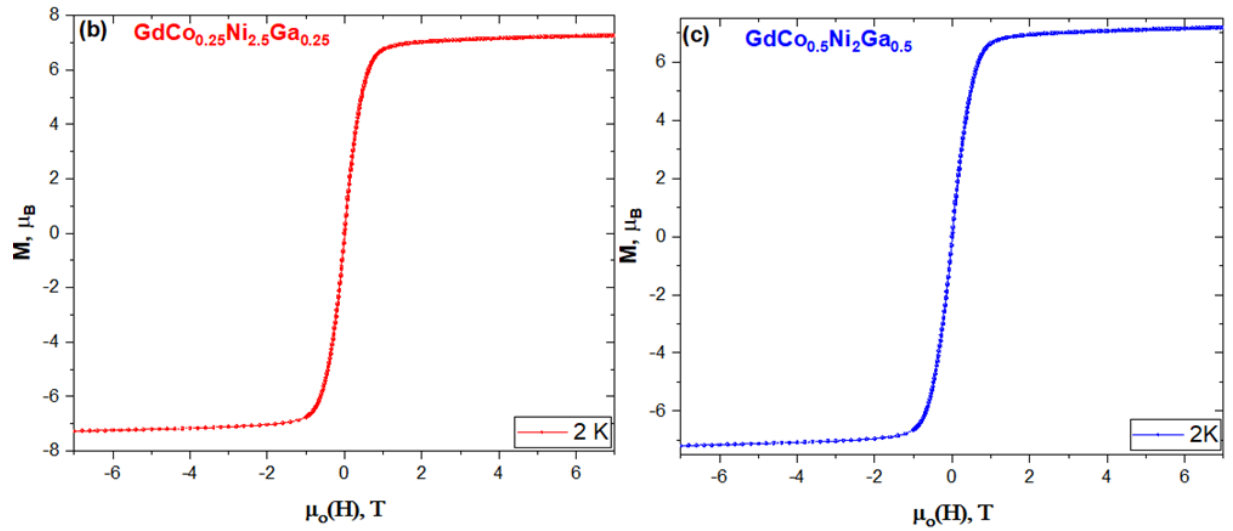


Figure D.7. Field-dependent magnetization of (b) $\text{GdCo}_{0.25}\text{Ni}_{2.5}\text{Ga}_{0.25}$, (c) $\text{GdCo}_{0.5}\text{Ni}_2\text{Ga}_{0.5}$ at 2 K.

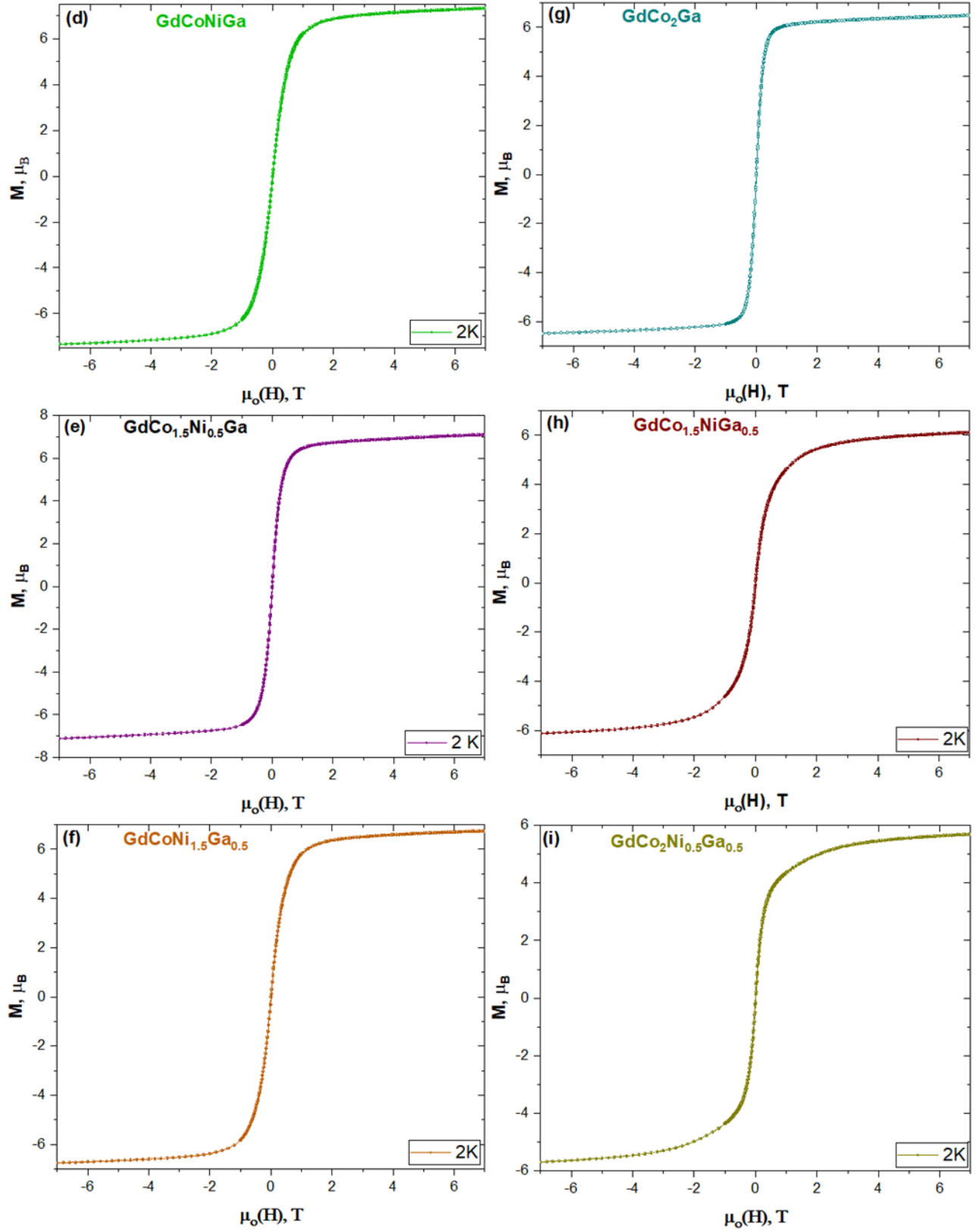


Figure D.8. Field-dependent magnetization of (d) GdCoNiGa , (e) $\text{GdCo}_{1.5}\text{Ni}_{0.5}\text{Ga}$ (f) $\text{GdCoNi}_{1.5}\text{Ga}_{0.5}$, (g) GdCo_2Ga , (h) $\text{GdCo}_{1.5}\text{NiGa}_{0.5}$, and (i) $\text{GdCo}_2\text{Ni}_{0.5}\text{Ga}_{0.5}$ compounds at 2 K.